On-line C-arm intrinsic calibration by means of an accurate method of line detection using the radon transform

Benjamin Spencer

▶ **To cite this version:**

Benjamin Spencer. On-line C-arm intrinsic calibration by means of an accurate method of line detection using the radon transform. Bioengineering. Université Grenoble Alpes, 2015. English. ⟨NNT : 2015GREAS044⟩. ⟨tel-01561081⟩

HAL Id: tel-01561081

https://theses.hal.science/tel-01561081v1

Submitted on 12 Jul 2017

HAL is a multi-disciplinary open access archive for the deposit and dissemination of scientific research documents, whether they are published or not. The documents may come from teaching and research institutions in France or abroad, or from public or private research centers.

L'archive ouverte pluridisciplinaire **HAL**, est destinée au dépôt et à la diffusion de documents scientifiques de niveau recherche, publiés ou non, émanant des établissements d'enseignement et de recherche français ou étrangers, des laboratoires publics ou privés.

HAL Authorization

UNIVERSITÉ DE GRENOBLE

THÈSE

Pour obtenir le grade de

DOCTEUR DE L'UNIVERSITÉ DE GRENOBLE

Spécialité : **ISCE/Biotechnologie, Instrumentation, Signal**

Arrêté ministériel : 7 août 2006

Présentée par

Benjamin Spencer

Thèse dirigée par **Dr. Alexandre Moreau-Gaudry**
et codirigée par **Dr. Laurent Desbat**

préparée au sein du **Laboratoire Techniques de l'Ingénierie Médicale et de la Complexité - Informatique, Mathématiques et Applications de Grenoble**
et de **l'École Doctorale d'Ingénierie pour la Santé, la Cognition et l'Environnement**

On-line C-arm Intrinsic Calibration by means of an Accurate Method of Line Detection using the Radon Transform

Thèse soutenue publiquement le **18 Décembre 2015**,
devant le jury composé de :

Dr. Philippe Cinquin
PU-PH, TIMC-IMAG, UJF-CNRS, Grenoble, Président
Dr. Jean-Michel Létang
Maître de Conférences, Institut National des Sciences Appliques, CREATIS, UCB Lyon, Rapporteur
Dr. Dimitris Visvikis
Directeur de Recherche Institut national de la santé et de la recherche médicale, LATIM, UBO Brest, Rapporteur
Dr. Catherine Burnier
Enseignante-chercheuse, CPE, Lyon, Examinatrice
Dr. Alexandre Moreau-Gaudry
PU-PH, TIMC-IMAG, UJF Grenoble, Directeur de thèse
Dr. Laurent Desbat
Professeur, TIMC-IMAG, UJF Grenoble, Co-Directeur de thèse

Dr. Julien Bert
Ingénieur de recherche, LATIM, Brest, Invité

Contents

1 Introduction **1**

1.1 Calibration of Isocentric C-arm Systems for 3D Image Reconstruction 3

1.2 Materials, Methods and Context for the Following Research 10

1.2.1 Isocentric C-arm x-ray imaging system 10

1.2.2 Review of projective geometry 14

1.2.3 Simulation program 21

1.3 Summary 25

2 General Approach to Intrinsic Calibration **29**

2.1 Homography Intrinsic Calibration Method 30

2.1.1 Homography determined using lines 32

2.1.2 Initial estimate of $\mathbf{K_0}$ 33

2.1.3 Detection of spherical markers in an x-ray image 33

2.2 Results 34

2.2.1 Initial validation of homography calibration - noiseless simulated projection images as source and detector rotate along perfect circular trajectory 35

2.2.2 Evaluation with noise but without C-arm deformation 36

2.2.3 Evaluation with noise and C-arm deformation 37

2.2.4 Single and multiple deformation parameter variation 38

2.3 Discussion 39

3 Collimator Edge Detection via the Radon Transform for Homography Intrinsic Calibration **43**

3.1 Introduction to Line or Edge Detection 44

3.1.1 Line determination using the Radon transform 46

3.2 Implementation of method of line detection 55

3.2.1 Principle of measurements of (θ, s) 56

3.2.2 General method of edge detection 57

3.2.3 Approach to edge detection by various methods 61

3.3 Optimal Method of Edge Detection 72

3.3.1 Sensitivity of $(\widetilde{\varphi}, \widetilde{s})$ measurement 73

3.3.2 Various methods of edge detection 76

3.3.3 Discussion on optimal edge detection methods 94

3.4 Further Evaluations of Edge Detection 98

3.4.1 Effects from noise and simulated C-arm deformation 98
3.4.2 Single and multiple deformation parameter variation 101
3.4.3 Comparison of intrinsic calibration from edges, spherical markers, and the gold-standard calibration method 104
3.4.4 Discussion on further evaluations of edge detection 106
3.5 Edge Detection Applied to C-arm Projections of the X-ray Tube Collimator 108
3.5.1 Edge detection with real data 109
3.5.2 Results of edge detection on real data 110
3.5.3 Discussion regarding edge detection in real C-arm images 117

4 Application to 3D Image Reconstruction **119**
4.1 Introduction to Cone-Beam Image Reconstruction Methods 120
4.2 Conditions and Implementation of Reconstruction 126
4.3 Results of Image Reconstruction 130
4.4 Discussion 135

5 Conclusions and Future work **139**
5.1 Discussion and Future work 143

Bibliography **149**

List of Figures

1.1 Isocentric C-arm x-ray system. 11
1.2 Projection images of the x-ray tube collimator in the field of view 12
1.3 A picture, and x-ray projection of the gold-standard calibration phantom . . . 15
1.4 Pin-hole and direct imaging camera models. 17
1.5 A diagram of the homography model 19
1.6 A comparison of a simulated projection image with added noise with a real projection image 23
1.7 Comparison of a simulated image with noise and a real projection image of the x-ray tube collimator 25
1.8 Comparison of a simulated image with noise and a real projection image of the gold-standard calibration phantom 26

2.1 Diagram of the homography intrinsic calibration model. 31

3.1 Characterization of a line in an image 46
3.2 Diagram of the x-ray projection of the collimator edge (2D). 47
3.3 The collimator edge profile from a real x-ray C-arm image 48
3.4 Collimator edge profiles in simulated image 49
3.5 Example of the Radon transform of an image 50
3.6 Example of the Radon transform of an edge 51
3.7 Profile of the 1D Radon transform of a simulated edge 51
3.8 Radon transform of the x-ray collimator edge 52
3.9 First and second derivative of a simulated edge profile 53
3.10 Diagram of the sensitivity of line angle measurement 54
3.11 An example of a simulation generated image of the collimator 56
3.12 Diagram showing the ImageJ and Radon coordinate systems. 57
3.13 Depiction of image centering process 58
3.14 Flow chart of edge angle and position determination process. 60
3.15 Example of the peak of curves 61
3.16 Example of the derivative of the 1D Radon Transform 63
3.17 Example bias in edge angle estimation 64
3.18 First derivative of the Radon transform with and without noise 64
3.19 First derivative of the Radon transform with and without Gaussian filtering . 65
3.20 Second derivative of the 1D RT (with $\theta = \varphi$) 69
3.21 Second derivative of the cubic spline fit to the 1D RT with noise 70

3.22 Curve of the maximum of the derivative of the 1D RT versus the Radon transform angle . . . 80
3.23 Curve of the maximum of the derivative of the 1D RT versus the Radon transform angle with Gaussian filtering . . . 80
3.24 Curve of the slope of the line fit to the 1D RT versus the Radon transform angle 85
3.25 Example of a simulated image before and after the application of the Canny edge detector . . . 91
3.26 Example of edge detection after application of the Canny edge detector and Radon transform . . . 93
3.27 Projection images from two C-arm scans of the x-ray tube collimator for edge detection . . . 110
3.28 Estimated positions and angles of right and top edges by the three edge detection methods . . . 111
3.29 Linear fit method estimated positions of the edges in two C-arm scans . . . 114
3.30 Linear fit method estimated angles of the edges in two C-arm scans . . . 115
3.31 Projection images showing edge detection error due to object in the field of view 116

4.1 An illustration of parallel beam imaging . . . 122
4.2 Depiction of the frequency domain sampling from multiple parallel beam measurements . . . 124
4.3 A description of the fan-beam projection of a 2D object onto a 1D detector. . . 125
4.4 An illustration of a cone-beam projection of a 3D object . . . 126
4.5 Image reconstruction comparison of four different calibrations . . . 132
4.6 Image reconstructions showing the max and min estimated calibration error . 134
4.7 Diagram illustrating the consequence of a static detector position error in the plane of orbital rotation on 3D image reconstruction . . . 136

List of Tables

1.1 Simulated phantom specifications 24
1.2 The maximum and standard deviation of the varied C-arm deformation parameters for simulation experiments. 25

2.1 Chart of simulation evaluation comparisons. 34
2.2 Comparison of intrinsic calibration methods with the ground-truth without noise or C-arm deformation 36
2.3 Comparison of intrinsic calibration methods with the ground-truth with noise but without C-arm deformation 37
2.4 Comparison of intrinsic calibration methods with the ground-truth with noise and C-arm deformation 38
2.5 The intrinsic calibration estimation error from single parameter deformation . 39
2.6 The intrinsic calibration estimation error from multiple parameter deformation 39

3.1 Collimator edge segmentation in Radon transform space 58
3.2 Homography calibration sensitivity due a to static edge angle deviation 76
3.3 Homography calibration sensitivity due to a static edge position deviation . . 77
3.4 Homography calibration sensitivity due to uniform random deviations in the edge angles and positions 77
3.5 Edge angle and position error using max derivative of the 1D RT 81
3.6 Intrinsic calibration error using max derivative of the 1D RT 81
3.7 Edge angle and position error using derivative and mean filter 83
3.8 Intrinsic calibration error using derivative and mean filter 83
3.9 Edge angle and position error using linear fit to 1D RT 84
3.10 Intrinsic calibration error using linear fit to 1D RT 84
3.11 Edge angle and position error using average first derivative of polynomial . . . 86
3.12 Intrinsic calibration error using average first derivative of polynomial 87
3.13 Edge angle and position error using the R^2 correlation coefficient of the polynomial 87
3.14 Intrinsic calibration error using R^2 correlation coefficient of the polynomial . . 87
3.15 Edge angle and position error using second derivative of the 1D RT 88
3.16 Intrinsic calibration error using second derivative of the 1D RT 89
3.17 Edge angle and position error using first derivative of the cubic spline 89
3.18 Intrinsic calibration error using first derivative of the cubic spline 89
3.19 Edge angle and position error using the Canny edge detector and Hough transform 90

3.20 Intrinsic calibration error using the Canny edge detector and Hough transform 90
3.21 Edge angle and position error using the Canny edge detector and Radon transform 92
3.22 Intrinsic calibration error using the Canny edge detector and Radon transform 92
3.23 Edge angle and position error using the derivative of a Gaussian filter 93
3.24 Intrinsic calibration error using the derivative of a Gaussian filter 94
3.25 Noise and deformation affects on edge detection and IC accuracy using the linear fit method 99
3.26 Noise and deformation affects on edge detection and IC accuracy using the derivative of a Gaussian filter method 100
3.27 Noise and deformation affects on edge detection and IC accuracy using the Canny edge detector and Radon transform 101
3.28 The IC and edge estimation error by the linear fit method from single and multiple parameter deformation 103
3.29 The IC and edge estimation error by the derivative of a Gaussian filter method from single and multiple parameter deformation 104
3.30 The IC and edge estimation error by the Canny edge detector method from single and multiple parameter deformation 105
3.31 Comparison of IC accuracy using edges (LF method), spherical markers, and the gold-standard with noise and C-arm deformation 106
3.32 Angle and position estimations of the edges of the x-ray tube collimator imaged in a typical C-arm scan 112

4.1 The maximum and standard deviation of the varied C-arm deformation parameters for simulation experiments. 127
4.2 Average from all 29 scans of the reconstructed marker RMS position error between the ground-truth and the estimated calibrations 131
4.3 Average from all 29 scans of the reconstructed marker radii ratio from the four calibrations 133

List of Abbreviations

CED Canny edge detector. vi–viii, 58, 66–68, 84–89, 91, 92, 96, 97, 99, 101, 103, 137

CFRT Canny filter followed by the Radon transform. 92–94, 97–100, 102–105, 107, 108, 113, 114

CT computed tomography. 1, 2, 8

DGF derivative of a Gaussian filter. 67, 68, 85–88, 92–94, 96, 98–100, 102–105, 107, 108, 113

DMF derivative of a mean filter. 78, 81, 90–93

FBP filtered back-projection. 116, 118, 120

FDK Feldkamp Davis & Kress cone-beam reconstruction. 8, 116, 121, 123

FOV field of view. 3, 5, 6, 11, 24, 25, 27, 38, 52, 70, 92, 94, 100, 103–107, 109, 110, 113, 114, 135, 137–143

GF Gaussian filter. 62, 64, 77–84, 90–93, 103

GT ground-truth. 69, 70, 73–75, 77, 86, 88, 95, 97, 100, 105

HC homography calibration. 30–38, 69, 71, 74, 86, 94, 100–102, 104

HT Hough transform. 67

IC intrinsic calibration. 4–6, 23–25, 27–38, 135–142

IR image reconstruction. 115, 116, 118, 121, 124–126, 128, 129, 132, 133, 138, 139

LF linear fit. 78, 81, 90–95, 98–105, 107–109, 113, 123

MF mean filter. 61, 64, 66, 78, 84, 91

RMS root-mean square. 33–35, 74, 77, 86, 93, 97, 104, 126, 128, 129

RT Radon transform. 46, 48, 49, 54, 56–58, 60–70, 74–76, 78–84, 88, 90–93, 139, 140

RTK Reconstruction toolkit. 6, 115, 116, 123

SD standard deviation. 22, 32–35, 56, 63, 68, 75, 77–94, 103, 105, 106, 108, 109, 122

Chapter 1

Introduction

Résumé de l'Introduction en Français

Les systèmes d'imagerie radiologique ≪ C-arm ≫ fournissent des images 3D pour la planification, le contrôle et le guidage dans de nombreuses interventions chirurgicales. Les scanners C-arm collectent de nombreuses projections radiographiques 2D en géométrie conique lors de leur rotation de plus de 180 degrés autour du patient. Ces projections 2D peuvent être traitées pour produire une volume 3D reconstruit grâce à un algorithmes de reconstruction 3D. Ces algorithmes nécessitent la connaissance de la géométrie conique d'acquisition de chaque radiographie, c'est à dire la position de la source ainsi que la position et l'orientation du détecteur. Au cours de la trajectoire d'acquisition le C-arm, peut se déformer mécaniquement, des vibrations peuvent perturber les différentes positions et orientations, en particulier pour les c-arm standard. Ceci implique la nécessité de calibrer les paramètres qui définissent la géométrie d'acquisition. Le modèle utilisé est semblable à celui des caméra pinhole et donc les procédés de calibration du domaine de la vision par ordinateur peuvent être adaptés. Classiquement, les paramètres de calibrations sont séparés en paramètres intrinsèques (ceux qui décrivent le système de mesure indépendamment de l'objet mesuré) et paramètres extrinsèques (ceux qui décrivent la position et l'orientation du système de mesure relativement à l'objet mesuré).

Il existe de nombreuses techniques pour la calibration de C-arm. De nombreuses font l'hypothèse que la déformation du C-arm motorisé au cours de l'acquisition est reproductible. Il suffit donc de calibrer offline le C-arm en fonction des paramètres de position, c'est a dire des paramètres de commande du moteur. Certaines mécaniques de C-arm ne permettent pas de faire une telle hypothèse.

L'objet de notre recherche est de proposer une méthode de calibration intrinsèque ≪ on-line ≫ de C-arm en n'utilisant que les informations radiologiques induites par la présence d'un collimateur attaché à la source. Cela implique une méthode extrêmement précise de détection des bords linéaires épais du collimateur dans les projection radiologiques. Puisque le collimateur est attaché à la source, seules des informations sur les

paramètres de calibration intrinsèque pourront être déterminées.

Aucune information sur la position ou l'orientation du collimateur n'est nécessaire pour notre procédure de calibration intrinsèque. Nous faisons simplement l'hypothèse que le collimateur est fixé sur la source. Cependant seulement des variations des paramètres intrinsèques entre projections successives peuvent être identifier. C'est pourquoi, une calibration complète des paramètres intrinsèques doit être fournie pour une acquisition de référence. Une méthode de calibration des paramètres extrinsèques doit aussi être disponible ou bien notre méthode de calibration intrinsèque doit être couplée à une autre méthode pour le calibrage complet du système.

Des recherches analogues ont été proposées dans la littérature avec des marqueurs (billes radio opaques) à la place des bords du collimateur. Le travail de Gorges et al. [Gorges 2007, Gorges *et al.* 2006] propose une mire de calibration attachée au détecteur. L'idée de marqueurs attachés à la source a été proposée (et brevetée) par Navab et al [Navab & Mitschke 2001] et utilisée par Mit [Mitschke & Navab 2003].

Enfin l'idée d'utiliser le collimateur de la source pour la calibration d'un C-arm a été breveté par Schuetz [Schuetz 2001]. Dans [Schuetz 2001] la position des bords du collimateur est supposée connue relativement à la source et d'autre part le collimateur est supposé essentiellement planaire. Dans notre travail, ces conditions ne sont pas requises. De plus le brevet [Schuetz 2001] ne propose *aucune* méthode robuste et précise de détection de la projection des bords du collimateur dans les projections radiographiques.

Une importante contribution de notre travail est dédiée à la détermination précise et robuste de l'angle et la position d'un bord dans une image radiographique. La détection de bords ou de droites a été analysée en profondeur dans le domaine de la vision par ordinateur mais il n'existe pas de travail qui étudie le niveau de précision dans cette détection afin de déterminer les paramètres de calibration intrinsèque.

Dans le chapitre 2 nous introduisons les techniques de calibrations intrinsèques envisagées. Des résultats préliminaires de simulations de techniques de calibration à partir de marqueurs son présentées. La précision de la calibration intrinsèque d'une projection radiographique est discutée.

Le chapitre 3 est consacré à l'étude de la détermination de la projection des bords du collimateur dans une radiographie. Plusieurs méthodes de détection de bord (certaines sont originales) sont étudiées et comparées sur des données simulées mais aussi sur des données réelles.

Le chapitre 4 permet de valider les méthodes de calibration développées dans notre travail dans le cadre de la reconstruction 3D à partir de multiples radiographies. Elle

sont comparées une méthode standard de calibration globale à base d'une mire 3D de marqueurs.

Le chapitre 5 rassemble les résultats obtenus, et discute les limitations de nos méthodes ainsi que les améliorations possibles à mettre en place dans de travaux futurs.

1.1 Calibration of Isocentric C-arm Systems for 3D Image Reconstruction

Three-dimensional (3D) interventional computed tomography (CT) imaging and guidance is required during numerous medical procedures, such as: minimally invasive spine surgery [Siewerdsen *et al.* 2005], orthopedics [Khoury *et al.* 2007], head and neck surgery [Chan *et al.* 2008], brachytherapy seed placement [Jaffray *et al.* 2002a], and application to treatment planning before and during radiation therapy [Jaffray *et al.* 2002b]. Furthermore, many interventional procedures require 3D imaging in addition to: capability for 3D digital angiography (or digital subtraction angiography) for vascular interventions (example vascular stent placement) [Noel *et al.* 2006, Orth *et al.* 2008], cross-sectional imaging for guided biopsies [Orth *et al.* 2008], and standard realtime fluoroscopy imaging [Hofstetter *et al.* 1999].

Conventional helical multi-detector CT scanners are the primary method of high-quality 3D CT imaging, most often used for diagnostic imaging. The use of these systems for 3D interventional guidance during procedures has various complications including in room size constraints and procedural time constraints which would undoubtedly affect the diagnostic CT work-flow. For many (if not all) interventional procedures use of conventional CT scanners is simply not feasible for 3D imaging and guidance [Orth *et al.* 2008].

Mobile isocentric C-arm systems are designed to allow 3D intra-procedural CT guidance with the additional capabilities of providing realtime fluroscopic imaging, 3D digital angiography, and cross-sectional imaging [Orth *et al.* 2008]. Physicians are able to image patients during interventional procedures in order to locate various tools or organs of interest and continue or adapt their treatment accordingly. Multiple two-dimensional (2D) images of the stationary patient positioned at the isocenter can be obtained while the system rotates around the gantry to allow 3D image reconstruction. The mobile

system can be moved into place when needed and removed after image acquisition.

C-arm scanners use a cone-beam x-ray source and a 2D flat panel detector to produce 2D projection images with sub-millimeter resolution. The scanner can collect 2D projection images over more than 180^o to produce 3D reconstructed images using short-scan [Parker 1982] cone-beam reconstruction algorithms such as Feldkamp reconstruction [Feldkamp *et al.* 1984]. Reconstruction algorithms require that the precise geometry of the scanner during acquisition is known.

In contrast to conventional diagnostic CT machines in which the source and detector positions are fixed to the gantry ring and move with a known rotation, mobile C-arm systems suffer from mechanical instabilities, and gravitational affects during orbital rotation which significantly alter the source and detector location from its ideal circular trajectory [Jaffray *et al.* 2002b, Maier *et al.* 2011, Daly *et al.* 2008]. (See Fig. 1.1 for a labeled image of a C-arm.) Thus, in order for accurate 3D image reconstruction the precise position and orientation of the source and detector must be measured by a process of scanner (or equivalently camera) calibration.

Calibration of a 3D cone beam system is characterized by nine geometric calibration parameters: three intrinsic parameters describing the geometry of the camera (ie. the source position relative to the detector) and six extrinsic parameters establishing the position and orientation of the x-ray imaging system in some world coordinate frame. More specifically, the extrinsic parameters designate a three parameter translation from the world coordinate frame to the source and three parameters defining the orientation of the detector relative to that frame. The world coordinate frame is usually specified by the some calibration object frame. Either the nine geometric calibration parameters can be determined separately (for example by direct inversion formula as in [Noo *et al.* 2000, Mennessier *et al.* 2009, Cho *et al.* 2005]) or simply the twelve parameter 3D to 2D projective mapping which describes the imaging system can be identified.

The typical approach to C-arm calibration involves imaging of a known phantom of x-ray opaque markers placed in the isocenter as the C-arm rotates during scan acquisition [Strobel *et al.* 2003, Cho *et al.* 2005, Mennessier *et al.* 2009, Noo *et al.* 2000]. The 2D imaged positions of the markers with known 3D geometry provides the calibration for that view of the scan. The calibration parameters of each view of the scan are stored to be applied during reconstruction of all subsequent scans. This approach is generally termed "off-line" calibration.

Offline calibration requires the assumption that the C-arm source and detector fluctuations during orbital rotation are identical in the calibration scan and the scan to be reconstructed. Thus the non-ideal C-arm motion during rotation is reproducible (short-

term reproducibility). Further the calibration technique must be performed regularly to account for possible variability in the long-term reproducibility.

Daly et al. [Daly *et al.* 2008] and Siwerdsen et al. [Siewerdsen *et al.* 2005] have studied the long and short term reproducibility of the source and detector orbit. Daly et al. show that the short-term reproducibility ($\approx$ 4 hours) was highly reproducible, however their study involved a modern C-arm scanner under ideal conditions. Other studies have reported that the assumption of C-arm scanner reproducibility may not be viable [Strobel *et al.* 2003, Mitschke *et al.* 2000, Navab *et al.* 1996]. The long term reproducibility over weeks to months noticeably showed a reduction of image quality [Daly *et al.* 2008, Siewerdsen *et al.* 2005]. Furthermore Siwerdsen et al. [Siewerdsen *et al.* 2005] studied the effect of the C-arm angluation on image reconstruction. There was a significant degradation of reconstructed image quality when the angulation of the C-arm scan differed from the angulation of the initial calibration scan.

Provided that the C-arm system has high short term reproducibility, the offline calibration procedure is performed regularly (on the order of weeks to months) and performed at the same angulation as the scan to be reconstructed, offline calibration should be sufficient for reconstruction purposes. Nevertheless, a calibration procedure which measures the geometry of the scanner from the same data set to be reconstructed (ie. the calibration and acquisition scans are the same) would undoubtedly provide a benefit over the standard offline calibration method. Scanner calibration which measures the geometry of the scanner from the same image set to be reconstructed is commonly called "on-line" calibration.

Some online methods simply use the image based approach in which the fiducial markers used for calibration are scanned with the object in the field of view (FOV) [Mitschke & Navab 2003]. The overlapping markers are then removed from the 2D image after calibration but before reconstruction. In this case both the markers used for calibration interfere with the image of the object to be reconstructed, and the object may cause a loss in precision of the localization of the calibration markers [Mitschke *et al.* 2000].

Alternatively, the markers may be placed in an area of the image which is separate from the imaged area to be reconstructed [Navab *et al.* 1996]. Calibration errors can result when the markers do not completely span the 2D field of view [Strobel *et al.* 2003] and additionally irradiation of the calibration markers outside the patient volume to be reconstructed usually results in irradiation of the patient which is undesirable when not completely necessary.

Some other online methods rely on an external tracking system to measure the mechanical flex and geometry of the C-arm system as it rotates during a scan [Mitschke

et al. 2000, Amiri *et al.* 2013]. These non image based approaches can be potentially error prone and may not provide a suitable reconstruction image quality [Mitschke *et al.* 2000, Amiri *et al.* 2013]. In [Mitschke *et al.* 2000, Mitschke & Navab 2003] the reconstruction image quality of the online calibration procedure did not produce an improvement over their gold-standard offline calibration method despite the level of C-arm reproducibility.

Our approach to online calibration

In this paper we present an alternative approach towards marker-less online C-arm calibration. Our approach simply utilizes the edges of the slightly closed x-ray tube collimator to provide information about the intrinsic calibration (IC)) parameters of the C-arm. The four edges of the (square) x-ray tube collimator in the field of view, give (4x2) eight pieces of information which is equivalent to using the imaged locations of four spherical markers. Being as the calibration object is attached to the C-arm source, only information about the intrinsic parameters (position of the detector relative to the source) can be determined. The position and orientation of the C-arm relative to some world coordinate frame (extrinsic parameters) must be measured by another means before reconstruction is possible.

The collimator, or markers attached to the source, generate a planar homography between any two projection images or views in a scan. This planar homography provides an estimation of the variation of the intrinsic calibration (IC) parameters between any two views. Thus if the intrinsic calibration (IC) parameters are measured for a single view of the scan, the IC parameters for every other view of the scan can be estimated from the homography between those views. In other words, the calibration of nine parameters which fluctuate in every view/projection (three intrinsic and six extrinsic), becomes the calibration of 3 unknown static parameters and the six varying extrinsic parameters.

This approach towards intrinsic calibration using markers attached to the source has been previously studied in [Mitschke & Navab 2003]. Mitschke et al. use a plate of markers attached to the x-ray source in order to create a 'virtual detector plane' with constant intrinsic parameters [Navab *et al.* 1999, Navab & Mitschke 2001]. The markers identify the mapping to this virtual detector plane and the static intrinsic parameters are measured beforehand using an offline calibration phantom. This online method requires that the markers attached to the x-ray source are removed from the image before reconstruction. The six varying extrinsic parameters are discovered using an external visual system. The reconstructed image quality using this method was not an improvement over simply using the offline calibration method.

Gorges et al. [Gorges *et al.* 2006, Gorges 2007] implement a similar approach to intrinsic calibration by attaching a planar phantom to the flat panel x-ray detector. In this approach, the intrinsic calibration procedure is an offline procedure such that the planar markers are imaged only during calibration. This approach requires a single view intrinsic calibration by acquiring multiple images of a rotating and translating calibration phantom with a stationary C-arm(hence stationary intrinsic parameters) [Lavest *et al.* 1998].

Bronnikov [Bronnikov 1999] reported a mildly similar approach which utilized a circular calibration aperture to perform a partial calibration. The offline procedure was implemented on a non rotating industry cone-beam x-ray system for 3D image acquisition of objects which rotate on a turn table. Only two 180^o opposed images of the aperture are required (two 2D locations) along with the known focal length to calibrate for five unknown calibration parameters.

This method of intrinsic calibration (IC) has several advantages most notably that the edges of the collimator provide essentially free information about the IC parameters of the C-arm during every projection of a scan. The collimator would slightly obstruct the field of view (FOV) but also reduce the dose delivered to the patient. This reduction of the FOV could simply be compensated for by increasing the size of the flat panel detector. Furthermore, no information about the position and geometry of the collimator need to be known to provide the calibration, it is only required that the edges of the collimator are attached and fixed to the x-ray source. The main disadvantage is that this method can only measure the variation of the IC parameters between views and requires that the IC parameters of a single reference view of the scan be measured by another means. Consequently any errors in the measurement of the IC parameters of this single view are transferred to every other view, a static bias. Lastly, in order to provide 3D reconstruction a method of extrinsic calibration must be implemented and coupled with the intrinsic calibration.

Mennessier et al. [Mennessier *et al.* 2009] have developed an analytic method of C-arm calibration which can fully and individually calibrate a single projection image using a 6-ball phantom placed at the isocenter [Spencer *et al.* 2012]. Direct inversion formula have been developed which give the nine geometric calibration parameters which describe each projection image from the 2D imaged locations of the six markers and their corresponding known 3D geometry. This method can be conveniently exploited in our case to provide the single reference view IC before scanning the object as well as to provide a 'gold-standard' method of C-arm calibration to compare with our new IC technique.

In order to produce full online calibration there are many available extrinsic calibration techniques which can be implemented along with our method of intrinsic calibration to obtain the full C-arm geometric calibration. Online extrinsic calibration is not of prime interest in this study so for reconstruction purposes the most novel image based extrinsic calibration method will be implemented which requires only a four marker planar calibration object with known geometry, positioned at the isocenter of the C-arm system. This common and straightforward technique has been formulated and discussed in several references, notedly [Sturm & Maybank 1999] and [Burnier 2015].

Research summary

The goal of this research is to show that our new technique can accurately determine the IC parameters of the C-arm for every projection image acquired using only the x-ray collimator given that the IC parameters of a single view are accurately measured by another means. However, in order for this to be possible, a very accurate method of measuring the angle and position of the thick, straight edges of the projection of the x-ray tube collimator must be developed. Our technique will be evaluated in both real and simulation studies which replicate our own C-arm.

Simulation studies will first be performed using a simple four spherical marker phantom attached to the x-ray source. The objective of these studies is to validate the IC technique and show its practicality for real C-arm calibration. The IC results will be compared to the simulation ground-truth conditions and the gold-standard [Mennessier *et al.* 2009] calibration method. The initial single view IC parameters can be provided by the ground-truth simulation conditions or the gold-standard method.

Next simulation studies will be performed on a calibration phantom which imitates the edges of the x-ray tube collimator in the field of view. These simulation studies will be used to investigate and discover the most accurate method of measuring the precise location of edges in an x-ray projection image. These simulation studies will be assessed based on their performance relative to the ground-truth simulation conditions. Subsequently this method of edge detection will be applied to real data from an isocentric C-arm scanner with the collimator in the field of view (FOV).

Finally, the developed method of IC using the collimator edges in the FOV will be evaluated through 3D image reconstruction using the Reconstruction toolkit (RTK) [Rit *et al.* 2014].

The method of intrinsic calibration is a common technique from the field of computer vision and a similar concept of creating a virtual detector plane with static intrinsic

parameters has been reported and patented by Navab and Mitschke [Mitschke & Navab 2003, Navab *et al.* 1999, Navab & Mitschke 2001]. These works are notably different from this research because they only use markers attached to the x-ray source, there is no inquiry into using the collimator, and instead of a method of single view intrinsic calibration they use a full intrinsic and extrinsic calibration.

This research marks the first known instance of attempting to use the x-ray tube collimator in the field of view to provide information about the calibration of a C-arm, although the idea has previously been patented by Schuetz [Schuetz 2001, Schuetz & Mitschke 2002]. These patents describe a process of measuring the intrinsic calibration parameters using either a marker plate or the x-ray tube collimator which may contain structures attached to (or removed from) the x-ray collimator. The claims outlined in these patents are notably different from this work as they require that the markers or collimator edges lie in the same plane, and further that the positions of the markers or collimator edges are known (or measured) relative to each other and the x-ray source position.

Secondly this research is the first reported investigation into the accurate measurement of the edges of the x-ray tube collimator in a projection image. Line or edge detection in computer vision has been extensively studied and reported (see Chapter 3 for an overview). In x-ray images, line or edge detection has been previously studied for a few different applications, such as: vascular tree identification and image enhancement [Coppini & Demi 1993], ridge detection for multi-modality image matching [Maintz *et al.* 1996], and also for the detection of the collimator edges simply for the purpose of automated removal of these edges from projection images (a process which has no requirement for accuracy). In contrast to these works, the research presented in this work proceeds with an intense and thorough investigation into the accuracy of edge detection with the objective of obtaining the highest possible degree of precision - on the order of $1/10^{th}$ of a pixel in the edge position, and $1/100^{th}$ of a degree in angular precision.

1.2 Materials, Methods and Context for the Following Research

This section will introduce the necessary apparatus, methods and context which will be used in the following chapters. The C-arm used for real data acquisition is described, an explanation of the simulation program used in all simulation studies is given, and a brief review of projective geometry provides the context and useful formula utilized in this research.

1.2.1 Isocentric C-arm x-ray imaging system

An isocentric C-arm x-ray imaging system capable of 2D image acquisition was used in this study (see Fig. 1.1). The system is composed of an x-ray tube (or source), which generates x-rays via Bremsstrahlung and fluorescence and a Trixell flat panel detector to measure the x-ray signal to produce 2D projection images. The C-arm is designed to allow the source and detector to rotate along the C shaped gantry while obtaining projection images of the patient or object placed in the isocenter. The C-arm is capable of acquiring projection images over 199^o for cone-beam computed tomography 3D image reconstruction. A reconstruction technique such as the Feldkamp, FDK, method or iterative reconstructions methods [Feldkamp *et al.* 1984, Noo 1998] would be used to create a 3D image from the 2D projections acquired during the gantry rotation.

In the ideal situation the source and detector would follow a perfect circular trajectory as they rotate along the gantry. However due to gravity effects and mechanical instabilities the source and detector undergo a significant amount of non ideal motion. Furthermore vibrations of the source and detector can result and begin to amplify during rotation. In consequence, the non-ideal motion, the deformation from a circular orbit, must be measured in order to produce acceptable 3D image reconstructions. This involves measurement of the source position, detector position, and detector orientation for every projection image of the scan.

The flat panel detector consists of a 1560×1440 pixel array with a pixel size of 0.182×0.182 mm^2. The x-ray source to the detector distance is 1198 mm, and the x-ray source to center distance is 665 mm. Additionally the x-ray source contains its own built in collimator which can be controlled manually.

For all experiments presented in this work the images were acquired from the C-arm in pulsed-fluoroscopy mode with 40 kV and 2 mAs (50 ma pulse with 25 frames

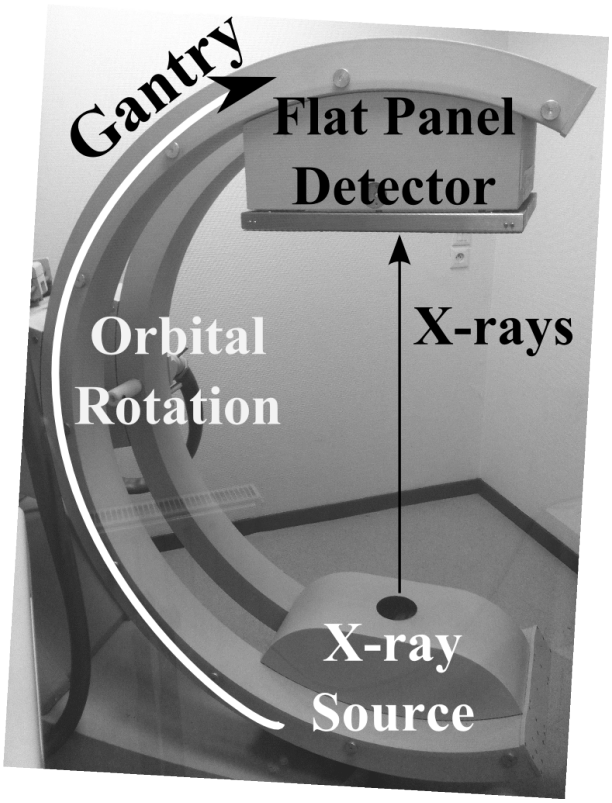

Figure 1.1: Isocentric C-arm x-ray system.

per second). Generally, patient scans would be obtained with a tube voltage in the range of 80 - 120 kV and a current depending on the patient size (roughly to 2 mAs). For object-less scans a tube voltage of 40 kV and current of 2 mAs is most often used. This lower than usual tube voltage would have some affect on the characteristics of the projection image however there is no clear advantage or disadvantage for this lower voltage compared to the typical patient voltage.

1.2.1.1 X-ray tube collimator

The x-ray tube contains a built in collimator which can be automatically adjusted by the user. Approximate measurements of the collimator indicate that its thickness is, $t \approx 3$ mm thick, and distance from the source is, $d \approx 130$ mm. A projection image, Fig. 1.2, shows that the collimator edges are somewhat different widths in the image. An approximate measurement of the edges displayed in Fig. 1.2(a) yields: $L = 64 \pm 5$pixels, $R = 27 \pm 2$pixels, $T = 42 \pm 2$pixels, $B = 55 \pm 5$pixels.

When obtaining a full scan of the collimator over 192^o the edges of the collimator exhibit clear and smooth motion as illustrated by the projection of the collimator at two different angles seen in Fig. 1.2. This movement of the collimator edges indicates that the source and detector movements (C-arm deformation) during orbital rotation affects the intrinsic parameters of the C-arm imaging system.

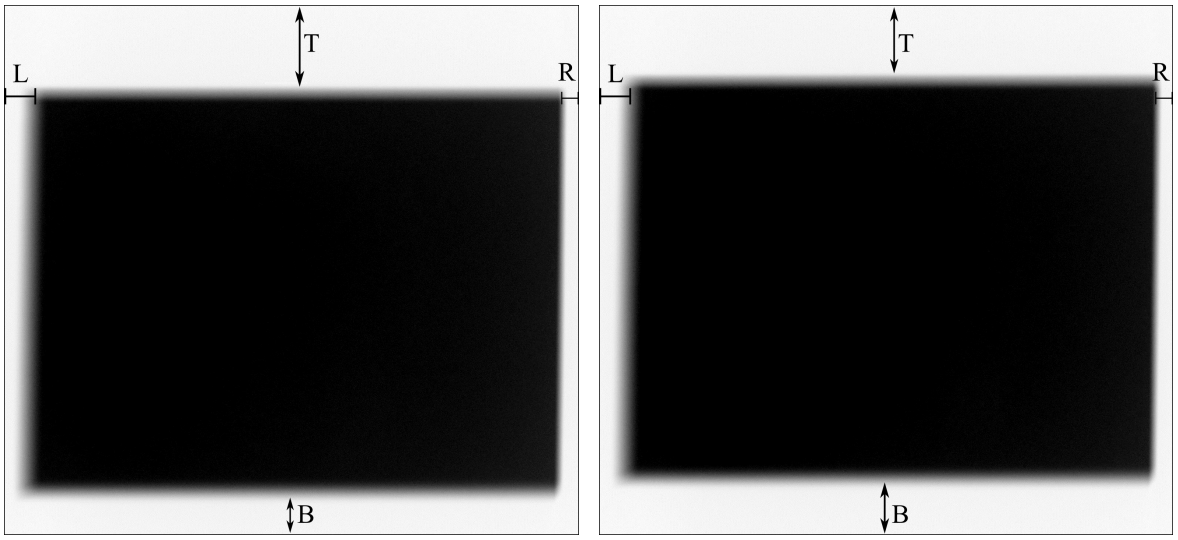

(a) Projection of collimator edges at 20^o (b) Projection of collimator edges at 160^o

Figure 1.2: Projection images of the x-ray tube collimator in the field of view. (a) corresponds to an image at orbital angle 20^o while (b) is at 160^o. The projection of the collimator edges in (b) is visually higher than the edges in (a).

1.2.1.2 Brief explanation of x-ray projection

An x-ray projection is produced by emitting a flux of x-rays (or photons) which travel through the object and are measured by the detector. The value measured on the detector is dependent on the number of x-rays which pass through the object to reach the detector. Roughly speaking, the number or ratio of incident photons which pass through the object is inversely proportional to the density of the object and the amount of mass which the x-rays must traverse. The relationship is given by the Beer-Lambert law of transmittance:

$$\tau = \exp\left(-\int_0^L \mu(z)\,\mathrm{d}z\right) \tag{1.1}$$

where τ gives the ratio, or probability that the photons will pass through the object of thickness Δz and attenuation coefficient $\mu(z)$. The attenuation coefficient is specified by the material and density of the object and thus designates the ratio of transmittance through the object and subsequently the recorded intensity on the detector. Furthermore, the attenuation coefficient is a function of the energy of the incident photons but for our purposes we will assume the x-ray source produces a mono-energetic beam of photons.

Thus the intensity, I, of any pixel (i, j) in the measured projection image is given by:

$$I_{(i,j)} = I_{0(i,j)} \exp\left(- \int_0^L \mu(z)_{(i,j)} \, \mathrm{d}z \right) \tag{1.2}$$

where $I_{0(i,j)}$ is the max intensity measured at that pixel without an object in the field of view, and $\mu(z)_{(i,j)}$ designates the attenuation coefficient of the object along the line L between the source and the pixel.

1.2.1.3 Noise measurement

The measurement of the noise in a standard measurement image is necessary for the production of realistic simulation images with noise. The noise measurement must be attained from an image which resembles a typical image of a patient or object of interest. Thus, for our purposes the measurement was done with a water phantom in the image FOV with 40 kV and 2 mAs (following our standard imaging conditions). As is the case with most C-arms, the images generated are enhanced with electronic gain. In order to measure the level of noise of an x-ray image the image must first be gain corrected. This involves simply dividing our standard measurement image, I_m, with a flood field gain correction image which contains nothing in the field of view, denoted I_0. Lastly, the negative of the ln of the image is taken, yielding $-\ln \frac{I_m}{I_0}$, and the average of the standard deviation of the intensity fluctuations in the image are measured to give an accurate measurement of the image noise. The average noise in a typical image was found to be: $\sigma_N = 0.4213$ (in gray level units of $\ln \frac{I_m}{I_0}$).

When considering the measurement of photons on a flat panel detector the photon noise follows a Poisson distribution. However when the number of measurements is very large, which is certainly the case with x-ray imaging systems, the Poisson distribution can be well approximated as a normal distribution with the standard deviation σ_N.

1.2.1.4 Gold-standard calibration phantom

To provide an alternative and gold-standard calibration method a six marker offline calibration phantom was designed and fabricated. The offline calibration method has been proposed by Mennessier et al. [Mennessier *et al.* 2009] and previously implemented in [Spencer *et al.* 2012]. This calibration procedure can fully and individually calibrate each projection image using the 2D imaged and known 3D locations of the 6-marker phantom.

The phantom was fabricated in PMMA (lucite) material. This material has a high durability and low radio opacity in an x-ray image. The six markers were provided by six spherical steel ball-bearings of 2.5 mm diameter. The design was based on the following necessary criteria (in order of importance):

- accuracy of positioned markers on phantom
- good visibility of markers in image - removal of background phantom material that may reduce measurement accuracy of marker location in image
- simple and easy phantom alignment

The design of the phantom was as follows:

1. The six markers were placed in the middle of the six faces of a rectangular prism of size $100 \times 80 \times 60$ mm^3.
2. The corners of the phantom were cut at a precise angle to allow easy alignment.
3. The center of the cube was bored out in order to remove the radio opaque material which may reduce the visibility of the markers during a scan.

Relative to the center of the phantom, the six markers are positioned at: (50,0,0),(0,40,0),(0,0,30),(-50,0,0),(0,-40,0),(0,0,-30), with all units in mm. These markers were machined to within 0.020 mm precision.

A figure showing a picture and an x-ray projection of the phantom can be seen in Fig. 1.3.

1.2.2 Review of projective geometry

This section is intended to give a dense overview of some well known and integral topics of computer vision which will be used throughout this study. If the reader is familiar with computer vision and projective geometry this section will be readily apparent to her/him

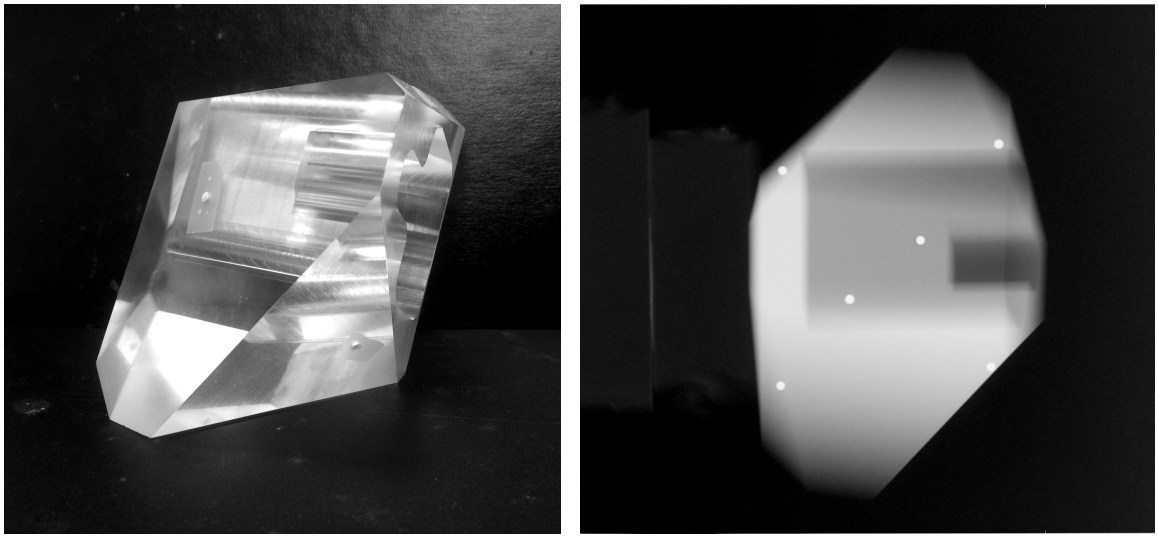

(a) Picture of gold-standard calibration phantom (b) X-ray image of gold-standard phantom

Figure 1.3: A picture, and x-ray projection of the six marker gold-standard calibration phantom. Note that the ten sided semi-transparent object is difficult to discern in both the x-ray projection and picture.

however if the reader is unfamiliar with these topics for a better explanation they should consult one or all of the following resources: the textbook 'Multiple View Geometry in Computer Vision' by Hartley and Zisserman [Hartley & Zisserman 2004], or the textbook 'Three-dimensional Computer Vision: A Geometric Viewpoint' by Faugeras [Faugeras 1993], or the lecture note from Sturm entitled 'Some lecture notes on Geometric Computer Vision' [Sturm 2013], among other possible resources. This review will cover the following four topics:

1. The camera model and the projective matrix
2. Camera calibration: intrinsic and extrinsic
3. Homography
4. General solution to the projective matrix or homography identification

The notation of this section closely resembles that of Hartley and Zisserman [Hartley & Zisserman 2004] and is similar to Sturm [Sturm 2013].

1.2.2.1 Camera model and the projective matrix

A camera projects the 3D world onto a 2D image. There are two types of camera models: the standard pin-hole camera (used in computer vision) and the direct imaging camera which models the C-arm x-ray imaging system. Both models are analogous and both contain the following variables listed in the below chart, and shown in Fig. 1.4. From here on we will be considering the direct imaging camera model which pertains to our C-arm x-ray imaging system.

Variable	Pin-hole Camera	Direct Imaging Camera
$\vec{\mathbf{s}}$	optical center	source
$\mathbf{R}(\Phi, \Theta, \eta)$	image plane orientation	detector plane orientation
(f, u_s, v_s)	focal length along optical axis & principle point	focal length & orthogonal proj. of source onto detector
$\mathbf{X}_1 = (X, Y, Z)$	3D point (relative to world frame)	
$\mathbf{x}_1 = (u, v)$	projection of 3D point (image frame)	

It is important to note that the 3D point, $\mathbf{X}_1$, source position, $\vec{\mathbf{s}}$, and detector orientation, $\mathbf{R}(\Phi, \Theta, \eta)$, are relative to the (arbitrary) world coordinate frame. The orthogonal projection of the source onto the detector is in pixel units and in the reference frame of the detector with the origin of the detector being the (0,0) pixel position.

Now to show a simple projection of the 3D point $\mathbf{X}_1$ onto the detector assuming the world coordinate frame is located at the source position and parallel to the orientation of the detector:

$$\begin{bmatrix} u \\ v \\ 1 \end{bmatrix} \sim \begin{bmatrix} w * u \\ w * v \\ w \end{bmatrix} \sim \begin{bmatrix} f & 0 & u_s & 0 \\ & f & v_s & 0 \\ & & 1 & 0 \end{bmatrix} \begin{bmatrix} X \\ Y \\ Z \\ 1 \end{bmatrix} = \mathbf{K}\mathbf{X}_1 \tag{1.3}$$

This implementation employs the use of homogeneous coordinates to designate the projection and note that the projection is only known up to scale being as any 3D point along the line from the point to the optical center would project to the same (u, v) location on the detector. Furthermore, this projection uses the assumptions that the (u, v) pixels are square, and orientated perpendicularly to each other, which is the case

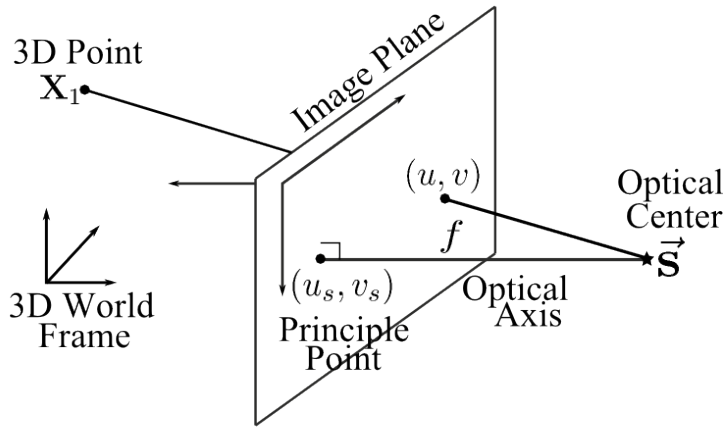

(a) Pin-hole camera model

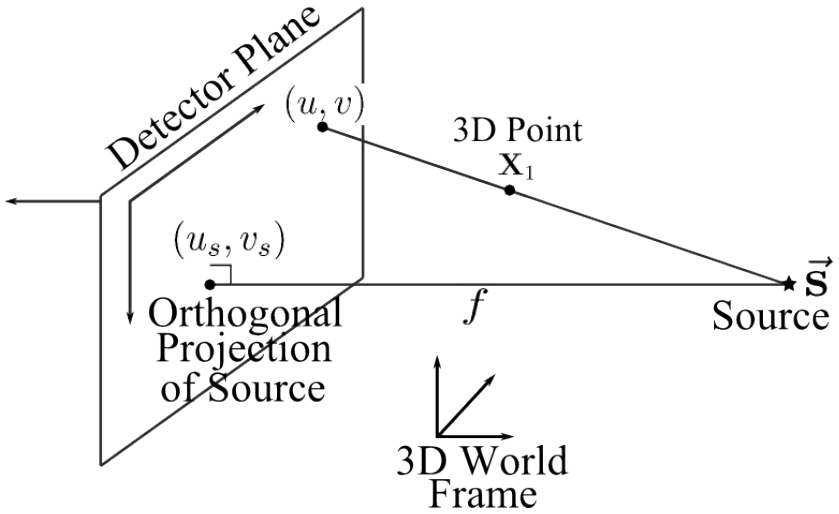

(b) Direct imaging camera model

Figure 1.4: Diagram depicting the geometry and relevant variables for the (a) pin-hole camera model, and (b) direct imaging camera model. All variables are in the world coordinate reference frame.

for almost all modern detectors/cameras.

In the likely event that the world coordinate frame is not parallel to the detector orientation and the source position is not at the origin of the world frame the 3D point

$\mathbf{X}_1$ must first be rotated by the 3×3 rotation matrix $\mathbf{R}$ (designated by the Euler angles (Φ, Θ, η) and translated by $\mathbf{t}$ before projection:

$$\begin{bmatrix} u \\ v \\ 1 \end{bmatrix} \sim \mathbf{K} \begin{bmatrix} \mathbf{R} & |\mathbf{t} \end{bmatrix}_{(3\times4)} \begin{bmatrix} X \\ Y \\ Z \\ 1 \end{bmatrix} \sim \mathbf{K} \begin{bmatrix} \mathbf{R} & |\mathbf{t} \end{bmatrix}_{(3\times4)} \mathbf{X}_1 \tag{1.4}$$

Using this notation the source position $\vec{\mathbf{s}}$ is given by $\vec{\mathbf{s}} = -\mathbf{R}^T\mathbf{t}$.

This completes the camera model description of a 3D to 2D projection. The resulting matrices are often expressed by the 3×4 projection matrix $\mathbf{P}$: $\mathbf{P} \sim \mathbf{K} \; [\, \mathbf{R} \mid \mathbf{t} \,]$.

1.2.2.2 Camera calibration

The projection matrix $\mathbf{P}$ describes how the 3D objects project onto the 2D image. Estimation of this projection matrix allows the reconstruction of the 3D scene from multiple 2D projections. The 3D to 2D projection is characterized by 9 unknown parameters which can be separated into intrinsic parameters, those which express the geometry of the camera, and extrinsic which identify the location of the camera in the world coordinate frame. The three intrinsic parameters are defined by the orthogonal projection of the source onto the detector, matrix $\mathbf{K}$ (Eqn. (1.3)&(1.5)), while the six extrinsic are represented by the three parameter rotation matrix $\mathbf{R}$ and the three parameter translation $\mathbf{t}$.

$$\mathbf{K} = \begin{bmatrix} f & 0 & u_s \\ & f & v_s \\ & & 1 \end{bmatrix} \tag{1.5}$$

Camera calibration generally involves the process of estimating the 3×4, 12 parameter (up to scale), projection matrix $\mathbf{P}$ using a calibration object, or phantom, which designates the world coordinate frame. Afterwards, if necessary, the projection matrix can be separated into it's intrinsic and extrinsic components. Alternatively, the intrinsic calibration parameters can be measured separately when using a phantom which is in the reference frame of the camera.

A typical calibration object would consist of multiple 3D markers with known geometry relative to the calibration object and which are easily distinguishable on the 2D image. Using the 3D coordinates of the marker in the world frame, $\mathbf{X}_i$ and the associated 2D projection, $(u, v)_i$, gives one solution to equation (1.4). The projection of six

3D markers produces twelve equations (u/v position of six markers) which can uniquely determine the projection matrix $\mathbf{P}$. (More details on this solution are described below).

1.2.2.3 Homography

Homography describes the mapping of a 2D point (or points) from one projection/view to another, see figure 1.5. This plane to plane mapping is defined (up to scale) by the 3×3 matrix, $\mathbf{H}$:

$$\mathbf{x}'_1 \sim \mathbf{H}\mathbf{x}_1$$

Any points contained on the plane Π which have been imaged in one view can be located in another using the homography between the two views. Additionally, the imaged locations of 3D points on a plane can be utilized to solve the homography which is dependent on the imaging system.

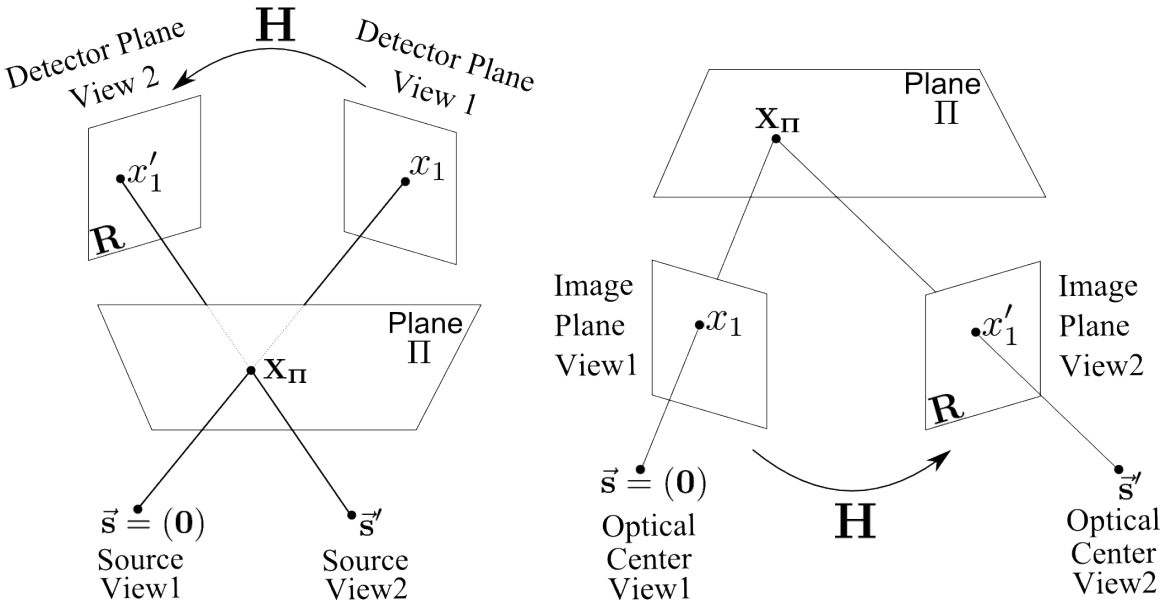

(a) Homography - direct imaging camera model

(b) Homography - pin-hole camera model

Figure 1.5: A diagram of the homography model as it applies to (a) direct imaging systems and (b) pin-hole imaging systems.

From figure 1.5 the projection of a marker, $\mathbf{X_\Pi}$, lying on the plane Π is expressed

using equation (1.4) in two views by:

$$\mathbf{x}_1 \sim \mathbf{K}\,[\,\mathbf{I} \mid 0\,]\,\mathbf{X}_\Pi \qquad \mathbf{x}'_1 \sim \mathbf{K}'\,[\,\mathbf{R} \mid \mathbf{t}\,]\,\mathbf{X}_\Pi \tag{1.6}$$

where $\mathbf{R}$, and $\mathbf{t}$, are the extrinsic calibration parameters of the second view relative to the coordinate system of the first view, and $\mathbf{K}$, and $\mathbf{K}'$ are the intrinsic calibration parameters of first and second views respectively and the source position in the second view is $\vec{\mathbf{s}'} = -\mathbf{R}^T\mathbf{t}$. Given that the plane, Π, is described by the equation $\Pi = (\mathbf{n}^T, d)$ where $\mathbf{n}$ is the normal of the plane and d is the plane's distance from the origin the resulting homography takes the form:

$$\mathbf{H} \sim \mathbf{K}'(\mathbf{R} - \mathbf{t}\mathbf{n}^T/d)\mathbf{K}^{-1} \tag{1.7}$$

Recall that the homography is only defined up to scale and not exact equality, therefore the homography matrix contains 9 parameters but only 8 degrees of freedom. To solve the homography between two views at least four 3D markers on a plane must be imaged in the two views.

1.2.2.4 General solution to the projective matrix or homography

Recall that in order to solve the 12 parameter (up to scale) projection matrix ((1.4)), at least six 3D to 2D point correspondence are required, while the 8 parameter homography matrix (9 parameters up to scale) requires at least four 2D to 2D point correspondences. In both cases the correspondences provide a linear system of equations and both matrices can be solved by a simple single value decomposition.

For explanation purposes we will consider the solution to the homography matrix. Each point correspondence provides two linear equations:

$$\begin{bmatrix} u'_1 \\ v'_1 \\ 1 \end{bmatrix} \sim \mathbf{x}'_1 \sim \mathbf{H}\mathbf{x}_1 \sim \mathbf{H} \begin{bmatrix} u_1 \\ v_1 \\ 1 \end{bmatrix}$$

$$u'_1 = \frac{(\mathbf{H}\mathbf{x}_1)_1}{(\mathbf{H}\mathbf{x}_1)_3} \qquad v'_1 = \frac{(\mathbf{H}\mathbf{x}_1)_2}{(\mathbf{H}\mathbf{x}_1)_3}$$

$$u'_1(H_{31}u_1 + H_{32}v_1 + H_{33}) = H_{11}u_1 + H_{12}v_1 + H_{13}$$

$$v'_1(H_{31}u_1 + H_{32}v_1 + H_{33}) = H_{21}u_1 + H_{22}v_1 + H_{23}$$

All four point correspondences can be utilized in this way to construct a single linear equation system of the form $\mathbf{Az} = 0$ where the vector $\mathbf{z}$ is composed of the entries of $\mathbf{H}$ and $\mathbf{A}$ contains the four point correspondences (Eqn. (1.8)). Finding the null space of the matrix $\mathbf{A}$ yields the unique solution of the matrix $\mathbf{H}$.

$$\left[\begin{array}{ccccccccc} u_1 & v_1 & 1 & 0 & 0 & 0 & -u_1u_1' & -v_1u_1' & -u_1' \\ 0 & 0 & 0 & u_1 & v_1 & 1 & -u_1v_1' & -v_1v_1' & -v_1' \\ \hline u_2 & v_2 & 1 & 0 & 0 & 0 & -u_2u_2' & -v_2u_2' & -u_2' \\ 0 & 0 & 0 & u_2 & v_2 & 1 & -u_2v_2' & -v_2v_2' & -v_2' \\ \hline \cdots & \cdots & \cdots & & & & & & \\ \vdots & & & & & & & & \\ \hline u_m & v_m & 1 & 0 & 0 & 0 & -u_mu_m' & -v_mu_m' & -u_m' \\ 0 & 0 & 0 & u_m & v_m & 1 & -u_mv_m' & -v_mv_m' & -v_m' \end{array}\right] \left[\begin{array}{c} H_{11} \\ H_{12} \\ H_{13} \\ H_{21} \\ H_{22} \\ H_{23} \\ H_{31} \\ H_{32} \\ H_{33} \end{array}\right] = 0 \tag{1.8}$$

where m is the number of markers.

Summary of useful formula from projective geometry

Projection Matrix	Proj. 3D point onto 2D image	$(u, v, 1)^T \sim \mathbf{PX_1} \sim \mathbf{K}\left[\begin{array}{cc} \mathbf{R} & \vert\mathbf{t} \end{array}\right]\mathbf{X}_1$
Intrinsic Calibration	Specifies geometry of camera	$\mathbf{K} = \left[\begin{array}{ccc} f & 0 & u_s \\ & f & v_s \\ & & 1 \end{array}\right]$
Extrinsic Calibration	Position/orientation of camera in world frame	$\mathbf{R}(\Phi, \Theta, \eta)$ $\vec{\mathbf{s}} = -\mathbf{R}^T\mathbf{t}$
Homography Matrix	2D image to 2D image mapping	$\mathbf{x}_1' \sim \mathbf{Hx}_1$ $\mathbf{H} \sim \mathbf{K}'(\mathbf{R} - \mathbf{tn}^T/d)\mathbf{K}^{-1}$

1.2.3 Simulation program

A simulation program was designed to generate 2D projection images with an identical geometry as the C-arm described in section 1.2.1: Image size of 1560×1440 pixels, pixel size of 0.182 mm^2, source to detector distance of 1198 mm and source to center distance of 665 mm. The program can simulate the projection of ellipsoids (or spheres) and parallelepipeds (which create lines on a 2D image) which can be utilized to designate

a known phantom object for experimentation. The simulation can allow the variation of the source position, the detector position, and the detector orientation during image generation. Further, the generated phantom or object may be positioned at the isocenter while the source and detector rotate around it or fixed to rotate with the same orbital rotation as the source.

The 2D x-ray projection images of the object are produced by employing the Radon transform to compute the value of each pixel on the detector. For each pixel the line, L, which passes from the pixel to the source, through the object, is found and the pixel value is computed by the integral of the object mass density along this line. In this case the pixel value, I is given by: $I_{(i,j)} = \int_0^L f(z)_{(i,j)}\,\mathrm{d}z$ where $f(z)_{(i,j)}$ designates the object mass density along the line L between the source and the pixel (i, j).

This method of computing the pixel intensity is notably different from the above Beer-Lambert law of transmittance seen in Eqn. (1.1). The simulation generated images actually give a measure of the negative of the ln of the intensity of an x-ray projection image, $-\ln\dfrac{I}{I_0}$. In any case the simulation generated images are easily comparable to the real projection image by simply pre-processing either the real or simulated generated images to match each other.

1.2.3.1 Noise treatment

The simulation program mimics the x-ray image generation of the real C-arm however it produces noiseless images. Before image processing, noise is added to the generated images to replicate the level of noise in the real C-arm projection images. Noise was measured from the C-arm during normal conditions of operation (section 1.2.1.3). This noise was added to the simulated images using ImageJ [Abràmoff *et al.* 2004] as Gaussian noise with the same standard deviation and zero mean. A comparison of the image quality of the real and simulated data can be seen in figure 1.6.

1.2.3.2 Simulated phantoms

The simulation program generated projection images of three designated phantoms. The first, shown in Fig. 1.6(a), simply contains four spheres at the corners of the image field of view which were rigidly fixed to the x-ray source such that when the source rotates around the isocenter the phantom rotates with it. The second is similar to the first except that parallelepiped objects were simulated at the corners of the image which rotate with the same orbital rotation as the source. These parallelepipeds result in lines or edges in

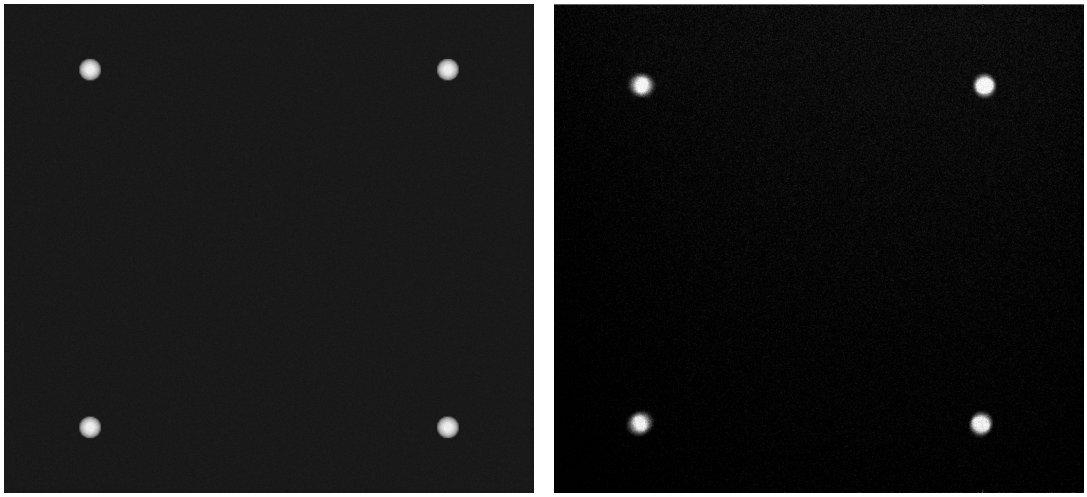

(a) Simulated image with noise (b) Gain corrected real image

Figure 1.6: An example of a simulated projection image with added Gaussian noise with a gain corrected real projection image. In both images the size of the markers is the same (1.25 mm radius) while the distance from the source and dimensions are approximate in the real projection image.

the field of view which resemble the slightly closed edges of the x-ray tube collimator, see Fig. 1.7(a). The phantom was created such that the position and thickness of the parallelepipeds produces a simulated image in which the width of the edges is roughly the same as the real image of the collimator, Fig. 1.7(b).

Lastly six spherical markers positioned around the isocenter with precisely known 3D locations (see Table 1.1) were simulated to provide our gold-standard calibration phantom [Mennessier *et al.* 2009, Spencer *et al.* 2012]. The simulated and a real projection image of the gold-standard calibration phantom is shown in Fig. 1.8.

The specifications of all three phantoms can be seen in Table 1.1.

1.2.3.3 Simulated C-arm deformation

The six parameters which characterize the detector position and orientation relative to the source are: z_d, y_d, x_d, Φ, Θ, η. In the absence of detector rotation the z-axis is orthogonal to the detector, (thus $z_d = f$), whereas the y-axis is parallel to the detector u-axis and x is parallel to the v-axis. The angle Θ defines a rotation about the v-axis, while Φ defines a rotation about the u-axis which is parallel to the axis of orbital rotation.

Table 1.1: Simulated phantom specifications. The positions of the phantoms are given relative to the isocenter of the system. The collimator phantom positions indicate the corners of the parallelepipeds at the midpoint of their thickness.

Simulated Phantom	radius or thickness [mm]	marker or edge positions [mm]	Distance from source [mm]
Planar 4 markers	r =1.00	$(+12,+12,-507.5)$,$(+12,-12,-507.5)$ $(-12,+12,-507.5)$,$(-12,-12,-507.5)$	157.5
Collimator 4 edges	t =15	$(+14,+14,-507.5)$,$(+14,-14,-507.5)$ $(-14,+14,-507.5)$,$(-14,-14,-507.5)$	157.5
Gold-standard 6 markers	r =1.25	$(50,0,0),(0,40,0),(0,0,30)$ $(-50,0,0),(0,-40,0),(0,0,-30)$	isocenter

The in plane detector rotation (rotation about the z-axis) is defined by η.

These six deformation parameters were altered individually or all six simultaneously by a random deviation. The random simulated deformation was based roughly on the deformation measured by Daly et al. [Daly *et al.* 2008] from a similar C-arm. Their study utilized a C-arm with a source to detector distance of 1225 mm (our C-arm: 1198 mm), source to center distance of 637 mm (ours: 665 mm), pixel array of 2048×1536 with size 0.194 mm^2 (our C-arm: 1560×1440 with 0.182 mm^2). The detector and geometries are similar between the two C-arms however their C-arm was of considerably better quality in terms of mechanical stability therefore we can assume our level of C-arm deformation is substantially greater.

The random deformation of the detector was characterized by a Gaussian distribution in which the standard deviation (SD) of each parameter was designated by the maximum measured deformation of the C-arm in Daly et al. [Daly *et al.* 2008]. The maximum simulated deformation was capped at twice the value of the SD (twice the value of the max measured by Daly et al.), or at the maximum observable deformation for the y_d parameter due to the limitation of image size (u_{size} = 1440 pixels). These values are summarized in Table 1.2.

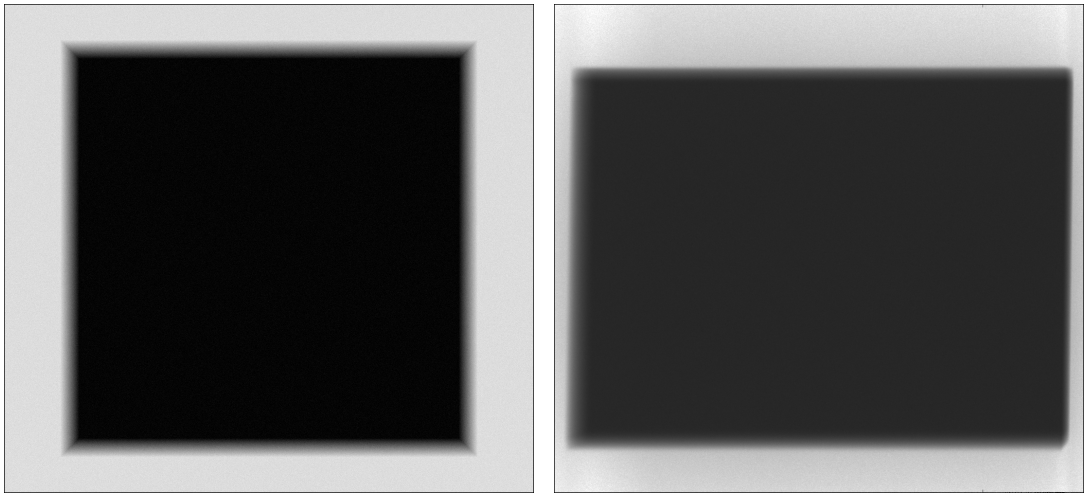

(a) Simulated colimator image with noise (b) Gain corrected real image of x-ray tube collimator

Figure 1.7: An example of a simulated projection image of the x-ray tube collimator with added Gaussian noise, and a gain corrected real image of the edges of the slightly closed x-ray tube collimator.

Table 1.2: The maximum and standard deviation of the varied C-arm deformation parameters for simulation experiments.

Calibration Parameter	z_d [mm]	y_d [mm]	x_d [mm]	Φ [deg]	Θ [deg]	η [deg]
Standard deviation	13.8	12.8	12.8	2.4	2.4	0.8
Maximum	±27.6	±16.0	±25.6	±4.8	±4.8	±1.6

1.3 Summary

This research focuses on a new method of marker-less intrinsic calibration of a C-arm imaging system. Only the edges of the x-ray tube collimator in the field of view and a single view accurate calibration by another means, such as our gold-standard, are required. This method can be coupled with a method of online extrinsic calibration to provide full online calibration and 3D image reconstruction.

In Chapter 2 the IC technique used throughout this report is introduced. This is a commonly used technique from the literature, which has been applied to a C-arm x-ray imaging system in which the calibration object is attached and fixed to the x-ray

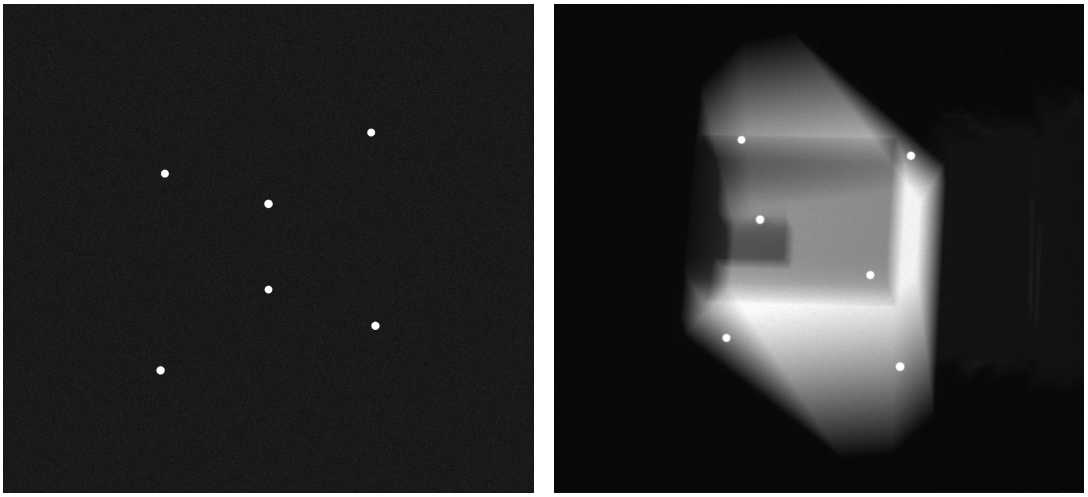

(a) Simulated gold-standard calibration phantom with noise

(b) Gain corrected real image of our gold-standard phantom

Figure 1.8: An example of a simulated projection image of our six marker gold-standard calibration phantom with added Gaussian noise, and a gain corrected real image of our gold-standard calibration phantom. Note that the positions of the markers in the two phantom images are not supposed to be at the same location being as the two phantom are at different orientations relative to the C-arm.

source. Initial evaluations of this technique are performed using simulations to validate the concept and investigate its possible limitations or sensitivities. To initially avoid the difficult process of edge detection in an x-ray image (presented in Chapter 3) the collimator edges are replaced by simulated spherical markers in the corners of the image field of view. The preliminary IC results are presented and methods of accurate single view IC are discussed.

A full detailed examination into accurately locating the collimator edges in the FOV is given in Chapter 3. This localization is an important process being as calibration is highly sensitive to errors. Edge detection in the literature is discussed and several methods of edge detection are examined through simulation studies to find the optimal detection method for collimator edges. Lastly, our optimal method of edge detection is evaluated in comparison with some commonly used line/edge detection techniques from the literature through simulation studies and also with real C-arm scans with the collimator edges in the FOV.

Chapter 4 demonstrates the application of this work to 3D image reconstruction.

Through simulation studies the geometric calibration necessary for 3D image reconstruction is provided by our method of IC using edges in the FOV along with a typical extrinsic calibration produced from a four marker planar phantom. These reconstructed images are compared with those generated from the simulation ground-truth conditions and the gold-standard calibration method.

Chapter 5 summarizes the results of this research and discusses the limitations and possible improvements to be made in the future.

Chapter 2

General Approach to Intrinsic Calibration

Résumé du Chapitre 2 en Français

Dans ce chapitre nous rappelons les méthodes de calibration intrinsèque par homographie et nous présentons des premiers résultats à partir de simulations sur des marqueurs radio-opaques. Les résultats montrent que cette approche permet de déterminer de manière très précise les variations des paramètres intrinsèques au cours de l'acquisition. Dès lors que qu'un jeu de paramètres intrinsèques est connu pour une projection radiographique de référence, la calibration intrinsèque des autres projections peut-être déterminée par cette méthode. Cependant, une erreur dans les paramètres intrinsèques de l'image de référence se propage dans les paramètres des autres projections. Nous proposons des techniques pour mesurer la calibration intrinsèque de l'image de référence. Nous avons comparé notre méthode de calibration on-line à base d'homographie avec une méthode standard de calibration globale en présence de bruit dans les radiographies et de déformations du C-arm.

Summary

This chapter outlines the derivation of the homography intrinsic calibration (IC) and presents some initial simulation evaluations to check the validity of the method and investigate some possible sensitivities it might have. Although the purpose of this research is to use the collimator edges in the field of view (FOV) to provide the intrinsic calibration (IC) of the C-arm, the simulation studies in this chapter use spherical markers instead of edges in the FOV in order to simplify initial investigations. The possible techniques which can provide the single view measurement of the IC are also discussed

and analyzed in the following.

Part of the work presented in this chapter has been previously published by the authors in Spencer and Desbat [Spencer & Desbat 2014]. Due to differences in the simulation program and conditions the results presented here are new and improved.

2.1 Homography Intrinsic Calibration Method

Planar homographies have been extensively studied and utilized for pin-hole camera calibration purposes in the field of computer vision [Sturm 2000, Hartley & Zisserman 2004]. Generally in computer vision the intrinsic calibration is often known and constant, which is not the case for C-arm systems. In some cases planar homographies have been used for calibration of both extrinsic and intrinsic parameters [Sturm & Maybank 1999]. The calibration object is always in the image FOV when using pin-hole cameras in computer vision.

Unlike methods of calibration in computer vision our technique involves four markers fixed to the source (or optical center) with unknown 3D location. The imaged positions of these markers generates a planar homography between the detector plane in one view, and the detector plane in any other view. This formulation provides significant simplification to the calibration problem, though as a consequence, only the variation of the IC parameters and the relative rotation of the detector between views can be discovered.

As the markers are fixed to the optical center it cannot designate the world coordinate frame, and thus we express the 3D position of the markers in the reference frame of the source. Using this simplification when projecting a 3D point ($\mathbf{P} \sim \mathbf{K}\ [\ \mathbf{R}\ |\ \mathbf{t}\ ]$) the translation vector which represents the source position in the world coordinate frame becomes zero: $\mathbf{t} = 0$. Additionally, the orientation of the detector is defined to be $\mathbf{I}$ in the first view, and some rotation $\mathbf{R}$ in the second. Consequently, in our simplified situation, rather than our standard projection matrix (Eqn. (1.6)), we have:

$$\mathbf{x}_i \sim \mathbf{K}\,[\,\mathbf{I}\,]\,\mathbf{X}_\Pi \qquad \mathbf{x}'_i \sim \mathbf{K}'\,[\,\mathbf{R}\,]\,\mathbf{X}_\Pi \tag{2.1}$$

where $i = 1...m$, m is the number of markers in each view, and the 3D point $\mathbf{X}_\Pi$ is in the reference frame of the source. As seen in Fig. 1.5(a), the homography $\mathbf{H}$ defines the mapping of the projection of a 3D point, $\mathbf{x}_i$, from one view to it's corresponding projection in another, $\mathbf{x}'_i$, by:

$$\mathbf{x}_i' \sim \mathbf{H}\mathbf{x}_i$$

This planar homography defines the mapping of the detector plane in one view to the detector plane in another view.

In general, the homography has 8 degrees of freedom but is dependent on 15 parameters, $\mathbf{H} \sim \mathbf{K}'(\mathbf{R} - \mathbf{t}\mathbf{n}^T/d)\mathbf{K}^{-1}$ (Eqn. (1.7)). As illustrated in Fig. 2.1, when the 3D points are expressed in the reference frame of the source (ie. attached to the source), the general homography (Eqn. (1.7)) simplifies to:

$$\mathbf{H} \sim \mathbf{K}'\mathbf{R}\mathbf{K}^{-1}$$

which is dependent only on the intrinsic calibration parameters of both views, $\mathbf{K}$ and $\mathbf{K}'$, and the relative rotation of the detector between views, $\mathbf{R}$.

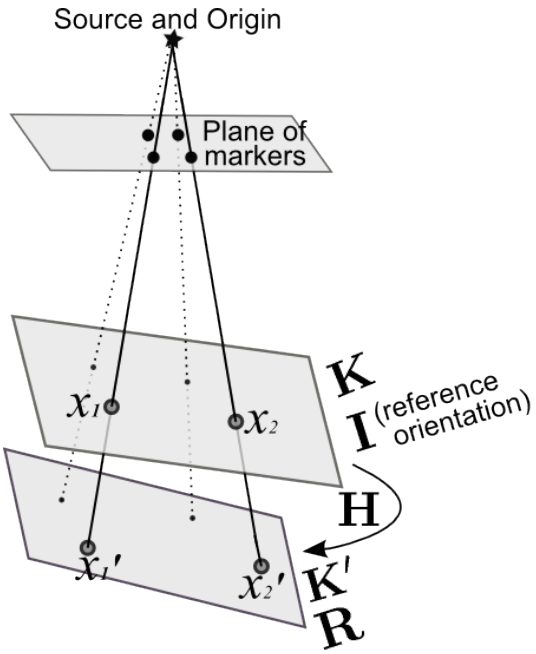

Figure 2.1: Diagram of the homography intrinsic calibration model.

The homography formulation relies only on the imaged position of the markers on the detector planes, and thus the 3D location of the markers or collimator edges does not need to be known, nor do the 3D locations need to be in any particular arrangement.The homography is established provided that the markers are visible in the projection images

and their projected locations are not co-linear, that is to say that the projection of the markers cannot produce a line on the detector plane.

The homography matrix is determined up to scale and therefore contains 8 degrees of freedom. The matrix can be identified up to scale using 8 measurements from four points or lines in both views (refer to subsection 1.2.2). If the initial IC parameters, $\mathbf{K}$, are known or have been measured in one of the two views then it follows that: $\mathbf{HK} \sim \mathbf{K'R}$ and the product $\mathbf{K'R}$ is known. With some simple algebra the IC parameters of the second view and the relative rotation of the detector can be deduced:

$$\mathbf{HK} \sim \mathbf{K'R} \tag{2.2}$$

$$\mathbf{HK}(\mathbf{HK})^{\mathbf{T}} \sim \mathbf{K'R}(\mathbf{K'R})^{\mathbf{T}}$$

$$\mathbf{HK}(\mathbf{HK})^{\mathbf{T}} \sim \mathbf{K'RR^{T}K'^{T}} \sim \mathbf{K'K'^{T}}$$

The form of $\mathbf{K'}$ is known, Eqn. 1.5, thus the form of $\mathbf{K'K'^{T}}$ is known and further because $\mathbf{K'K'^{T}}_{(3,3)} = 1$ the above relation, established up to scale, can be determined to exact equality and the values of f', u'_s, v'_s, can be easily determined from the scaled matrix $\frac{\mathbf{HK}(\mathbf{HK})^{\mathbf{T}}}{\mathbf{HK}(\mathbf{HK})^{\mathbf{T}}_{(3,3)}}$. This process is similar to QR decomposition (but RQ decomposition instead) and is explained in further detail in [Sturm 2013].

Therefore, if the homography is determined between two views and the intrinsic parameters are known in one of the two views the IC parameters of the second view, $\mathbf{K'}$, can be determined uniquely along with the rotation of the detector between views, $\mathbf{R}$. This procedure can be repeated to determine the variation of the IC parameters relative to the measured or known IC parameters $\mathbf{K_0}$ for every projection image of a scan, N, $\mathbf{K'_i}$ for $i = 1 \ldots (N-1)$. For evaluation purposes the rotation of the detector relative to the initial view is of no importance because this is only the rotation of the detector in the x-ray source/marker plane coordinate frame not the world coordinate frame which would require an additional rotation and translation. This step would be achieved by an extrinsic calibration method.

2.1.1 Homography determined using lines

A simple modification is required to obtain the homography between views using lines instead of points. In projective geometry a point $\mathbf{x}$ lies on the line $\mathbf{l}$ if and only if $\mathbf{x^{T}l} = 0$

or $\mathbf{l^T x} = 0$. Given that $\mathbf{x'} = \mathbf{Hx}$, we have:

$$\mathbf{l}'_i = \mathbf{H^{-T}} \mathbf{l}_i \quad \text{or} \quad \mathbf{l}_i = \mathbf{H^T} \mathbf{l}'_i \tag{2.3}$$

for lines $i = 1 \ldots m$.

Equivalently the intersection points of the lines can be computed to determine the homography with points.

2.1.2 Initial estimate of $\mathbf{K_0}$

The homography calibration (HC) method requires an initial estimation of the intrinsic calibration parameters for a single view of the scan. In the real world situation the initial estimate of the IC parameters can be provided by utilizing an offline calibration technique which can accurately determine the IC parameters of each view independently. This phantom can be used to fully calibrate a single initial view of the scan before data acquisition. Essentially this involves a single projection image of an offline calibration phantom to determine the initial $\mathbf{K_0}$ before removing the phantom and proceeding with the full scan of the object of which each view is intrinsically calibrated using the collimator. The offline calibration procedure of Mennessier et. al. [Mennessier *et al.* 2009] (further described in Spencer et. al. [Spencer *et al.* 2012]) would be a suitable method for this purpose.

In the case of simulation studies, the initial $\mathbf{K_0}$ could be given by either using the calibration procedure of Mennessier et. al. [Mennessier *et al.* 2009] and the simulated gold-standard phantom (refer to section 1.2.3.2, or alternatively by using the known ground-truth IC parameters from the simulation conditions from a single view.

2.1.3 Detection of spherical markers in an x-ray image

Even in ideal conditions the projection of spherical markers on an x-ray detector plane usually creates an ellipse. The center of these elliptical regions can be located easily in the image by means of a gray level center of mass weighting of the projected ellipse. Clackdoyle and Mennessier [Clackdoyle & Mennessier 2011] explained that the center of mass of the projection of this ellipse is not the projection center of the spherical marker, although the error on the 2D location estimated by the center of mass is very small and considered negligible for our purposes. Thus the projection center of our spherical markers are approximated by the center of mass of the ellipse without correction.

Software such as ImageJ [Abràmoff *et al.* 2004] can be used to automatically threshold the image, segment the locations of spherical markers, and then apply a gray level center of mass weighting to accurately determine their location in the image. This process is identical for either real or simulation data.

2.2 Results

Using the detected locations of the spherical markers of the phantoms, the gold-standard calibration was completed as in [Mennessier *et al.* 2009], and the homography calibration (HC) was completed as in the previous section using both the single view initial IC from our gold-standard, $\mathbf{K_0^{GS}}$, and from the ground-truth simulation conditions, $\mathbf{K_0^{Sim}}$.

For all simulation studies we are interested in 3 things: (1) how accurately the HC method determines the IC parameters, $\mathbf{K^H}$, compared to the ground-truth parameters, $\mathbf{K^{Sim}}$, when the HC method is initialized with the ground-truth IC parameters, $\mathbf{K_0} = \mathbf{K_0^{Sim}}$ (ie. $\mathbf{K^H}$ determined using $\mathbf{K_0^{Sim}} \equiv \mathbf{K_{Sim}^H}$), (2) how accurately the HC method determines the IC parameters, $\mathbf{K^H}$, compared to $\mathbf{K^{Sim}}$ when the HC method is initialized with the gold-standard IC parameters, $\mathbf{K_0} = \mathbf{K_0^{GS}}$ (ie. $\mathbf{K^H}$ determined using $\mathbf{K_0^{GS}} \equiv \mathbf{K_{GS}^H}$), and (3) how accurately the gold-standard estimates the IC parameters, $\mathbf{K^{GS}}$, relative to the ground-truth $\mathbf{K^{Sim}}$. The second comparison, (2), corresponds to the real data situation in which we compare the accuracy of the HC method $\mathbf{K^H}$ initialized with $\mathbf{K_0^{GS}}$ compared to our offline gold-standard calibration technique.

Although the HC method can estimate both the IC parameters and the orientation of the detector we are only interested in how well it can estimate the IC parameters as the detector orientation is not in the world coordinate reference frame and of no interest for calibration purposes.

Table 2.1: Chart of simulation evaluation comparisons.

Comparison	Calculation of mean, standard deviation, and max $\lvert \cdot \rvert$
(1)	$\mathbf{K^{Sim}} - \mathbf{K_{Sim}^H}$
(2)	$\mathbf{K^{Sim}} - \mathbf{K_{GS}^H}$
(3)	$\mathbf{K^{Sim}} - \mathbf{K^{GS}}$

From the above comparisons (Table 2.1) the differences of the IC parameters for every simulated projection image (Δf, Δu_s, and Δv_s) were found and the mean, stan-

dard deviation (SD), and maximum absolute value ($\max|\cdot|$), was calculated. These quantities show the validity, and accuracy of the intrinsic calibration method.

This simulation study will look at the performance of the HC method relative to the ground-truth and our gold-standard calibration: without noise and without C-arm deformation (ie. a perfect circular orbit), with noise and without C-arm deformation, and with noise and with deformation. The simulation program can allow the alteration of the source position, the detector position, and the detector orientation however because the planar phantom is rigidly attached to the source, any translation of the source position would be equivalent to the same translation in the detector position in the opposite direction. Therefore for all simulation studies the full range of C-arm deformation involves only the detector orientation, characterized by the Euler angles of the detector (Φ, Θ, η), and the detector position relative to the source characterized by (z_d, y_d, x_d). Refer to subsection 1.2.3.3 on page 23 for more information concerning simulated deformation.

2.2.1 Initial validation of homography calibration - noiseless simulated projection images as source and detector rotate along perfect circular trajectory

As an initial validation the homography IC was completed using the simulation ground-truth (GT) conditions. Instead of measuring the marker positions on the image the center of the spherical markers were projected on the detector plane to give the theoretical projected locations, (u_T, v_T). Using the GT initial view IC, $\mathbf{K_0^{Sim}}$, the IC was identical to the simulation GT conditions, which was expected.

Next the projected marker locations were measured from noiseless images of a 180^o, 50 projection simulated scan which had no deformation (ie. the source and detector followed a perfect circular orbit around the isocenter). When the HC was performed using the GT initial IC, $\mathbf{K_0^{Sim}}$, the IC has no measurable difference compared to the GT IC parameters indicating the high precision of the measured marker locations in the absence of noise or deformation. When comparing the measured $(u, v)_i$ (for $i = 1...4$) locations in the image with the GT projected marker locations, $(u_T, v_T)_i$, the measured locations in each projection of the scan had an average root-mean square (RMS) error of 0.021 pixels.

The gold-standard calibration was completed under the same conditions, the C-arm source and detector rotation around the gold-standard calibration phantom with a perfect circular orbit. Table 2.2(left) presents the mean, standard deviation (SD), and max

absolute value of the difference between the gold-standard, $\mathbf{K}^{\mathbf{GS}}$, and GT, $\mathbf{K}^{\mathbf{Sim}}$, of all projections of the scan. The results show that the mean difference was close to zero however even without noise and deformation of the detector position and orientation the gold-standard IC contained variations. These variations suggest inherent inaccuracies with the calibration method or potentially extreme sensitivities to the minuscule (assumed negligible) spherical center projection error discussed in subsection 2.1.3. Despite the varying intrinsic parameters of each view, with only 50 projections of the GS phantom at different orientations the intrinsic parameters can be fairly well estimated from the mean of the measured IC parameters of each view, see Table 2.2(left).

When performing the HC using the initial single view IC from the gold-standard, $\mathbf{K}_{\mathbf{0}}^{\mathbf{GS}}$, the IC displayed a static deviation shown in mean difference of the estimated IC parameters with the GT, Table 2.2(right), however the variation of the IC parameters was zero. This evaluation demonstrates that the variation of the IC between projection views can be determined perfectly from the four markers attached to the x-ray source (hence zero variation in Δf, Δu_s, and Δv_s). Further when the HC is initialized with an inaccurate single view IC, $\mathbf{K}_{\mathbf{0}}^{\mathbf{GS}}$ in this case, there is a static bias in the estimation of the IC parameters of every projection image.

Table 2.2: Comparison of the gold-standard method with the simulation ground-truth (left) and comparison of the HC initialized with $\mathbf{K}_{\mathbf{0}}^{\mathbf{GS}}$ with the simulation ground-truth (right). All simulations are without C-arm deformation or noise. (All units are pixels.)

Difference with K^{Sim}	K^{GS} Δf	K^{GS} Δu_s	K^{GS} Δv_s	K^{H}_{GS} Δf	K^{H}_{GS} Δu_s	K^{H}_{GS} Δv_s
mean	0.4	-0.6	0.8	13.1	-14.5	-2.6
SD	3.6	3.4	3.3	0.0	0.0	0.0
max $\lvert \cdot \rvert$	11.2	8.3	9.2	13.1	14.5	2.6

2.2.2 Evaluation with noise but without C-arm deformation

Similar to the above, 50 projection images of the phantoms with noise as the source and detector rotate along a perfect circular orbit were generated in order to see the effects on the calibration methods due to image noise only. (For details about the measured C-arm image noise refer to subsection 1.2.1.3 on page 13). The HC method initialized with the simulation ground-truth, $\mathbf{K}_{\mathbf{Sim}}^{\mathbf{H}}$, shows the error due to noise is on the order of 1 pixel with a maximum error in the 50 projection scan of 4 pixels, see Table 2.3(left).

The measured marker locations in the presence of noise, compared to the GT projected locations had an average RMS error of 0.025 pixels (compared to 0.021 pixels without noise).

This result demonstrates the approximate error on the IC. Under normal conditions (with noise) the HC can not expect to achieve better results than: $\sigma_f = \pm 0.1$ pixels, $\sigma_{u_s} = \pm 1.1$ pixels, and $\sigma_{v_s} = \pm 1.1$ pixels.

The gold-standard method compared to the simulation ground-truth showed an increase in error due to noise from approximately 3 to 4 pixels (the error without noise) to 5 to 7 pixel error due to both the noise and the calibration method, Table 2.3(right).

Table 2.3: Comparison with the simulation ground-truth of the HC initialized with $\mathbf{K_0^{Sim}}$ (left), and the gold-standard method (right). All simulations are without deformation but with noise. (All units are pixels.)

Difference with K^{Sim}	K^H_{Sim} Δf	K^H_{Sim} Δu_s	K^H_{Sim} Δv_s	K^{GS} Δf	K^{GS} Δu_s	K^{GS} Δv_s
mean	0.0	-1.7	-1.5	-0.8	0.1	0.2
SD	0.1	1.1	1.1	7.2	5.0	5.6
max $\lvert \cdot \rvert$	0.2	4.2	4.0	22.3	14.4	12.2

Similar to the above results without noise, when the HC method was initialized with the gold-standard, $\mathbf{K_0^{GS}}$, there was a systematic error seen in the mean while the standard deviation was exactly the same as the result when initialized with $\mathbf{K_0^{Sim}}$. This result shows that when the HC is initialized with IC parameters that are close to but not exactly correct there is little to no affect on the HCs accuracy in determining the variation of the intrinsic calibration parameters, hence zero standard deviation, there is only a systematic error on all the IC parameters equivalent to the error of the initial $\mathbf{K_0}$.

2.2.3 Evaluation with noise and C-arm deformation

Simulation evaluations with simulated C-arm deformation and added noise resemble the real world operating conditions of the C-arm imaging system. Fifty projection images over 180^o were simulated with a randomly generated detector position and orientation (variation of six parameters). The simulated random deformation was intended to depict the maximum feasible level of deformation of any standard C-arm system. (For a specific description of the simulated random deformation refer to subsection 1.2.3.3 on page 23.)

The HC was completed with both the initial single view IC of the GT conditions, $\mathbf{K^H_{Sim}}$, and the gold-standard, $\mathbf{K^H_{GS}}$, as shown in Table 2.4. These can be compared with the IC parameters of the gold-standard calibration, $\mathbf{K^{GS}}$, Table 2.4(right). The average RMS error of the imaged $(u, v)_i$ locations was found to be 0.027 pixels.

Table 2.4: Comparison with noise and C-arm deformation of the IC error of the homography calibration with the ground-truth single view IC (left), the HC with gold-standard single view intrinsic calibration (center), and the gold-standard full offline calibration method (right). (All units are pixels.)

Difference with K^{Sim}	K^H_{Sim} Δf	K^H_{Sim} Δu_s	K^H_{Sim} Δv_s	K^H_{GS} Δf	K^H_{GS} Δu_s	K^H_{GS} Δv_s	K^{GS} Δf	K^{GS} Δu_s	K^{GS} Δv_s
mean	0.0	-0.9	-0.7	-1.6	-4.3	-2.4	-0.3	-0.0	-0.4
SD	0.1	1.1	1.0	0.3	1.1	1.0	6.7	5.2	5.8
max $\lvert\cdot\rvert$	0.3	3.4	2.7	2.1	6.9	4.5	22.0	13.8	20.3

The comparison of the homography IC with the full gold-standard calibration show that the variation in the IC parameters is more accurately estimated with the HC method. However if the initial view IC contains error, this error is transfered to all the IC parameters leading to a static bias (displayed in the mean difference of the IC parameters). Additionally when comparing the HC using the GT single view IC, $\mathbf{K^H_{Sim}}$, with and without deformation (Table 2.4 and Table 2.3) reveals that the SD of the IC parameters are similar thus the calibration is insensitive to C-arm deformation and primarily noise affects the HC accuracy.

2.2.4 Single and multiple deformation parameter variation

A secondary evaluation of the HC performance during C-arm deformation was completed. First each of the six deformation parameters, (z_d, y_d, x_d, Φ, Θ, η), was varied individually by a random amount presumed to be the max feasible C-arm deformation(subsection 1.2.3.3). Secondly, two parameters were simultaneously varied by a random amount to see the error interdependence due to multiple parameter variation.

As shown in the previous section, when using spherical markers attached to the source the HC inaccuracies are primarily the result of noise, with the error due to noise approximately 5 to 10 times greater than the error due to simulated deformation. As a result, the effects from single and multiple parameter deformation can not be observed in the presence of noise and the evaluations were achieved without added image noise.

The error on the $\mathbf{K}^{\mathbf{H}}_{\mathbf{Sim}}$ IC parameter estimation, σ_f, σ_{u_s}, σ_{v_s}, resulting from the individual random variation of the z_d, y_d, x_d, Φ, Θ, and η can be seen in Table 2.5.

Table 2.5: The intrinsic calibration estimation error resulting from the random deformation of $(z_d, y_d, x_d, \Phi, \Theta, \eta)$ individually, in the absence of noise. Note the dash signifies 0.0 pixel error. (All units are pixels.)

Deformation Parameter	z_d	y_d	x_d	Φ	Θ	η
σ_f	-	-	-	-	-	-
σ_{u_s}	-	0.1	-	-	0.2	-
σ_{v_s}	-	-	0.1	0.3	-	-

Table 2.6 presents the error on the $\mathbf{K}^{\mathbf{H}}_{\mathbf{Sim}}$ IC parameter estimation, σ_f, σ_{u_s}, σ_{v_s}, resulting from the variation of: (z_d, x_d), (z_d, Φ), (z_d, η), (x_d, Θ), (x_d, Φ), (x_d, η), (Θ, Φ). In this study we can assume that the error due to deformation of y_d would be the same or similar to x_d, while Θ and Φ would produce a similar effect, and further the combination of (x_d, Φ) would be the same as (y_d, Θ).

Table 2.6: The intrinsic calibration estimation error resulting when two deformation parameters vary simultaneously in the absence of noise. Note the dash signifies 0.0 pixel error. (All units are pixels.)

Deformation Parameters	(z_d, x_d)	(z_d, Φ)	(z_d, η)	(x_d, Θ)	(x_d, Φ)	(x_d, η)	(Θ, Φ)
σ_f	-	-	-	-	-	-	-
σ_{u_s}	-	-	-	0.2	-	0.1	0.2
σ_{v_s}	0.2	0.2	-	0.1	0.3	0.1	0.2

The results validate that the error due to C-arm deformation is much less than the error due to projection image noise, and additionally the deformation due to multiple parameter variation is usually a simple quadratic additive increase of the errors due to individual deformation.

2.3 Discussion

The simulated projection of spherical markers can be very accurately localized in 2D images. As a result, simulation studies utilizing spherical markers provide a valuable

initial investigation of the HC method. This study showed that by using only the imaged position of four spherical markers attached to the source, with unknown 3D location, the homography calibration method can precisely determine the change or variation of the IC parameters between two or more projection views from a C-arm x-ray imaging system.

The most noteworthy observation from this investigation is that if there is any error in the initial single view IC it is transfered, as a static bias, to the estimated IC parameters of every projection of the scan. Daly et al. [Daly *et al.* 2008] studied the effect on the reconstruction image quality when there is a static bias in the focal length and orthogonal projection of the source on the detector (u_s, v_s). They showed that although a static error in the focal length has little effect on the reconstruction image quality the (u_s, v_s) parameters are crucial and a static error would produce a significant loss in image quality. More specifically they revealed that a reduction in image quality could be observed with as little as a 1 pixel static bias though the effects were small.

We have proposed to use a single projection of the gold-standard phantom to provide the initial view IC before measuring the variation of the IC between this view and all others of the scan. Our results have demonstrated that the gold-standard calibration method contains a significant amount of variation (on the order of 5 pixels) in the IC parameters between views of a scan. Therefore this indicates that simply using a single projection from the gold-standard calibration is not a practical means of obtaining an accurate initial view IC.

We present here a significantly more feasible approach to obtaining the initial view IC using the gold-standard calibration phantom. The gold-standard phantom can be placed in the isocenter of the C-arm and rotated, manually or on a turntable, 360^o while the C-arm remains in a constant static position. The static C-arm should have static IC parameters and a static image of the collimator in the FOV. Obtaining several projection images of the rotating phantom produces projection images with changing extrinsic calibration parameters but static intrinsic. Although the gold-standard calibration may show varying IC parameters, the average of the gold-standard calculated IC parameters during several projections around 360^o would provide an accurate IC. This hypothesis has been validated with simulation studies and further demonstrated in Table 2.4 in which the mean IC error (the difference from the ground-truth IC) is less than 0.5 pixels. The image of the collimator and the initial (rotating gold-standard) IC can be saved and afterwards the IC variation can be determined between all views of a scan and the reference image of the collimator with the accurately measured single view IC.

We have demonstrated that when our IC method is accomplished with an accurate

initial view IC it provides a better estimate of the IC compared to the gold-standard calibration, however this comparison does not imply that a reconstructed image with our IC would be an improvement compared to a gold-standard reconstructed image. The gold-standard determines all nine calibration parameters which specify the projection from the source to the detector through the 3D world coordinate frame. Though we have shown the IC parameters vary by several pixels in a simulated scan there may also be variation in the extrinsic parameters which gives a good estimation of the lines through 3D space from the source to the detector. Therefore as long as these lines are well estimated, the reconstruction image quality would still be suitable. Chapter 4 will attempt to evaluate the reconstructed image quality of our method and the gold-standard full offline calibration method.

After understanding the affects on the HC of the initial view IC and supposing that when in real data conditions a good estimate of the initial view IC should be achievable, for all future simulation studies we will assume the initial view IC is accurately known (or rather given by the ground-truth simulation conditions). Consequently, this aspect will be removed from future investigations.

Chapter 3

Collimator Edge Detection via the Radon Transform for Homography Intrinsic Calibration

---

Résumé du Chapitre 3 en Français

Nous décrivons la détection de bords du collimateur, ou de droites "épaisses", dans les projections radiographiques et nous en donnons un état de l'art. La transformée de Radon est proposée comme une méthode de détection de droites dans [Zhang & Couloigner 2007, Copeland *et al.* 1995, Götz & Druckmüller 1995, Rey *et al.* 1990]. Plusieurs méthodes de détection de bords de collimateurs à base de transformée de Radon sont proposées et évaluées sur des images simulées. Nous évaluons la précision de la détermination des droites mais aussi celle de l'estimation des paramètres de calibration intrinsèque. Nos méthodes sont comparées à des méthodes standard comme le filtre de Canny. À partir de ces simulations, la meilleure méthode de détection de la projection du bord d'un collimateur est déterminée. Nous avons remarqué que les discrétisations des images (taille des pixels) est une limitation majeure, en pratique, de nos méthodes. Les méthodes que nous proposons permettent d'améliorer la précision de l'estimation de l'angle d'une droite par rapport aux méthodes standard (filtre de Canny) qui ne permettent pas de déterminer cet angle avec suffisamment de précision (pour l'obtention de paramètres de calibrations intrinsèques en vue d'une reconstruction 3D).

Nous avons appliqué notre méthode sur des données réelles acquises sur un C-arm. Nous l'avons comparé à des méthodes standard comme le filtre de Canny et nous avons montré que notre méthode est plus stable et précise.

Summary

This chapter describes the implemented technique of collimator edge detection in an x-ray projection image and presents both simulation and real data evaluations.

3.1 Introduction to Line or Edge Detection

The method implemented to detect the collimator edges in a projection image must be designed to be robust and accurate with the ability to detect the collimator edges both in simulation images and real data. Calibration is very sensitive to errors in the detected positions of the markers/lines thus the line detection must be as accurate as possible. There are several well known techniques for line detection in the literature. For our purposes a method which very accurately detects thick, straight lines in noisy images must be developed.

Standard edge detection is composed of two steps, the detection of edges in an image and arranging or linking of these edges into global edge or line structure in the image [Burns & Hanson 1986, Copeland *et al.* 1995]. Commonly edge detection in an image is performed by the application of an edge detection filter of small spatial extent relative to the lines/edges in the image. The most common edge detectors implemented to perform this step would be (but are not limited to): the Sorbel edge detector, a simple 2D gradient or Laplace operator, and frequently the Canny edge detector [Canny 1986]. The Canny edge detector uses the derivative of a 2D Gaussian filter to obtain the gradient of the image. The edges in the image gradient become maxima. The edge pixels are identified and linked using a hysteresis thresholding which combines weak edge pixels with strong edge pixels to produce the global edge structure in a binary image. The Canny edge detector was further adapted by Deriche [Deriche 1987] to improve the filters capability in the presence of noise.

Once these edge pixels have been located in the image the next step requires a process of removing any false, unimportant or redundant edge pixels, and arranging or linking the remaining edge pixels into well defined edges or lines in the image. There are a variety of different techniques to do this (see [Burns & Hanson 1986] for an overview), however by far the most commonly used technique is the Hough transform [Duda & Hart 1972]. The Hough transform simply involves the conversion of a binary 2D image from Cartesian coordinates to a 2D histogram in polar coordinates. Thus lines in Cartesian space become points in (s, θ) space via the Hough transform. Measuring the maxima(s) (or minima(s)) in this 2D histogram yields the (s, θ) parameters of the line(s)

in the original image.

There are many problems with edge detection by these means. Firstly the intensity variation depicting an edge or line is most often distributed over an extended area and this variation may be very irregular and difficult to characterize. As a results these techniques often do not define thick lines properly, possibly producing multiple parallel edge responses along the profile of a single edge. Next, due to the small spatial extent of the operator, edge detectors often enhance the noise in the image causing inaccurate line/edge estimation. Aliasing due to the discretization of the image can also cause errors in edge/line detection by these methods.

In our case a method to precisely detect the thick, straight edges of the x-ray tube collimator in the image field of view possibly in the presence of significant noise is required. Straight line detection can simply and fairly accurately be accomplished by implementation of the Canny edge detector and Hough transform which is also suitable for detection of lines with curvature. However, due to the limitations mentioned above this technique is presumably not optimal for determination of thick edges or edges in the presence of significant noise. Burns & Hanson have developed an alternate method of straight line detection with the consideration of thick lines although the accuracy of their method is inadequate [Burns & Hanson 1986].

The Radon transform has been shown to be useful for straight line detection in numerous instances [Zhang & Couloigner 2007, Copeland *et al.* 1995, Götz & Druckmüller 1995, Rey *et al.* 1990]. Instead of the process of first detecting edges locally and then linking them to find the global edge structure, the Radon transform can directly detect the linear features in an image [Copeland *et al.* 1995]. The Radon transform is similar to the Hough transform [Duda & Hart 1972] or rather that the Hough transform is a special case of the Radon transform [Deans 1981]. Due to the inherent operation (ie. integration) of the Radon transform, it has been shown to be resilient in the presence of noise [Murphy 1986]. Further the detection of lines with the Radon transform can be improved by applying a filter directly in the transform domain [Rey *et al.* 1990, Murphy 1986]. Drawbacks of the Radon transform include its inability to determine the length or end points of a line segment in an image [Murphy 1986, Burns & Hanson 1986], and its difficulty in detecting lines with slight curvature [Murphy 1986, Burns & Hanson 1986] or line segments with lengths which are significantly less than the image dimensions [Copeland *et al.* 1995].

The Radon transform is suited for detection of straight lines, of any thickness, which are close to or exceed the dimensions of the image and possibly in the presence of significant noise [Copeland *et al.* 1995, Zhang & Couloigner 2007]. Given that the

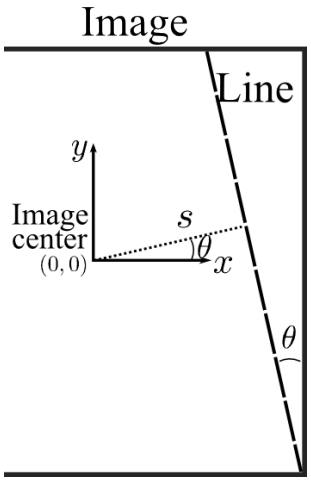

Figure 3.1: Characterization of a line in the image by the parameters (θ, s).

information of the length, width, or end points of the edges does not need to be measured the Radon transform should be an effective technique for the detection of the edges of the x-ray tube collimator in the image.

3.1.1 Line determination using the Radon transform

Unlike the center of mass weighting of spherical markers, line detection relies on the extraction of the two parameters which describe the line in the image, the angle $\theta\varepsilon[0, 2\pi)$, and position of the line defined as the shortest signed distance from the origin to the line, s (with $s\varepsilon\mathbb{R}$), see Fig. 3.1. Accordingly the line is described by the equation:

$$x\cos\theta + y\sin\theta = s \tag{3.1}$$

with:

$$vx + uy + 1 = 0$$

where $u = -\sin\theta/s$ and $v = -\cos\theta/s$ as described in subsection 1.2.2.

When the collimator is slightly closed and an x-ray projection image is acquired the edge (or line) of the collimator is observed as a gradual increase or decrease in intensity from the maximum intensity to zero, or vise versa. This gradual change is the result of the x-ray imaging properties and the design of the x-ray tube and collimator. The resulting imaged edge is quite unlike edges imaged in standard computer vision.

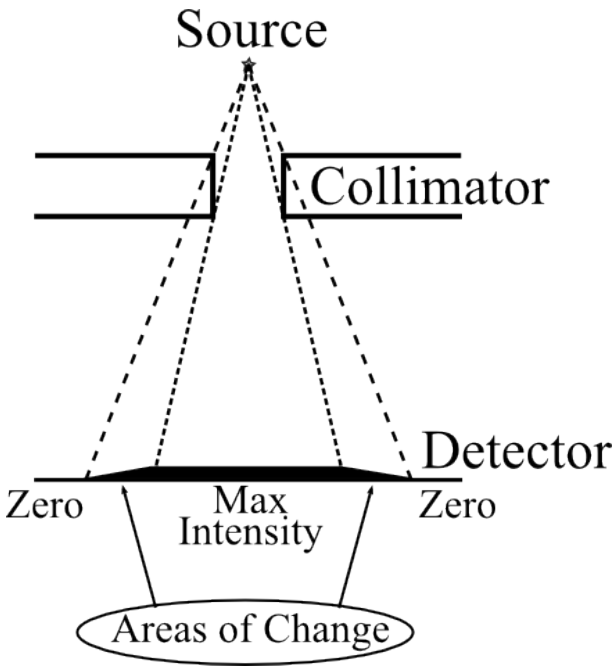

Figure 3.2: Diagram of the x-ray projection of the collimator edge (2D).

X-rays have the ability to penetrate matter and the resulting measured intensity on the detector is related to the amount and density of matter which the x-ray beam has traversed, see Fig. 3.2. When the x-ray beam does not traverse matter it is unhindered and the total flux of x-rays emitted reaches the detector resulting in maximum intensity at that location. Alternatively when the x-ray beam passes through the full width of the collimator, all the photons are blocked and the detector should (in ideal conditions) measure zero photons and zero intensity. In between these two regions the x-ray beam partially passes through the collimator and only some of the photons are stopped while others pass. It follows that a gradual change in the intensity from zero to the maximum is measured in the image extending perpendicularly from the edge. This change defines the edge of the collimator and can be characterized in several different ways which will be explained in more detail below.

The intensity profile along this edge follows an exponential curve when in ideal noiseless conditions using a monoenergetic x-ray beam (for more details refer to subsection 1.2.1.2 page 12). Under normal conditions this edge profile would deviate from an exponential curve. The profile of an edge as imaged in computer vision has been described by Burns & Hanson [Burns & Hanson 1986] as being highly non-linear, with wide low contrast shoulders, and distributed over an extended area. Though our edges

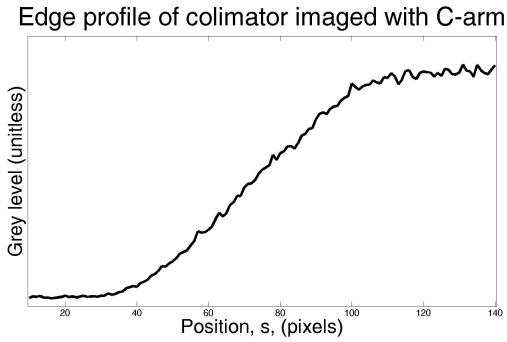

Figure 3.3: The collimator edge profile from **a real x-ray C-arm image**. Note that the edge profile of the real image is not perpendicular to the actual edge angle unlike the profiles shown in Fig.3.4.

are generated by a completely different means, an edge imaged using a polyenergetic x-ray beam by an imperfect detector in non-ideal imaging conditions similarly produces a non-linear edge profile with wide low contrast shoulders at the beginning and end of the edge profile, Fig 3.3.

The simulation program does not model the image directly but instead models the negative ln of the gain correct image (for a monoenergetic beam) which is what is required for image reconstruction (refer to section 1.2.3 on page 21). Therefore edges generated by the simulation program in the absence of noise generate a linear edge profile as seen in Fig. 3.4a and Fig. 3.4b, with the addition of Gaussian noise. It should be possible to detect the linear edge profile generated by the simulation program, the real x-ray C-arm edge profile, Fig. 3.3, or the negative ln of the gain corrected real image, all with the same line detection method.

In order to detect the collimator edge in the image the Radon transform has been proposed as a method which can accurately characterize this gradual change in intensity. The continuous form of the Radon transform of a 2D image, $f(x, y)$, is given by:

$$F(\theta, s) = \iint_I f(x, y)\delta(s - x\cos\theta - y\sin\theta)\,\mathrm{d}x\,\mathrm{d}y$$

where s and θ are shown in Fig. 3.1, I is the entire $x - y$ image plane, and δ is the Dirac delta distribution where: if f is a smooth function, $\int f(x)\delta(x) = f(0)$. This Dirac delta distribution forces the integration of the image over a single line with equation $s = x\cos\theta + y\sin\theta$. Thus the Radon transform of an image at a specific angle θ is the 1D projection of the image intensity (as a function of s) along that angle. In practice the image is discrete and not continuous and the discrete Radon transform, which is

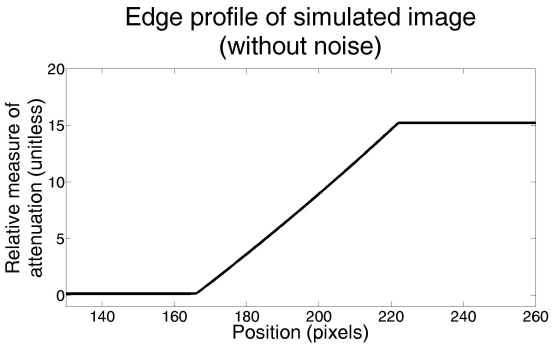

(a) Simulated edge profile without noise

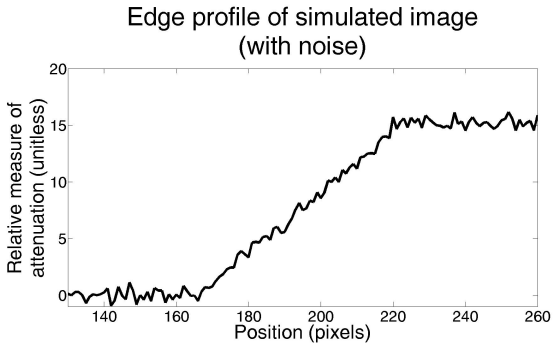

(b) Simulated edge profile with noise

Figure 3.4: Examples of the edge profiles **from simulation** studies (a) without noise, and (b) with noise. Note that the edge profile is obtained perpendicularly to the edge. The $y - axis$ shows the simulated values of the negative ln of the intensity in a gain corrected image.

described in [Götz & Druckmüller 1995, Toft 1996, Beylkin 1987], is applied to the image. As an example, the Radon transform of an image at the angle $\theta = 0^o$ gives the 1D function of the projection of the image intensity along the pixel columns of the image, is shown in Fig. 3.5(a), and similarly the Radon transform of an image at the angle $\theta = 45^o$ is shown in Fig. 3.5(b). Taking the discrete Radon transform of an image with dimensions (u_{size}, v_{size}) for $0^o \leq \theta < 180^o$ and $-\frac{1}{2}\sqrt{u_{size}^2 + v_{size}^2} \leq s \leq \frac{1}{2}\sqrt{u_{size}^2 + v_{size}^2}$ is equivalent to integrating over all possible lines in the image space. Any line in the image (of sufficient length) would be seen as a peak (for a high intensity line on low intensity background) or trough (low intensity line on higher intensity background) in the Radon transform. The amplitude of the peak or trough relative to the background in the transform is dependent on the lines intensity relative to the background intensity and also on the line length. As the Radon transform integrates over the entire image if the line does not span the image dimensions then upon integration along this line the background along with the line will contribute to the sum hence causing a reduced signal to noise ratio for short lines. Therefore for good detection, the length of the line should be close to or exceeding the image dimensions [Copeland *et al.* 1995].

For our purposes the Radon transform is used to detect the edges of the x-ray tube collimator to obtain the (θ, s) parameters required for calibration. The location, length, and width of these edges are approximately known beforehand. An example of the 1D Radon transform of an image of the edges of the collimator at $\theta = 0^o$ can be seen in Fig. 3.6(a). In the ideal case of a 1 pixel wide line, or an edge which increases from zero

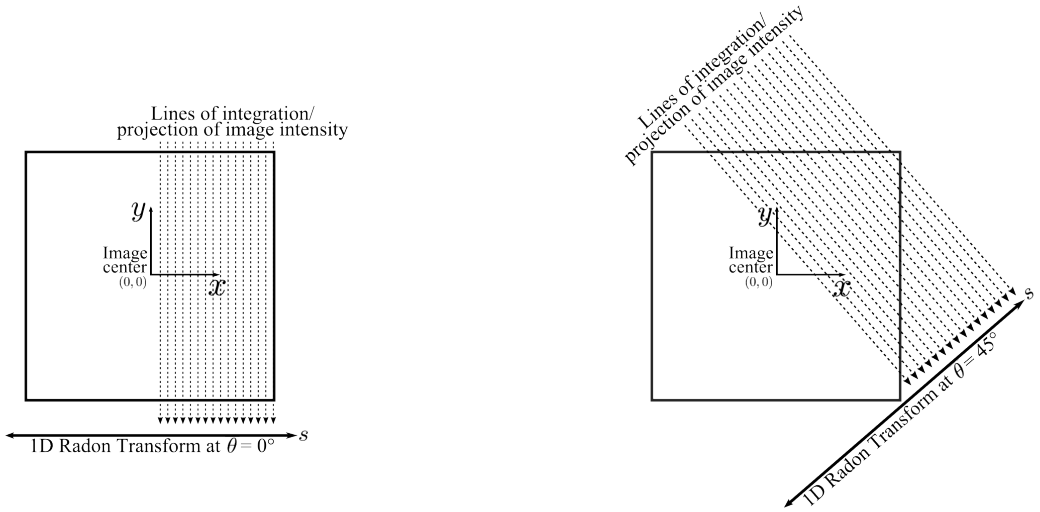

(a) Example of the Radon transform at $\theta = 0^o$ (b) Example of the Radon transform at $\theta = 45^o$

Figure 3.5: Example of the Radon transform of an image at two different angles.

along one row or column to the maximum intensity in the next row or column, the edge or line position would be defined by the abrupt discontinuity in the Radon transform, a step function at the appropriate angle and position of the line. In our case the collimator edge is thick and thus the abrupt discontinuity in the Radon transform is not seen.

For the simulated edge profile of Fig. 3.4(b) of an edge at angle $\varphi = 0^o$ and with the addition of noise, when the Radon transform is obtained at the angle of the edge, $\theta = \varphi$, the 1D Radon transform (RT) profile would look the same as the original profile (Fig. 3.7(a). However if the RT is obtained when $\theta \neq \varphi$ then the 1D RT has an exponential form with smooth shoulders and a reduced slope between the start and end positions of the edge, Fig.3.7(b). The RT of a collimator edge as imaged with an x-ray C-arm device will display the profile shown in Fig. 3.8, which is visually similar to the Radon transform of simulated data when $\theta \neq \varphi$ seen in Fig. 3.7(b).

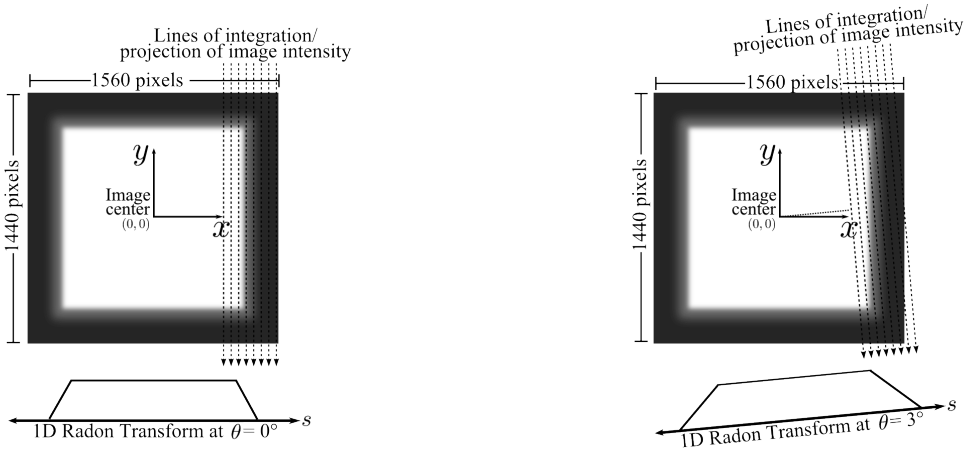

(a) Example of the Radon transform at $\theta = 0^o$ (b) Example of the Radon transform at $\theta = 3^o$

Figure 3.6: Example of the Radon transform of an edge at two different angles.

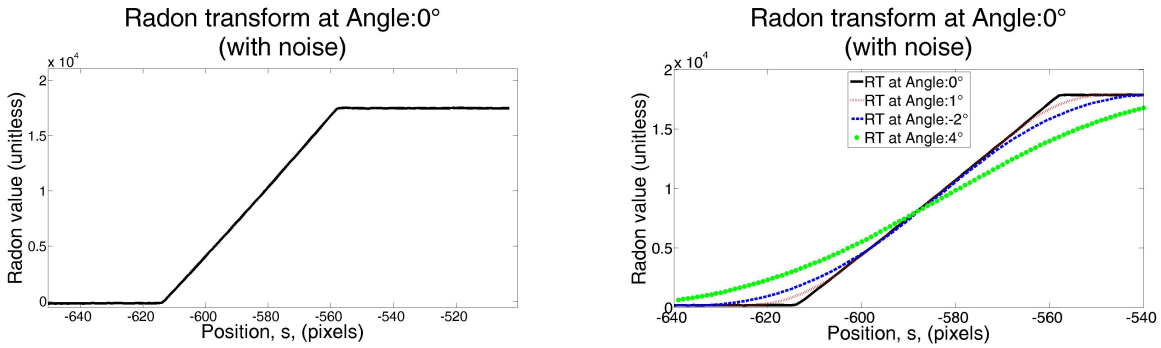

(a) Example of the Radon transform at $\varphi = 0^o$ (b) Example of the Radon transform at various angles

Figure 3.7: Profile of the 1D Radon transform of a simulated edge (with noise) located at $\varphi = 0^o$ and obtained at various Radon transform angles.

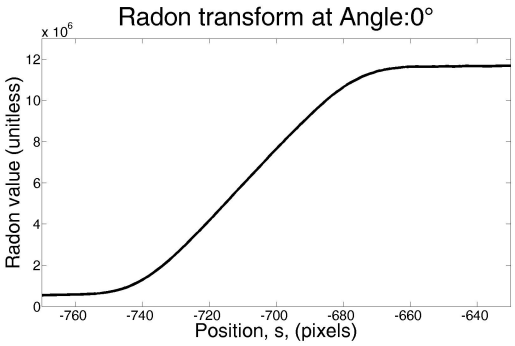

Figure 3.8: Radon transform of the collimator edge imaged with x-ray C-arm. An example of the edge profile before taking the Radon transform can be seen in Fig. 3.3. Note the Radon transform angle, $\theta = 0^o$, is likely not at the same angle of the edge, $\theta \neq \varphi$.

3.1.1.1 Characterizing the edge profile after application of the Radon transform

In order to characterize the 1D RT of the edge as a function of RT angle it can be informative to look at the first and second derivative of the simulated edge profile without noise (Fig. 3.4(a)) displayed in Fig. 3.9(a) and Fig. 3.9(b) respectively. These plots and their original profile (Fig. 3.4(a)) indicate that the angle and position (θ, s) which define the edge can be ascertained by a few specific characteristics. Most notably the 1D RT in which the change in intensity from zero to the max (or vise versa) is the most rapid, hence the slope of the line of the edge profile is maximum, can indicate that the angle of the Radon transform is the same as the angle of the edge in the image. (To clarify this point, notice the difference in the slope of the curves of the 1D Radon transforms taken at various angles, 3.7(b), of an edge at $\varphi = 0°$ in the image.) Secondly, it was observed that the maximum of the derivative of the 1D RT as a function of position increases as the angle of the RT approaches the angle of the edge (a similar result to the above condition but not identical). Lastly the smooth shoulders seen in the 1D RT become more like an abrupt change, and the least like a smooth transition from zero to the linear part of the profile. As a result of this when θ approaches φ the linear part of the profile contains the most points.

All of these conditions are similar however they can be measured in different ways. The first condition can be measured by fitting a line to the linear part of the profile and measuring the slope. The second condition is measured simply by the max of the 1D RT after a derivative filter has been applied, ie. the max of the curve in Fig. 3.9(a). And

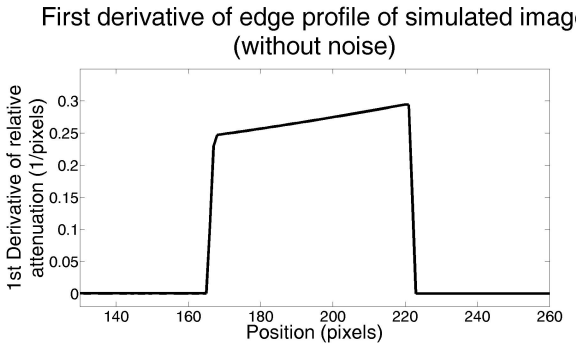

(a) First derivative of a simulated edge profile

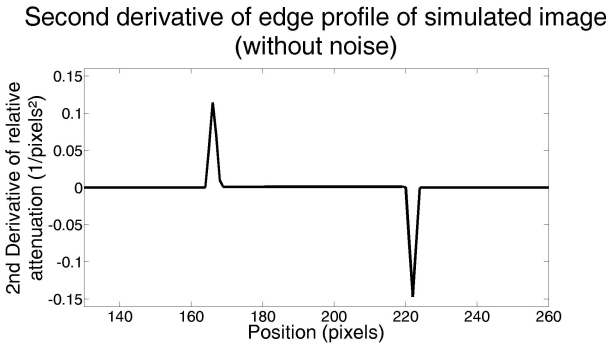

(b) Second derivative of a simulated edge profile

Figure 3.9: The first and second derivative of the profile plot of a simulated edge without noise (seen in Fig. 3.4(a)). Note that in the second derivative of the edge profile the value of the 2nd derivative between the two peaks is slightly more than zero due to the non-zero slope at the peak of the first derivative of the edge profile.

the third can be evaluated by taking the 2nd derivative of the 1D RT and measuring its max and min values, which are the max and min values seen in Fig. 3.9(b). This entails finding the max and min concavity of the curve, which is the amount of curvature seen in the shoulder regions.

The measured s position of the thick edge, which is the shortest signed distance between the edge and the center of the image, must be defined somewhere within the edge. Where exactly it is defined can be arbitrarily chosen however the location must be consistent for all edges such that the line defined in each projection corresponds to the same 3D virtual line in space. Some possible locations s could be defined would be the mid-point of the curve, or mid-point of the linear part of the curve, or the position of the maximum of the derivative of the curve.

3.1.1.2 Sensitivity of the measurement of (θ, s)

Given that the image is constructed by discrete pixels of finite size there are inherent limitations to the angular and positional sensitivity that can be achieved. The angular sensitivity can be first illustrated by assuming the ideal case of a line at $\varphi = 0^o$ which spans the image along the $y-$axis, or simply a single column of higher intensity pixels. The 1D transform at $\theta = 0^o$ would simply show a step change in intensity at the appropriate s. In this case, a line in the image at $\varphi = 0^o$ would be identical to a line at $\varphi_s = \pm \arctan(\text{line width/line height}) = \pm \arctan(1 \text{ pixel}/1440 \text{ pixel})$ and the Radon

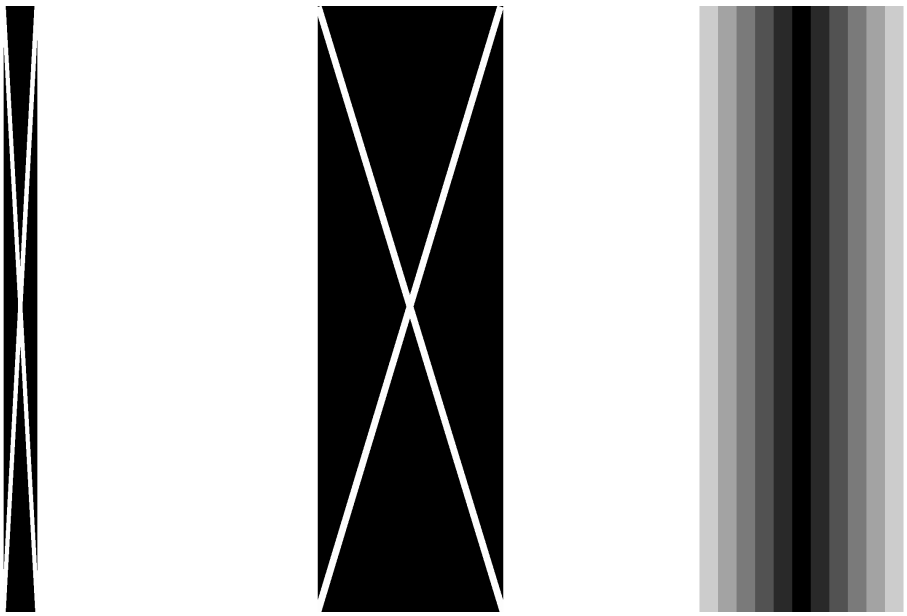

(a) One pixel wide line has angular sensitivity $\pm 0.040^o$

(b) Eleven pixel wide line has angular sensitivity $\pm 0.438^o$

(c) Eleven pixel gradient has angular sensitivity $\pm 0.040^o$

Figure 3.10: Diagram of the sensitivity of line angle measurement. The white lines indicate the maximum and minimum Radon transform angles which generate the same 1D Radon transform.

transform for $-0.040^o \leq \theta \leq 0.040^o$ produces the same result (see Fig. 3.10(a)). Now consider the case of the same line except 11 pixels wide all with the same intensity. Now the sensitivity is reduced to $\varphi_s = \pm \arctan(11/1440) = \pm 0.438^o$ (Fig. 3.10(b)). If however, the line in the image increases gradually to the max intensity in pixel column 6, and then decreases to the background intensity in pixel columns 7 to 11, then the 1D transform measures a curve and the sensitivity is again $\pm 0.040^o$ (Fig. 3.10(c)). Finally now assume the above 11 pixel wide line is orientated at $\varphi \neq 0^o$. In this case the line lies diagonally across the 2D pixel grid and each pixel intensity is determined based on its distance from the center of the line. When the discrete Radon transform is obtained at $\theta = \varphi \neq 0^o$ the resulting 1D Radon transform shows the same characteristic profile as in the above Fig. 3.10(c). However, due to the spread in pixel values close to the line, now if the discrete Radon transform is measured at $\theta = \varphi \pm \lambda \cdot 0.040^o$ (where the scalar λ is between 0 and 1) the result is not the same as the discrete Radon transform measured at $\theta = \varphi$. Hence the sensitivity is increased for lines which do not lie parallel to the image rows or columns.

To obtain the highest possible degree of angular sensitivity, despite the angle of the edge or line in the image, the angle at which the Radon transform is performed can simply be oversampled. This consists of measuring the 1D RT at a very fine angular increment. If the angular step is fine enough then undoubtedly redundant measurements of the data are being obtained, thus essentially the same 1D profile is measured. The measurement of the edge angle can be obtained at the highest degree of accuracy with the average measurement of these redundant data (ie. the angle of the midpoint in the angular sensitivity range). This is further described in section 3.2.2. The angular sensitivity depends on the discretization of the image and its pixel size but also related to the edge angle in the image.

On the other hand, the positional sensitivity is related to the method of operation of the Matlab Radon transform [Matlab 2014]. The Matlab Radon transform divides each image pixel into 4 equal sub-pixels and then projects each sub-pixel of the image along the transform angle θ, to construct the 1D Radon transform array of which each element, s, is the same width of the pixel. This indicates that the position of the line/edge can only be determined to the nearest pixel an hence the highest possible positional accuracy is ± 0.5 pixels.

3.2 Implementation of method of line detection

The following describes the development of a method of thick, straight line detection in noisy images using the Radon transform. Real data was first used to give an indication of the necessary conditions and challenges which must be satisfied in order for line detection in the case of noisy real data. Using these initial investigations our simulation program was adapted to allow the simulation of parallelepiped objects attached to the x-ray source which very closely model the real data case (described in subsection 1.2.3.2 on page 22). The real and simulation generated images of the collimator are 1560×1440 pixels image size, pixel size of 0.182 mm^2, with maximum intensity at the center and lower (or zero) intensity at the edges of the image where the x-rays are attenuated by the collimator. An example of simulated projection images of the collimator can be seen in Fig. 3.11. The following line detection methods were performed with a Matlab program which uses the Radon transform from the image processing toolbox [Matlab 2014].

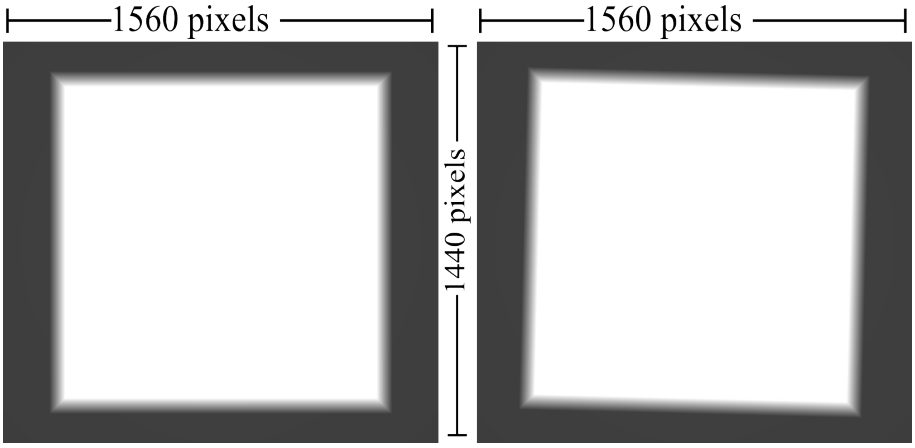

Figure 3.11: An example of a simulation generated image of the collimator without and with C-arm deformation.

3.2.1 Principle of measurements of (θ, s)

For simplicity the data, or projection image, is related to the sign convention of ImageJ, see Fig 3.12. The image of size 1560×1440 pixels is first read in by Matlab and then transposed back to the correct ImageJ orientation. The application of the Radon transform must be done in a coordinate system relative to the center of the image, see Fig. 3.12, in which the Radon transform $y - axis$ is flipped relative to the ImageJ $y_j - axis$. As a result, before the calibration step and after the determination of the parameters of the edge (θ, s), there must be a change of coordinate system in which the $y - axis$, or $u - axis$, is flipped, and the image coordinates translated by $(\frac{v_{size}}{2}, \frac{u_{size}}{2})$ back to ImageJ coordinates. The new equations for the line parameters u, and v, in Eqn. (3.1) become $u_c = +\sin\theta/s$ and $v_c = -\cos\theta/s$ when relative to the center of the image, and

$$u_j = \frac{u_c}{(1 - u_c\frac{u_{size}}{2} - v_c\frac{v_{size}}{2})} \qquad v_j = \frac{v_c}{(1 - u_c\frac{u_{size}}{2} - v_c\frac{v_{size}}{2})} \tag{3.2}$$

in ImageJ coordinates.

Being as the edges in the image do not completely span the field of view (FOV), a bias in the measurement of the angle of the edge will result if the edge positions are not approximately centered around the image center. This can result due to C-arm deformation such as the movement of the detector position relative to the source. To correct this bias before measurement, the center of mass of the image is measured and then the image size is extended to center the original image in this larger image by

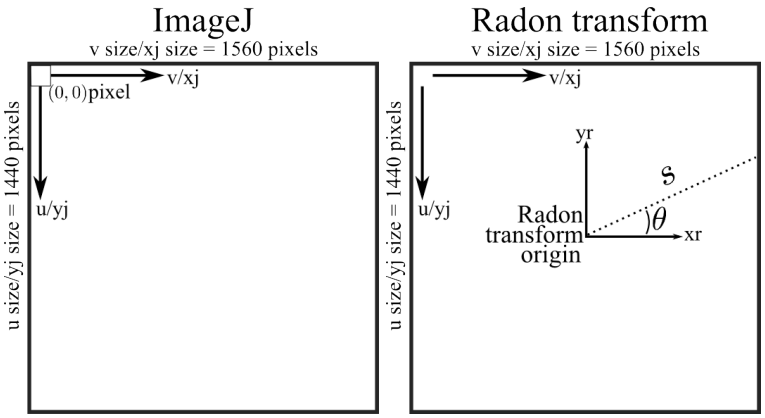

Figure 3.12: Diagram showing the ImageJ and Radon coordinate systems.

adding padded zeros to the image boundaries based on the center of mass measurement. This step can be seen in Fig. 3.13. After the unbiased measurement of (θ, s), the u, and v, again must be translated back to the correct ImageJ coordinates before calibration. The above equation now becomes:

$$u_j = \frac{u_c}{(1 - u_c(\frac{u_{size}}{2} + c_y) - v_c(\frac{v_{size}}{2} + c_x))} \qquad v_j = \frac{v_c}{(1 - u_c(\frac{u_{size}}{2} + c_y) - v_c(\frac{v_{size}}{2} + c_x))} \tag{3.3}$$

where the variables c_y and c_x are the measured deviation of the center of mass of the image relative to the center of the image.

The Radon transform is applied to the data at a very fine angular increments twice, once between $-3^o \leq \theta \leq 3^o$ for the left and right edges and again between $87^o \leq \theta \leq 93^o$ for the top and bottom edges. As it is known that the collimator edges are positioned around the center of the image and the approximate size of the original image is 1560×1440 pixels, unnecessary data from the Radon transform can be removed for s positions which are outside of the image boundary and at the center of the image which does not contain an edge. Now each of the four edges are segmented out of transform space, and can be located individually. Table 3.1 shows the approximate range in which each edge can be located.

3.2.2 General method of edge detection

Figure 3.14 gives a general overview of the four step process to finding the parameters of each edge $(\widetilde{\varphi}, \widetilde{s})$. The first step is simply the application of the Radon transform (RT)

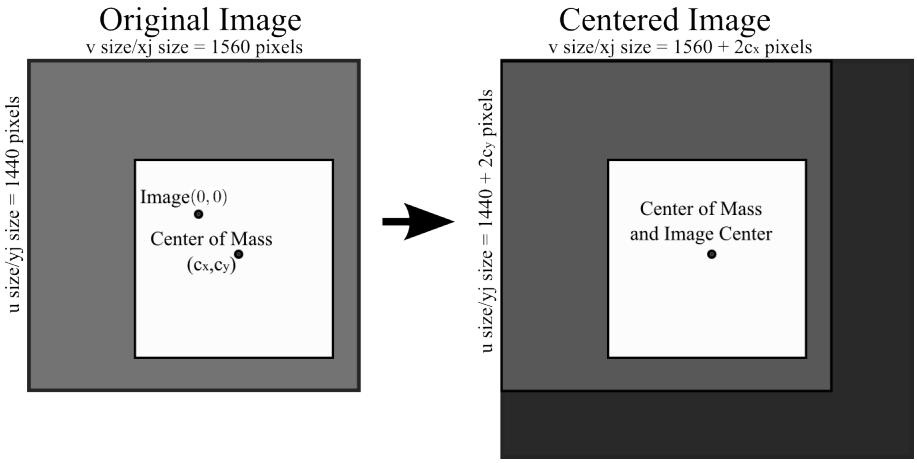

Figure 3.13: A depiction of the process of centering the image center of mass by expanding the image boundaries, a process necessary to correct edge angle measurement bias.

Table 3.1: Collimator edge segmentation in Radon transform space (relative to center of image) and original image space of size 1560×1440 pixels.

Edge	Angle	s position range	range in original image coordinates
Left	$-3^o \leq \theta \leq 3^o$	$-780 \leq s_L \leq -390$	$0 \leq x_j/v \leq \frac{1}{4}v_{size}$
Right	$-3^o \leq \theta \leq 3^o$	$390 \leq s_R \leq 780$	$\frac{3}{4}v_{size} \leq x_j/v \leq v_{size}$
Bottom	$87^o \leq \theta \leq 93^o$	$-720 \leq s_B \leq -360$	$0 \leq y_j/u \leq \frac{1}{4}u_{size}$
Top	$87^o \leq \theta \leq 93^o$	$360 \leq s_T \leq 720$	$\frac{3}{4}u_{size} \leq y_j/u \leq u_{size}$

at the angle θ_i (where $i = 1...k$, k is the number of angular increments in the angular range of each edge seen in Table 3.1). The segmentation of the edge follows (as described in the subsection above) to obtain the one dimensional Radon transform (1D RT) as a function of position, s, at the angle θ_i, for each edge in the image. Next, in step two, a Gaussian filter can be applied to the 1D RT in order to reduce any effects from noise exhibited in the 1D RT. The third step involves the characterization of the curve/line in the 1D RT which represents the edge. This characterization is intended to give a quantized measure of how close the angle θ_i is to the actual edge angle, φ. As described above (Section 3.1.1.1) the estimated angle, $\widetilde{\varphi}$, of the edge can be defined by several different methods. The way in which this edge is estimated is the most important step of the edge determination process and establishes the accuracy of the angle estimation.

Lastly, the above three steps are repeated at each angular increment, $\theta_{i=1...k}$, with, k angular increments in the angular range. The quantized measure determined in step

three is then plotted versus the angle θ_i of the Radon transform for each edge. The rationale is that the angle θ_i which corresponds to the maximum (or minimum) of this curve indicates the true edge angle, $\theta = \varphi$. The position of the edge, $\widetilde{s}$, at the estimated edge angle $\widetilde{\varphi}$, is determined from the 1D RT at the angle $\widetilde{\varphi}$ by some criteria which should be reproducible for all edges. The $\widetilde{s}$ position is established at a specific position along the edge of the curve which is consistent for all edges.

Recall that given the limits on the angular sensitivity, when sampling the Radon transform at a very fine angular increment (much finer than the sensitivity) results in the measurement of redundant data. In this case the angle which corresponds to the best estimate of $\widetilde{\varphi}$ would be the mid point of these identical (or nearly identical) measurements. In cases where the edge angle is slightly skewed from the pixel rows or columns, sampling at a very fine angular increment produces a curve seen in Fig. 3.15(b). Measuring the same values of this curve at an even finer angular increment would eventually produce the peak plateau of Fig. 3.15(a). Simply finding the max in either of these two cases does not produce the best result (see [Zhang & Couloigner 2007]). To estimate correctly the edge angle from the curve of step four, a method which effectively selects all points of the curve which are close to the top/plateau while neglecting others must be implemented. This can be accomplished in three main ways. The simplest method would be to apply a mean filter to the curve of the value vs θ, which has the same length as the minimum angular sensitivity, and then finding the maximum. Another method could be to measure the difference between points adjacent to the max point, and apply a threshold which selects only points which are close to their neighbors extending outward from the max point of the curve. And the third possible method could be to use a normalized Gaussian filter instead of a mean filter with a standard deviation based on the minimum angular sensitivity in order to identify the midpoint of the plateau or peak of the curve of step four. Once appropriate selection criteria have been implemented the best estimate of the angle of the edge $\tilde{\varphi}$ is simply the average of all the points at θ_i which compose the plateau or peak of the curve (refer to Fig. 3.15).

To improve the method of edge detection for real or noisy simulation data a 1D Gaussian filter can be applied to the 1D RT in step two. The Gaussian filter acts to smooth any noise effects exhibited on the 1D RT which then allows a more accurate characterization of the 1D RT in step three, and subsequently a better edge angle estimation. The Gaussian filter should only locally smooth the noise effects in the 1D RT and therefore should have a standard deviation (SD) likely between $\sqrt{2}$ and 6 pixels (in s) depending on the level of noise and width of the edge in the image. This standard deviation can be varied and optimized based on both the noise level and the implemented method of 1D RT characterization in order to improve edge detection.

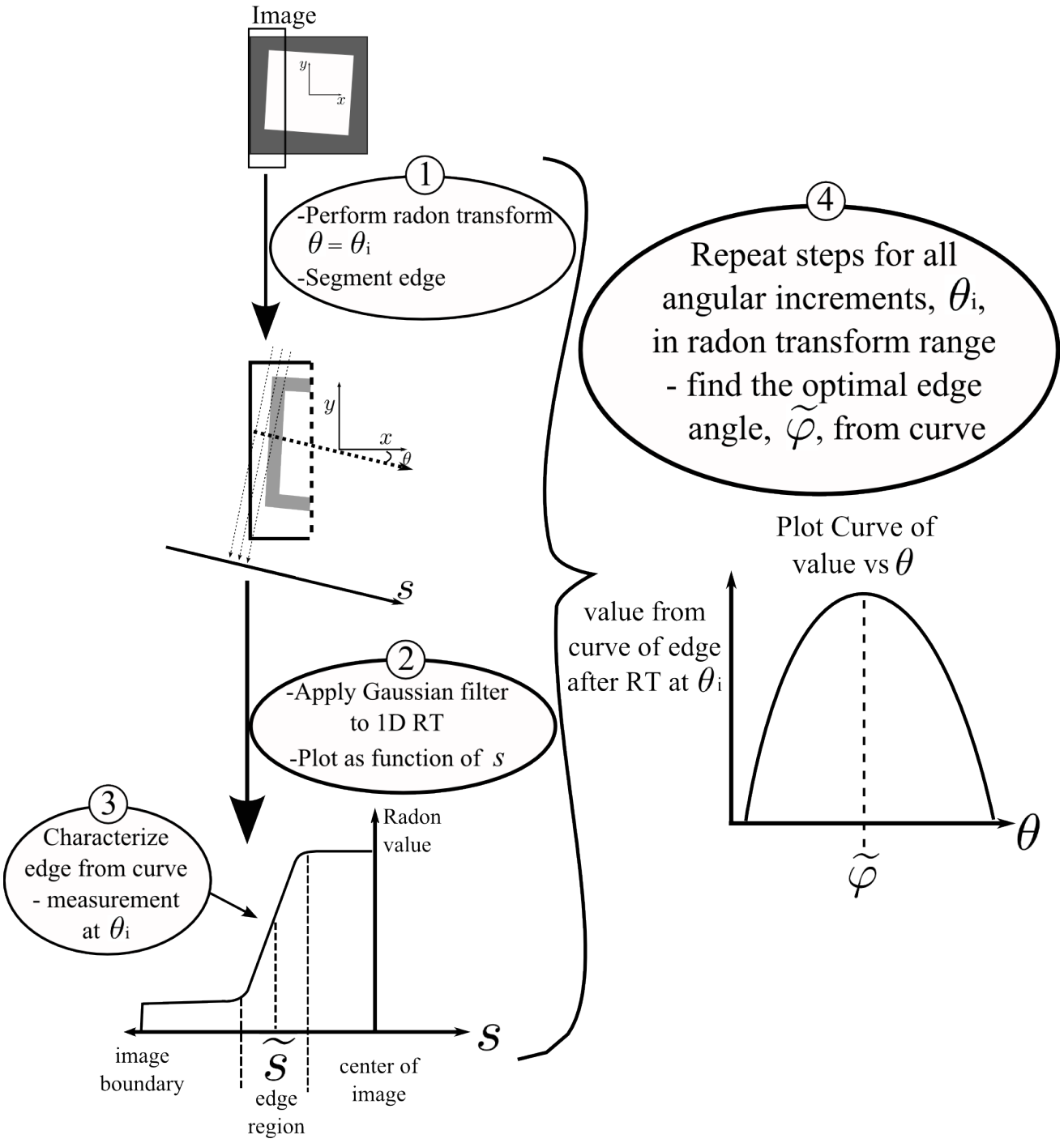

Figure 3.14: Flow chart of edge angle and position determination process.

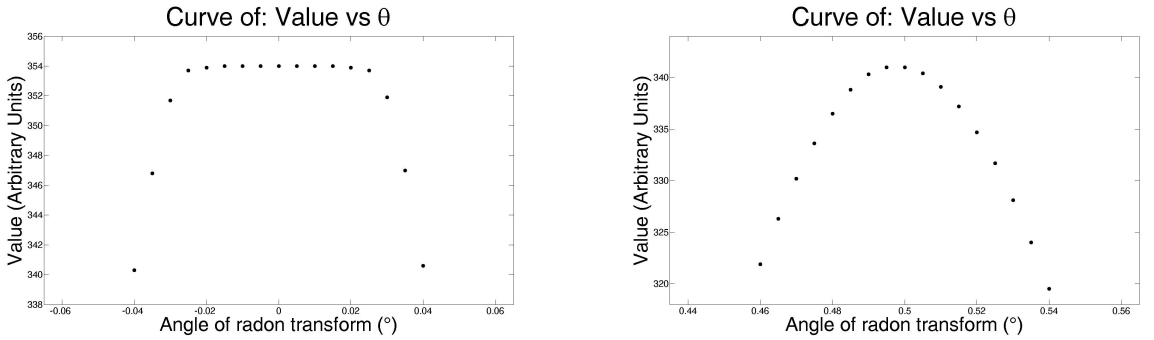

(a) A plateau is formed when the edge angle $\varphi = 0^o$ (b) A curve is formed when the edge angle $\varphi \neq 0^o$

Figure 3.15: Example of the peak of curves of some value measured in step three versus Radon transform angle, θ. A plateau is formed when the edge angle $\varphi = 0^o$ (a), while a curve is formed when the edge angle $\varphi \neq 0^o$ (b).

The main objective of this research is to find the best possible way of estimating the angle $\widetilde{\varphi}$ and position $\widetilde{s}$ of the edges in the image in the presence of noise and C-arm deformation (ie. the translation and rotation of the detector relative to the source). The characterization of the curve of the edge in the 1D Radon transform must be optimal and furthermore the measurement of the angle $\widetilde{\varphi}$ from the curve of value vs angle of step 4 must also be handled properly.

Finally once $(\widetilde{\varphi}, \widetilde{s})$ has been determined Eqn. (3.3) is used to determine the parameters of the line required for the homography calibration method of section 2.1, equation (2.3) (page 33).

3.2.3 Approach to edge detection by various methods

The edge angle parameter must be very accurately measured for the reason that the calibration process is highly sensitive to errors in the angle of the edge (refer to section 3.3.1). This measurement must be robust when noise is present in the image and there is simulated or real C-arm deformation, which is represented by variation of the detector position and orientation during acquisition of projection images. As described in section 3.1.1.1 (page 52) there are three characteristics which can be used to estimate the edge angle from the 1D RT at a given angle: the maximum (or minimum) of the derivative of the RT of the edge profile, the slope of the linear part of the 1D RT of the edge profile, or the sharpness of the smooth shoulders of the 1D transform. In order to describe this 1D profile we have implemented five different methods: a simple derivative filter, fitting

a line to the linear part of the profile of the 1D RT, fitting a 3rd degree polynomial to the edge profile in the 1D RT, by directly using the 1D RT or by fitting a cubic spline to the entire profile, and using the derivative of a Gaussian filter to compute the gradient of the image. From these five methods there are several different ways of measuring the edge characteristics, and within that there are different ways to make the estimation from the curve of step four. Evidently there are many possible variations for the process of edge detection and the best possible method, which is robust in the presence of noise and C-arm deformation, must be chosen.

Furthermore edge detection can be accomplished by means of the Canny filter and Hough transform as well as the Canny edge detector (CED) and Radon transform to give a comparative evaluation of the accuracy of our implemented methods of edge detection with the commonly used or standard techniques from the literature.

All methods have the capability for edge detection in either real or simulation data however experimentation to determine the best method is done on simulation data with noise, and with randomly simulated C-arm deformation. The image size, pixel size and approximate width of the edge in pixels are required as inputs for most of the methods. Further, it is assumed that the image field of view, that is the portion of the image which does not contain an edge is at least one half of the image dimensions. Being as all four edges are found by the same process, the following subsections give the edge detection description of only the left edge in the image which produces a 1D Radon transform edge profile which increases along s with similar behavior as is shown in Fig. 3.8 and Fig. 3.7(b).

Below is a summary of the most relevant details of the extensive experimentation to determine the best method of edge detection. The two methods of standard edge detection commonly used in the literature are also described. The results of this experimentation and their comparison with standard techniques will be shown in section 3.3.2 to determine the most reliable method of edge detection.

3.2.3.1 Maximum of the derivative of the Radon transform

The first attempt for measuring the angle of the edge can be obtained from the maximum (for the left edge) of the derivative of the 1D Radon transform at each angular increment (step three of Fig. 3.14) by the application of a simple derivative filter. Recall that a line in an image is observed as a peak in transform space, however an edge in the image would be seen as a peak (for the left and bottom) or trough (for the right and top edges) in the derivative of transform space. The 1D RT of a given edge at $\varphi = 0^o$ (Fig. 3.7)

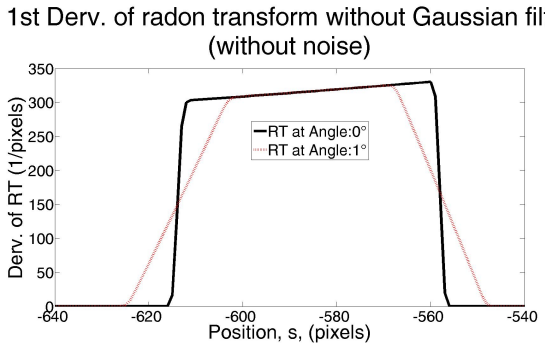

Figure 3.16: Derivative of the Radon transform at $\theta = 0°$ and $\theta = 1°$, of an edge at $\varphi = 0°$, without noise, and without Gaussian filtering.

after the application of a derivative filter can be observed in Fig. 3.16. The 1D RT at a given angle can be characterized by the value of the max of this curve, the max of the first derivative.

Once the max of the derivative of the Radon transform has been found, step four of Fig. 3.14 can be completed in several different ways. The logical first estimation of $\widetilde{\varphi}$ would be simply the maximum of the curve of the max at each θ_i versus all θ's, hence the global max of the derivative of the 2D Radon transform within the angular and positional range for each edge. The position $\widetilde{s}$ can be estimated by the position of the maximum of the derivative at the estimated $\widetilde{\varphi}$.

Recall that in order to estimate the angle of the edge most accurately the Radon transform is obtained at a very fine angular increment. As a result of this when the edge is at $\varphi = 0^o$ the Radon transform contains a slight bias in which the angle across the diagonal of a line or in our case across the diagonal of a row or column of pixels gives a slightly higher maximum, see Fig 3.17 for an example of peak of the curve of step four containing this bias.

As described in section 3.2.2 the maximum of the curve of step four could be determined using the difference between points, a mean filter, or a Gaussian filter. Consequently the peak of the curve of step four (seen in Fig. 3.17) would be averaged and the result removes the bias and gives the best estimate of the angle given it's sensitivity.

For real or simulated data with noise a Gaussian filter should be exploited in step two to improve the measurement of the maximum of the derivative. The Gaussian filter obviously affects the derivative of the 1D RT, Fig. 3.18(a), though the effect on the 1D RT should be the same for all Radon transform angles. Fig. 3.18(b) shows that undoubtedly a Gaussian filter is required in order to measure the max of the derivative

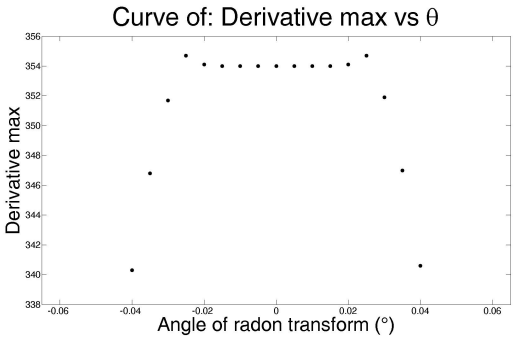

Figure 3.17: Example of the peak of the curve of the maximum of the derivative versus the angle for an edge with angle $\varphi = 0^o$ in a noiseless image. Note that a slight bias occurs due to the integration of the line along the diagonal of the image columns.

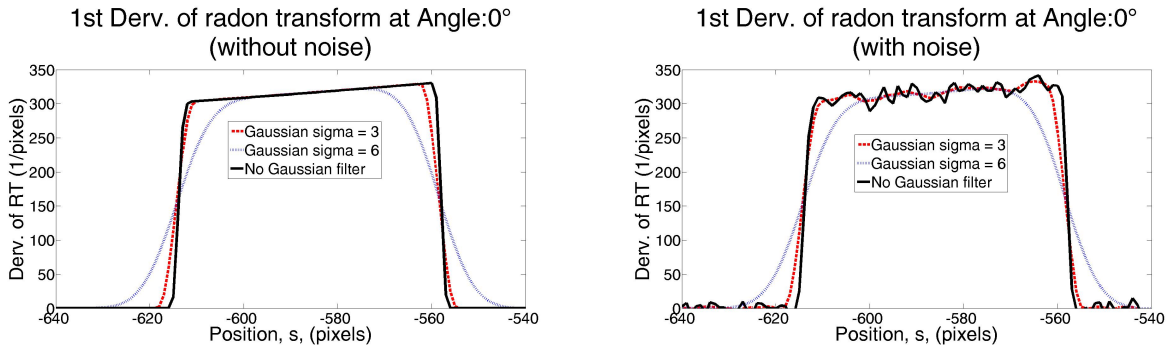

(a) First derivative of RT without noise

(b) First derivative of RT with noise

Figure 3.18: The first derivative of the Radon transform at $\theta = 0°$ of an edge at $\varphi = 0°$, with Gaussian filters of varied standard deviations used to reduce noise affects.

in the presence of noise.

Based on the results the best method in which to find the max from the curve of step four must be chosen and as well the appropriate standard deviation of the implemented Gaussian filter should be optimized for the best results.

3.2.3.2 Slope of the edge profile fit to a straight line

The next, and more elaborate approach to characterize the curve of the 1D Radon transform was by fitting a line to the edge profile at each angular increment, θ_i, (step three) and then constructing a curve of the slope of this line versus the angle of the

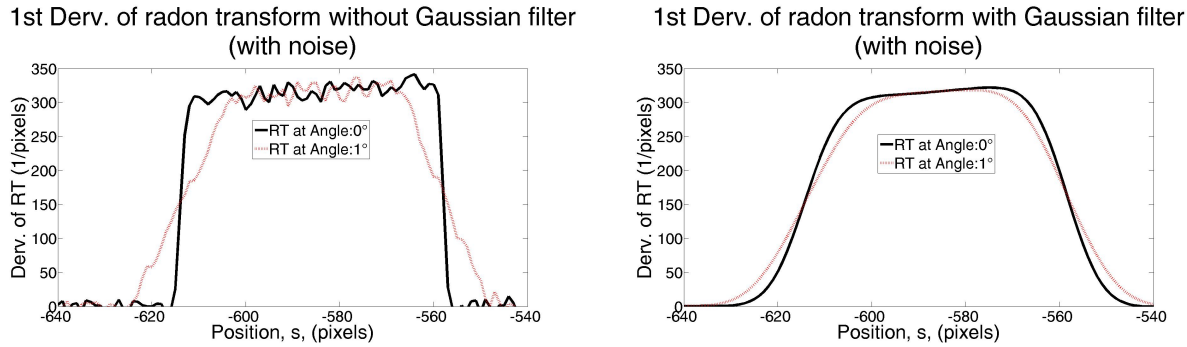

(a) First derivative of the RT without Gaussian filtering

(b) First derivative of the RT with Gaussian filtering

Figure 3.19: First derivative of the Radon transform at, $\theta = 0°$ and, $\theta = 1°$, of an edge at $\varphi = 0°$, with noise, and (a) without Gaussian filtering, and (b) filtering using a Gaussian function with a standard deviation of 6.

RT (step four). For this approach the points to include in the fit of the line must be intelligently chosen and this process can be accomplished in several ways. The intent is to find the best line fit to the edge profile in the 1D RT at each RT angular increment, θ_i, see Fig. 3.7(b). This is equivalent to finding a horizontal line which best describes the plateau of the peak of the curves in Fig. 3.19(a). The way in which the points are selected from the edge profile to fit to the straight line is very important and will certainly depict the slope of the fitted line and the manner in which the slope changes as the RT angle changes.

The first straightforward technique to select the points required to fit a line to the edge profile would be the application of a mean filter to the derivative of the 1D RT with approximately the same width as the linear part of the edge profile at each angular step. The process involves the application of a derivative filter, $D = \left[+\frac{1}{2}, 0, -\frac{1}{2}\right]$, followed by a mean filter of the prescribed length n, $M = \left[\frac{1}{n}, \frac{1}{n}..., \frac{1}{n}\right]$, which creates a filter (of length $n + 2$) which finds the slope between the first and last two points of the mean filter length.

$$D \star M = \left[-\frac{1}{2n}, -\frac{1}{2n}, 0, 0..., 0, \frac{1}{2n}, \frac{1}{2n}\right]$$

The length of the mean filter (MF) would be based on the approximate measurement of the edge profile width in the image. Essentially the number of points are chosen before hand and the slope between the first and last point of the desired length is found for all possible combinations of points in the 1D RT of the edge. This is equivalent to finding

the maximum average value for the desired number of points in the curve of Fig. 3.16. Thus depending on the length, the mean filter could incorporate the smooth low contrast shoulders when $\theta \neq \varphi$ (the edges of the curve in Fig. 3.16) and only the linear part of the 1D RT when $\theta = \varphi$ (the peak of the curve of Fig. 3.16).

An alternative approach to using a mean filter of the desired length would be to fit the desired number of points to a straight line from a specified location in the 1D RT. The number of points to select should be slightly less than the width of the edge in the image, and in order for the best edge angle estimation the number should be precisely chosen. Once the appropriate number of points has been ascertained the location from the 1D RT in which to acquire these points to fit to the line must be determined. From the 1D RT of the edge, at any angular increment, a derivative filter and then a mean filter, which has roughly the same length as the width of the edge, can be utilized to give the approximate location of the midpoint of the linear portion of the 1D RT. Lastly, the points from the 1D RT to fit to a line are evenly selected from both sides of the position of this midpoint for each angular step.

To improve the estimation of the slope of the linear part of the 1D RT, as well as the selection of the points which contribute to the fit of the line, a Gaussian filter can be applied to the 1D RT as described in section 3.2.2.

Once the value of the slope of the fitted line is measured using one of the above methods of point selection for the given angle and the process is repeated for each angular increment to construct the curve of step four, the correct angle of the edge remains to be measured from the curve. This can be accomplished by implementing one of the three methods described in section 3.2.2 to best estimate the mid-point of the peak or plateau of the curve of step four (illustrated in Fig. 3.15).

In all cases, the position $\tilde{s}$ can be estimated by finding the midpoint, in s, of the curve/line in the 1D RT at the estimated edge angle, $\widetilde{\varphi}$. Hence this includes the application of a derivative filter followed by a mean filter with a specified length, an identical process to the first method described above.

The results can be improved by optimizing the number of points to fit to the line in the preceding method, and equivalently the length of the mean filter of the first method. Furthermore, as in all cases, the standard deviation of the Gaussian filter should be optimized to obtain the best result based on the method.

3.2.3.3 Radon transform fit to a 3rd degree polynomial

The next approach to describe the 1D RT of the edge was to fit the 1D RT edge profile (linear part and the smooth shoulder regions) to a 3rd degree polynomial. A 3rd degree polynomial can provide a very good fit to the curves seen in Fig. 3.7(b) without including the zero slope regions which provide no information. A polynomial fit gives a simple four parameter characterization of the 1D RT while also acting to reduce any noise affects. A Gaussian filter (GF) can be used in addition to a polynomial fitting to locally reduce noise before the fit. Subsequently, with an accurate 3rd degree polynomial fit, there are several possible ways to determine the estimate of the edge angle from this polynomial.

After taking the Radon transform, applying a Gaussian filter and segmenting each of the 4 edges from the 1D transform, the points to be incorporated into the polynomial fitting can be selected similar to the previous subsection. The application of a derivative filter and then a mean filter (with a length designated by the width of the edge) to the 1D RT at any angular increment can be implemented to determine the midpoint of the curve. From this midpoint the appropriate number of points from the 1D RT can be selected evenly from each side of the midpoint to give the desired curve. The goal is to keep the shoulder regions of the 1D RT while omitting the zero slope regions.

From the fitted polynomial the value which allows the estimate of the angle can be given in several different ways. In order to measure the characteristic of the slope of the 1D RT the first derivative of the polynomial can be computed and its maximum obtained ($\max(f')$) for each angular increment to generate the curve of step four. Similarly, the position in the polynomial in which the second derivative is equal to zero, s_z, can be found and the value of the first derivative at this position ($f'(s_z)$ with $f''(s_z) = 0$) can be used to give the slope of the 1D RT edge profile. Additionally, the first derivative can be computed and the points at which the first derivative is equal to zero determined, s_1 and s_2 with $f'(s_1) = f'(s_2) = 0$, and the slope of the line in the 1D RT can then be computed between these two points. And lastly, the first derivative can be obtained and summed or averaged for all points in the polynomial, average($f'(s)$) for all s. All of these methods are similar yet would produce slightly different results and would require optimization of the number of points selected to fit the polynomial as well as possible optimization of the standard deviation of the Gaussian filter used.

Another method can be implemented which does not measure the slope of the 1D RT but instead measures the characteristic of the curvature of the shoulder regions described in section 3.1.1.1. From the fitted polynomial the R^2 correlation coefficient can be calculated which gives a measure of how closely the polynomial models the original data. Being as a third degree polynomial is suited for fitting to a smooth distribution

such as that seen in Fig. 3.7(b), and is poorly suited for fitting to a straight and flat distribution such as that seen in Fig. 3.7(a), as the Radon transform angle θ approaches the edge angle φ, the 1D RT changes from Fig. 3.7(b) to Fig. 3.7(a). At this point, when $\theta \approx \varphi$, the polynomial has the worst fit and therefore the lowest R^2 correlation coefficient. The angle of the edge can be measured from the minimum of the curve of the R^2 correlation coefficient versus the Radon transform angle. To measure this characteristic the polynomial fit must include slightly more points than the width of the edge in the image. Both the number of points used to fit the polynomial, and again the standard deviation (SD) of the Gaussian filter should be optimized to obtain the best edge angle estimation.

As before the estimation of the edge angle from the constructed curve can be handled by either the MF, difference method, or GF. The estimation of the position $\widetilde{s}$ can then be simply given by the position of the midpoint of the curve in the 1D RT at the RT angle $\theta_i = \widetilde{\varphi}$.

3.2.3.4 Fitting of the entire edge profile to a cubic spline or directly using the 1D RT

The characterization of the 1D RT by either a line or 3rd degree polynomial relies on a process of selecting a desired position and number of data points to create the fit, which can be potentially erroneous and problematic to define for all conditions. The next method attempts to avoid this selection process. The exact number and location of the selection of data points from the 1D RT profile can be avoided by characterizing the entire profile: linear region, smooth shoulders, and zero slope tails, either by using a cubic spline fit or directly using the portion of the 1D RT which contains the edge profile. A cubic spline has the ability to fairly accurately fit the edge profile and can then be exploited to both reduce noise and gives a parametrization to determine a measure of how close the RT angle, θ, is to the actual edge angle, φ, for each angular step. Alternatively, when directly using the 1D RT noise affects can be reduced or removed using a GF and measurements from the first and second derivative can be used to estimate the edge angle and position.

The number of data points to fit the cubic spline can be arbitrarily chosen to be some amount larger than the edge length (for example twice the edge length). Likewise the location to select the data points can be arbitrarily chosen in the vicinity of the edge profile such as the midpoint of the curve as in the previous two selection procedures. Neither the number of data points or the position the data points are obtained from the 1D RT should negatively affect the edge angle and position estimation.

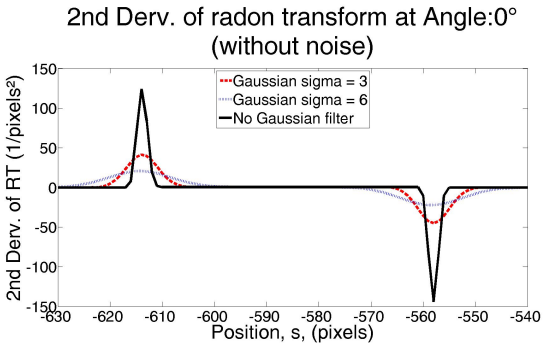

(a) Second derivative of the 1D RT

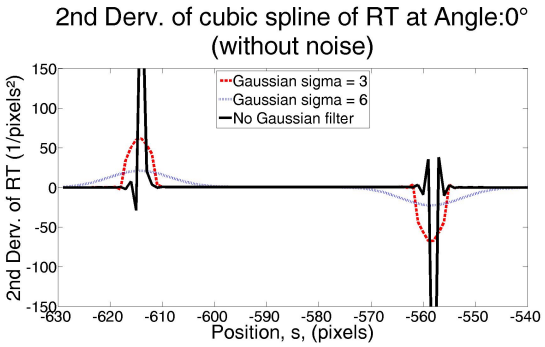

(b) Second derivative of the cubic spline fit to the 1D RT

Figure 3.20: Second derivative of the 1D RT (with $\theta = \varphi$) treated with and without a Gaussian filter and in the absence of noise. Note the slight errors in the cubic spline fit at the sharp corners of the 1D RT without the application of a Gaussian filter. (The 1D RT can be seen in Fig. 3.7(a).)

The cubic spline fit and the 1D RT should behave similar to the actual edge profile and thus their 1st and 2nd derivative should resemble Fig. 3.19 and Fig. 3.9(b) (when $\theta = \varphi$). It can be informative to examine how the 2nd derivative behaves as the angle of the Radon transform approaches the edge angle, $\theta \to \varphi$. When in noiseless conditions the 2nd derivative resembles Fig. 3.9(b) as would be expected, see Fig. 3.20. The 2nd derivative of the cubic spline fit contains some slight approximation errors when there is no Gaussian filter for smoothing, although these effects disappear when the 1D RT is smoothed with a Gaussian filter. Fig. 3.21, shows that in the presence of noise and with the application of a Gaussian filter the 2nd derivative can give a good indication of the curvature of the shoulder regions of the curve which can provide a means of estimating the edge angle.

The 2nd derivative generates both a maximum and minimum designating the curvature in the two shoulder regions. This measure of curvature can be quantized by finding the max and min value from the 2nd derivative using a mean filter to reduce any inaccuracies before measurement of the max/min peaks in the curve of Fig. 3.21. This low pass mean filter should have a length of about twice the standard deviation of the Gaussian filter used for smoothing the 1D RT. The average of the absolute value of the max and min can then be used to estimate the edge angle from the curve of this average versus the Radon transform angle. The estimation of the position of the edge can simply be given by the mid-point between the position of the max and min peaks in the 2nd derivative of the 1D RT or the cubic spline. The position of the edge can

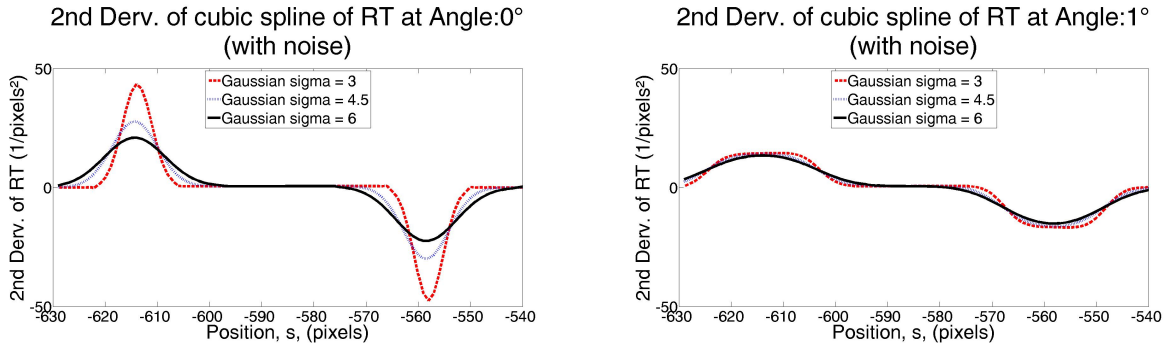

(a) Second derivative of the cubic spline fit with $\theta = \varphi$ (b) Second derivative of the cubic spline fit with $\theta \neq \varphi$

Figure 3.21: Second derivative of the cubic spline fit to the 1D RT with noise, and treated with various Gaussian filters. Note that the 2nd derivative of the 1D RT behaves in the same manner as the the cubic spline fit to the data.

be estimated by the midpoint between the located max and min peaks at the estimated edge angle $\widetilde{\varphi}$.

The cubic spline fit to the 1D RT can also be exploited to measure the slope of the edge profile in the 1D RT. The most accurate way to obtain a measure of the slope of the best fit line in the cubic spline would be to apply a simple mean filter to the derivative of the cubic spline. This process is similar to finding the slope in the 1D RT by the application of a derivative filter followed by a mean filter (as in the previous slope methods on page 64) and similarly the procedure requires selection of the optimal MF length to produce the best estimation of $\widetilde{\varphi}$. The estimation of the edge position can then be given by the midpoint of the MF at the estimated angle of the edge.

As before the edge angle estimate from the curve can be made using one of the three methods, and the standard deviation of the Gaussian filter should be optimized to obtain the best estimates of $(\widetilde{\varphi}, \widetilde{s})$.

3.2.3.5 Edge detection using the Canny edge detector and Hough transform

Edge detection should also be performed using the Canny edge detector (CED) and Hough transform for the purposes of comparison of the above implemented methods with the standard edge/line detection techniques. For most line or edge detection requirements the Canny edge detector (CED) and Hough transform are sufficient for accurate detection of any and all edges in an image. To reiterate our methods have been developed to obtain the most accurate localization of thick straight edges for the purpose

of sensitive intrinsic calibration of the imaging system.

Before edge detection by the application of the CED and Hough transform the same image pre-processing occurs as described in section 3.2.1. The image is then treated by the CED from the Matlab image processing toolbox [Matlab 2014]. To locate edges in the image, the CED calculates the gradient of the image by applying the derivative of a 2D Gaussian filter DGF with a specified standard deviation. The standard deviation used should be optimized based on the width of the edge profile to ensure accurate detection of the edges. Afterward, two thresholds are applied to the gradient of the image to detect strong and weak edges. The strong and weak edges are linked resulting in a new binary image which should only contain the edge features in the image. The Hough transform (HT) would then create a histogram in the (θ, s) space from the binary image. Similar to the Radon transform the edge features will be displayed as peaks in the Hough transform space. Finding the max of the HT will identify the (θ, s) parameters of the edge.

As before, for optimum sensitivity the HT should be applied at very fine angular sampling. The result would be multiple peaks of the same value at several angles but at the same position, s, in the HT space for each segmented edge. A simple average of all the angular increments which contain a peak will give the best estimate of the angle of the edge by the CED and HT.

3.2.3.6 Edge detection using the Canny edge detector and Radon transform

Given that the Hough transform is actually a special case of the Radon transform a comparison of edge detection using the Canny edge detector (CED) and the Radon transform should also be performed and should provide better results than the simplified Hough transform.

The Canny edge detector can be implemented as in the above description using an optimized standard deviation of the derivative of a Gaussian filter (DGF) to identify the edges. From the resulting binary image the RT can be used with the same angular sampling as in the above methods to localize the edge. After application of the Radon transform neither the Gaussian filter nor a derivative filter would be needed being as these steps were already completed by the CED. Simply finding the maximum in the 1D RT of the binary image can be used to generate the curve of step four required to estimate the angle of the edge. This estimation can be accomplished by one of the three methods described in section 3.1.1.1.

3.2.3.7 Derivative of a Gaussian filter after the Radon transform - Canny filter type approach

A final method should be implemented to mimic the Canny edge detector approach without the thresholding used for edge localization and the conversion of the resulting image to binary. The goal is to first use the Radon transform on the unchanged image of the edges and then to mimic the Canny filter of the CED to localize the edge in the 1D RT at each angular increment. A drawback to using the CED for edge detection in our case is the conversion of the image to binary. This confines the edge localization to a single line of discrete pixels in the image opposed to many lines of varied intensity displayed by the thick edges in the original image.

The Canny filter indicates the presence of an edge by the maxima in the gradient of the image obtained using the derivative of a Gaussian filter (DGF), with a standard deviation based on the width of the edge (ie. a large SD required for a wide edge). The large standard deviation of the DGF not only acts to reduce the noise effects in the image but also functions as a type of low pass filter on the value of the derivative of the edge in the image to retrieve the best estimate of this value along the entire edge profile.

By using the RT and then the derivative of a 1D Gaussian filter with a large SD the mechanism of edge detection is similar to using a small low pass Gaussian filter (to reduce noise), a derivative filter, and then a mean filter with roughly the same length as the edge profile in the image (described in subsection 3.2.3.2). Both methods obtain, to some extent, a type of average value for the derivative of the edge profile in the 1D RT.

The maximum after application of the DGF to the 1D RT can be found at each angular increment, θ_i, to construct the curve of the max versus angle θ. The edge angle can then be estimated from this curve using one of the three methods of determining the midpoint of the peak or plateau of the curve. The position of the edge, similar to other methods, can be estimated as the position of the max in the 1D RT obtained at the estimated edge angle $\theta = \widetilde{\varphi}$ after the application of the DGF. For this approach only the SD of the DGF should be optimized for the best result, which should be close to the SD of the Canny edge detector from the above two methods.

3.3 Optimal Method of Edge Detection

This section presents the comparative evaluation of the various methods of edge detection described in subsection 3.2.3. The results were acquired using simulation data with noise and simulated C-arm deformation. The methods are evaluated based on the accuracy

of the estimated edge parameters $(\widetilde{\varphi}, \widetilde{s})$ relative to the ground-truth (GT) (φ_T, s_T), and the accuracy of the calculated IC parameters from the homography method relative to the GT simulation conditions.

Initial comparisons of the methods are completed with both noise and deformation. Following this, more stringent experimentation can be performed on the simulation data to show the effect of noise and deformation on the accuracy of the edge detection.

Before observing the results of edge detection by various methods it would be beneficial to first analyze the limits of the sensitivity of the measurements of $(\widetilde{\varphi}, \widetilde{s})$ and how this effects the results of edge detection. The sensitivity analysis will give a measure of how accurately we can estimate the edge angle parameters given the experimental conditions, image size, and edge dimensions in the image. This will also give a measure of how accurately the homography intrinsic calibration can be attained. The following subsection investigates the theoretically attainable results.

3.3.1 Sensitivity of $(\widetilde{\varphi}, \widetilde{s})$ measurement

The purpose of this investigation is to identify how errors in the estimation of the edge parameters of the four edges in each image contribute to errors in the homography calibration (HC) and then determine the limits of the estimation of the IC parameters. The objective is to find the typical error on the estimation of the edge parameters, σ_φ and σ_s, obtain the theoretical simulation ground-truth (GT) edge parameters (φ_T, s_T), and preform the HC using the GT edge parameters with the addition of the typical error σ_φ, σ_s and observe the effect on the calibration parameters.

Measurement error of edge parameters The sensitivity of $(\widetilde{\varphi}, \widetilde{s})$ is dependent on the angular step size at which the RT is obtained at and also the limits on the positional accuracy of the Radon transform implemented by Matlab [Matlab 2014]. The simulated edges were modeled to be approximately the same length and width as the collimator edge in a real projection image from the C-arm described in section 1.2.1. The width of the edge in both simulated and real images should be roughly $w = 59$ pixels while the length should be around $l \approx 1000$ pixels. For a 1560×1440 image with edges approximately 1000 pixels in length and 60 pixels in width the minimum angular sensitivity in the estimation of the edge angle, the sensitivity when $\varphi = 0^o$, was found to be $\theta_{min} = 0.55°$. As a result of this, for all of the following experiments, the angular increment (or step size) at which the Radon transform was obtained at was $\theta_{ss} = 0.05°$.

As shown in Fig. 3.15 for most edge orientations the step size of $\theta_{ss} = 0.05°$ is a good

angular increment to obtain the RT, whereas there are some orientations (those which are very close to 0^o and 90^o) in which the accuracy in the measurement is diminished. We will not take this reduction of accuracy into account in this sensitivity study being as edge orientations which are very close to 0^o or 90^o rarely occur.

The Matlab implementation of the RT allows any (computationally feasible) angular increment, however the positional increment, in s, is fixed at the pixel size, $s_{ss} = 1$ pixel.

Under the assumption that we can determine the estimate of $\widetilde{\varphi}$ and $\widetilde{s}$ to the nearest 0.05° and nearest pixel, the error on this measurement would be $\sigma_\varphi = \pm 0.0025^o$ and $\sigma_s = \pm 0.5$ pixel.

Simulation ground-truth edge parameters In order to evaluate the sensitivity of the measurement of the edge parameters 50 projection images of parallelepiped objects attached to the x-ray source were simulated with random variation of the six parameters designating the detector position and orientation relative to the source, (z_d, y_d, x_d, Φ, Θ, η). (See subsection 3.3.2 and Table 3.1 for more details).

The ground-truth (GT) theoretically generated edge parameters (φ_T, s_T) were generated by using the simulation deformation conditions, (z_d, y_d, x_d, Φ, Θ, η), to project the known simulated phantom onto the rotated and translated detector. The phantom consists of four 3D parallelepiped objects intersecting along their thickness. The four points of intersection which are at the midpoint of the parallelepiped thicknesses are projected. These points correspond to the corners of the phantom and corners of the FOV (see Fig. 3.11 for a depiction of the four intersections points at the corners of the FOV). From these four projected locations on the detector, (u_i, v_i), the angle and positions of the edges relative to the image are calculated to give $(\varphi_{T\,i}, s_{T\,i})$ for $i = 1...4$.

Homography calibration using (φ_T, s_T) When using the ideal edge parameters, (φ_T, s_T), of all four edges of each projection image in a simulation scan with varying C-arm deformation (z_d, y_d, x_d, Φ, Θ, η), in order to complete homography intrinsic calibration (IC) with the initial view intrinsic calibration given by the GT simulation conditions, $\mathbf{K_0^{Sim}}$ (see subsection 2.1.2 for more details), the result yields the exact GT IC parameters for each projection of the scan within round off error. This result validates the homography calibration using the line parameters (Eqn. (2.3)).

Recall that if the initial view IC parameters, $\mathbf{K_0}$, contains an error, the error is directly transferred to all the calculated intrinsic parameters creating a bias or systematic offset in $\mathbf{K}_i$ (where i signifies the projection number, and $0 < i \leq n - 1$).

3.3.1.1 Static deviation in (φ_T, s_T)

An informative evaluation would be to vary each edge parameter of each of the four edges individually by a static amount, the estimated measurement error, $\sigma_\varphi = \pm 0.0025^o$, $\sigma_s = \pm 0.5$ pixel, and observe the effects on the IC. Both the IC error from a single static deviation in $\varphi_{T\,i}$ or $s_{T\,i}$ as well as the IC error due to a combinations of errors in the angle or position of the four edges can be studied.

There are two possible manners in which a single static deviation in $\varphi_{T\,i}$ or $s_{T\,i}$ could affect the IC parameters. From the 50 simulated projections, if a single edge parameter contained a static offset for a single projection image, generally a static or systematic error in the IC parameters of that projection would be produced. In the other case, IC error could occur if all 50 projection images contained the same static offset of one of the edge parameters.

The HC determines the IC parameter variation between each projection image and a reference image - projection one in this case. If a static error occurred only in the edge parameters of the reference image then all other IC parameters would acquire a bias or static error. Therefore both of the above effects can be studied simultaneously by instead varying the last 49 of 50 projection images by the static offset.

When adding a single deviation to one of the edge angle parameters (for example to the left edge angle $[\varphi_L \pm \sigma_\varphi, \varphi_R, \varphi_B, \varphi_T]$) a systematic error results in u_s or v_s with slight variations (or stochastic errors) seen in the focal length f, (see Table 3.2). When multiple static errors influence the edge angle parameters the systematic and stochastic errors either combine or cancel each other out.

A similar but slightly more complex result occurs due to a static error in the edge position, which is shown in Table 3.3. A single static deviation in one of the positions of the edges produces a systematic error in f with slight systematic and stochastic errors in the u_s and v_s intrinsic parameters. Again when these static deviations are combined the errors on the IC parameters either cancel or combine.

This study shows how errors in the edge parameters can combine and additionally gives an estimate of the affect of the typical edge angle and position error.

3.3.1.2 Uniform random deviation within error range

During implementation of edge detection the edge parameters can (typically) contain any level of error within the error range ($\sigma_\varphi = \pm 0.0025^o$, $\sigma_s = \pm 0.5$ pixel) and furthermore all estimated edge parameters would contain error simultaneously. To investigate the

Table 3.2: Investigation of error in homography calibration due to static deviations in the edge angle parameter by the typical measurement error $\sigma_\varphi = \pm 0.0025^o$. Note the dash indicates no static or stochastic error. (Note L, R, B, T, specify the left, right, bottom, and top edges respectively).

Static Deviation	f error [pixels]	u_s error [pixels]	v_s error [pixels]
$\varphi_L \pm \sigma\varphi$	0.0 ± 0.1	$\pm 1.6 \pm 0.0$	-
$\varphi_R \pm \sigma\varphi$	0.0 ± 0.1	$\mp 1.6 \pm 0.0$	-
$\varphi_B \pm \sigma\varphi$	0.0 ± 0.1	-	$\pm 1.6 \pm 0.0$
$\varphi_T \pm \sigma\varphi$	0.0 ± 0.1	-	$\mp 1.6 \pm 0.0$
$\varphi_L \pm \sigma\varphi$ $\varphi_R \pm \sigma\varphi$	-	-	-
$\varphi_B \pm \sigma\varphi$ $\varphi_T \pm \sigma\varphi$	-	-	-
$\varphi_L \pm \sigma\varphi$ $\varphi_R \mp \sigma\varphi$	0.0 ± 0.2	$\pm 3.2 \pm 0.0$	-
$\varphi_B \pm \sigma\varphi$ $\varphi_T \mp \sigma\varphi$	0.0 ± 0.2	-	$\pm 3.2 \pm 0.0$
$\varphi_{All} \pm \sigma\varphi$	-	-	-

effects of this measurement error on the IC during standard implementation a uniform random error (within the error range) was added to the GT edge angle and position. This random error was added to all 8 parameters of each of the 50 projection images, and the effect on the IC was observed. To obtain more statistically significant results this procedure was repeated 20 times for all 50 simulated projection images.

Assuming the level of measurement error is correct this experiment should give a good indication of the best attainable accuracy on the IC. To compare the sensitivity of the IC from the edge angle measurement versus the edge position measurement this analysis was performed with uniform random error added only to the edge angle (using the GT edge position) and subsequently with uniform random error added only to the edge position. Table 3.4 displays the variation or error in the focal length and orthogonal projection of the source onto the detector due solely to the measurement error of edge detection.

3.3.2 Various methods of edge detection

Simulation studies give a controlled and reliable way to determine the best method (or methods) of edge detection, and determine how well they compare to the standard edge detection techniques used in the literature. For these studies 50 projection images of parallelepiped objects attached to the x-ray source were simulated to model the edges of

Table 3.3: Investigation of error in homography calibration due to static deviations in the edge position parameter by the typical measurement error $\sigma_s = \pm 0.5$ pixels. Note the dash indicates no static or stochastic error.

Static Deviation	f error [pixels]	u_s error [pixels]	v_s error [pixels]
$s_L \pm \sigma_s$	$\mp 1.4 \pm 0.0$	0.0 ± 0.1	$\pm 0.3 \pm 0.2$
$s_R \pm \sigma_s$	$\pm 1.4 \pm 0.0$	0.0 ± 0.1	$\pm 0.2 \pm 0.2$
$s_B \pm \sigma_s$	$\mp 1.4 \pm 0.0$	$\mp 0.2 \pm 0.2$	0.0 ± 0.1
$s_T \pm \sigma_s$	$\pm 1.4 \pm 0.0$	$\mp 0.3 \pm 0.2$	0.0 ± 0.1
$s_L \pm \sigma_s$ $s_R \pm \sigma_s$	-	-	$\pm 0.5 \pm 0.0$
$s_B \pm \sigma_s$ $s_T \pm \sigma_s$	-	$\mp 0.5 \pm 0.0$	-
$s_L \pm \sigma_s$ $s_R \mp \sigma_s$	$\mp 2.8 \pm 0.0$	0.0 ± 0.2	0.0 ± 0.4
$s_B \pm \sigma_s$ $s_T \mp \sigma_s$	$\mp 2.8 \pm 0.0$	0.0 ± 0.4	0.0 ± 0.2
$s_{All} \pm \sigma_s$	-	$\mp 0.5 \pm 0.0$	$\pm 0.5 \pm 0.0$

Table 3.4: Investigation of error in homography calibration due to uniform random deviations in the edge angles and positions by the typical measurement error: $\sigma_\varphi = \pm 0.0025^o$ and $\sigma_s = \pm 0.5$ pixels.

Random Deviation	f error [pixels]	u_s error [pixels]	v_s error [pixels]
All edge angles	0.1	1.3	1.3
All edge positions	1.6	0.3	0.4
All positions and angles	1.6	1.3	1.3

the collimator. For 49 of these 50 projection images the detector position and orientation contained random deformation (described in greater detail in subsection 1.2.3.3 page 23) while the first projection had no deformation. As described in the above, projections in which the edge angle is parallel to the rows or columns (ie. no simulated deformation) have decreased sensitivity in the measurement of the edge parameters. This decrease in sensitivity can be examined in this first deformation free projection image. Being as the IC variation of every view is related back to this initial view, if the collimator edges in this initial view are mis-estimated this mis-estimation would be seen as a static bias in the IC of all other projection images. Therefore, the edge detection bias or sensitivity can be observed as the mean difference between the homography IC and the GT IC.

The level of noise from a real C-arm projection image (gain corrected projection image) was measured as described in subsection 1.2.1.3. This level of noise was applied

to the simulation data as Gaussian noise in order to generate simulation results which approximately modeled the real data conditions (subsection 1.2.3).

To determine the accuracy of each line detection method the measured edge angle and position were compared to the GT or ideal edge angle and position. From the GT simulation conditions the ideal collimator edge positions and orientations in the image were determined by projecting four intersection points from the four simulated parallelepiped objects onto the detector. Being as the parallelepiped objects are 3D and intersect along their thickness, the thickness midpoint was projected to obtain (φ_T, s_T). The difference between the estimated and GT edge angle was found for each edge, $\Delta\varphi_i = \widetilde{\varphi} - \varphi_T$, and for each projection image the root-mean square (RMS) of the difference of all four edges was calculated to give a measurement of the error of the angle for the given edge detection method of a single projection, $\varphi_{RMS} = \frac{1}{2}\sqrt{\Delta\varphi_1^2 + \Delta\varphi_2^2 + \Delta\varphi_3^2 + \Delta\varphi_4^2}$. The same was done for the measured position of the edge $\Delta s_i = \widetilde{s} - s_T$ and the average RMS position difference was calculated for each projection. From all 50 projection images the average of the RMS differences of each projection were calculated to give a measure of the total RMS error for the entire scan.

The limits on the estimation of the edge angle and position $(\widetilde{\varphi}, \widetilde{s})$ were presented in subsection 3.3.1 ($\sigma_\varphi = \pm 0.0025^o$, $\sigma_s = \pm 0.5$ pixels). From theses errors the error on the calculated quantities of φ_{RMS}, s_{RMS} and their respective averages for all projections can be ascertained: $\sigma_{\varphi_{RMS}} = \sigma_\varphi/\sqrt{4}$ and $\sigma_{s_{RMS}} = \sigma_s/\sqrt{4}$ (when the number of edges in the image is four), and $\sigma\bar{\varphi_{RMS}} = \sigma_\varphi/\sqrt{4}/\sqrt{n}$ and $\sigma\bar{s_{RMS}} = \sigma_s/\sqrt{4}/\sqrt{n}$ where n is the number of projections. As noted above, in the following experiments the number of projections is, $n = 50$, thus: $\sigma_{\varphi_{RMS}} = 0.001^o$, $\sigma_{s_{RMS}} = 0.3$ pixels, $\sigma\bar{\varphi_{RMS}} = 0.0002^o$, $\sigma\bar{s_{RMS}} = 0.04$ pixels.

A secondary more stringent evaluation of edge detection involves comparison of the IC parameters obtained from the estimated $(\widetilde{\varphi}, \widetilde{s})$ with the GT directly. From the GT simulation conditions the GT intrinsic calibration (IC) parameters were calculated. After determination of the edge parameters $(\widetilde{\varphi}, \widetilde{s})$ the homography calibration (HC) was completed as described in section 2.1 to estimate the IC parameters from the given line detection method. For the calibration procedure, the initial view IC was provided by the GT simulation conditions, K_0^{Sim} (see subsection 2.1.2 for more details). The difference between these IC parameters were calculated for each projection image, and their average difference, standard deviation, and max absolute error are used to demonstrate the capability for IC from the given line detection method.

For all edge detection methods, the estimate of the edge angle from the curve of some measured value versus the RT angle θ (the curve in step four of Fig. 3.14), was completed

by implementing either a mean filter, a Gaussian filter or using the difference method as described in subsection 3.1.1.1. Evaluations showed that the difference in performance or accuracy between the three methods was negligible and all three methods could be said to be equally suitable. Therefore for all the following experiments the more simplistic mean filter was used. The length of this mean filter is dependent on the minimum angular sensitivity, θ_{min}, and the RT angular increment, θ_{ss}: $l_{MF} = \theta_{min}/\theta_{ss}$. In the following studies the minimum angular sensitivity was observed to be $\theta_{min} = 0.55^o$ (see example Fig. 3.13) leading to the choice of $\theta_{ss} = 0.05°$ for the RT angular increment, and thus the mean filter length is given from the above $l_{MF} = 11$.

For use in the implementation of edge detection by some methods, the width was measured from a simulated image, $w = 59$ pixels. Additionally, the image field of view, that is the portion of the image which does not contain an edge was assumed to be at least half of the image dimensions, 780×720.

As shown in subsection 3.3.1 from a precision and statistics point of view there is no difference in measurements of the IC parameters to within $f \pm 2$ pixels and $u_s/v_s \pm 1$ pixels (refer to Table 3.4). However to better contrast the differences in the estimation of the edge parameters and calculated IC parameters by the various methods we show an additional significant figure.

3.3.2.1 Maximum of the derivative of the Radon transform

The first derivative of the profile of the edge seen in Fig. 3.9a exhibits that in the absence of noise the linear part of the edge profile (when $\theta = \varphi$) is not quite constant and actually the position of the maximum of the derivative is at the highest position of the linear part of the profile. This indicates that in the absence of noise the max derivative should be a good indicator of the edge angle, see Fig. 3.22(a) . However, this measure is susceptible to small fluctuations in the edge profile and thus causing it's unsuitability in the presence of noise.

When this method was attempted on simulation data with noise, the result verified the angle and position of the maximum of the derivative of the 2D Radon transform are highly sensitive to noise, see Fig. 3.22(b). Gaussian filters (GF) with standard deviations between $\sqrt{2}$ to 9 pixels were applied to the 1D RT to reduce the affects of noise (see Fig. 3.23 with a SD of 6 pixels). Table 3.5 shows the error in the angle and position of the detected edge by this method when compared to the angle calculated from the GT simulation conditions. Using the estimated angles and positions of the edges the IC parameters were calculated and compared to the GT IC parameters for all

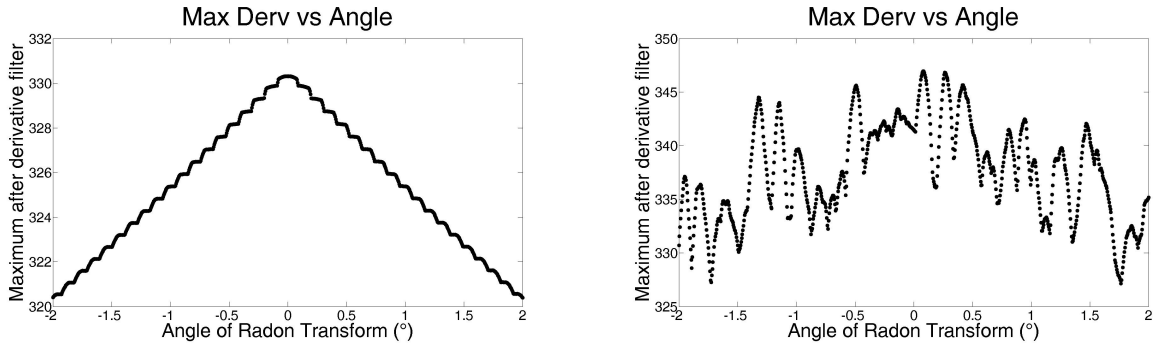

(a) Max of the 1D RT derivative vs angle without noise

(b) Max of the 1D RT derivative vs angle with noise

Figure 3.22: Curve of the maximum of the derivative of the 1D RT versus the Radon transform angle, with and without noise and without application of Gaussian smoothing filter.

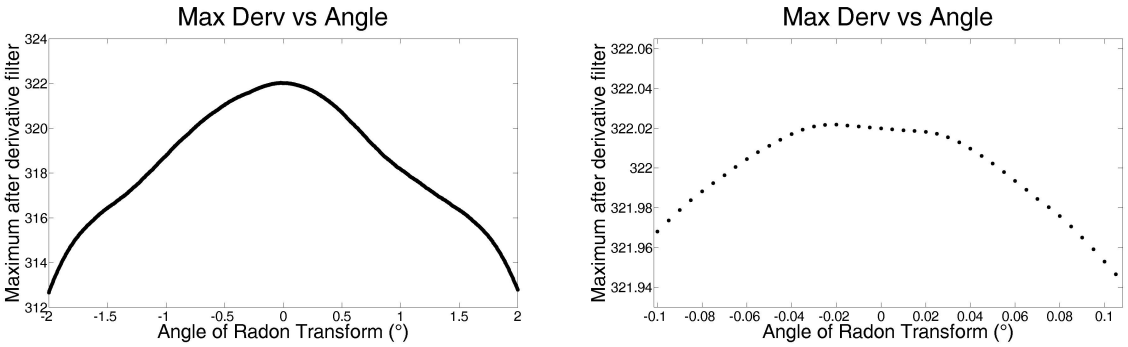

Figure 3.23: Curve of the maximum of the derivative of the 1D RT versus Radon transform angle without C-arm deformation ($\varphi = 0°$), with noise and with Gaussian filter with a standard deviation of 6.

50 projection images, see Table 3.6. As in all cases the mean filter technique was used to determine the estimate $\widetilde{\varphi}$ from the curve of step four (seen in Fig. 3.23).

Table 3.5: Error in the angle and position of the detected edge, $(\widetilde{\varphi}, \widetilde{s})$ **from the max of the derivative of the 1D RT**, compared to the theoretical edge angle and position, (φ_T, s_T). Noise was present and a Gaussian filter with a SD of **6 pixels** was applied to the 1D RT. The RMS error for a single projection is shown for the first three projections and the average RMS error of all 50 projections is given.

Projection or Average	Angle [deg]	Position [pixels]
Proj. 1	0.093	10.1
Proj. 2	0.195	11.5
Proj. 3	0.123	10.2
Avg. of all 50	0.1012	11.08

Table 3.6: Comparison of the homography calibration parameters calculated using the estimated $(\widetilde{\varphi}, \widetilde{s})$ **from the max of the derivative of the 1D RT**, and the ground-truth initial view IC parameters $\mathbf{K_0^{Sim}}$. The max absolute value, SD, and mean values were found for the difference between the estimated and ground-truth IC parameters of 50 projections simulated with random C-arm deformation and noise. (All units are pixels.)

Difference with K^{Sim}	K^H_{Sim} Δf	K^H_{Sim} Δu_s	K^H_{Sim} Δv_s
mean	-9.4	-9.9	-163.8
SD	15.3	88.5	101.6
max $\lvert \cdot \rvert$	75.4	215.4	383.3

As described in section 3.3.1 above, the GT angle and position are calculated by projecting the intersection point of the parallelepiped which lies at the center of their thickness. Thus, the projected position should be approximately at the middle of the edge profile. As shown in Fig. 3.19(b), the position of the max of the derivative of the profile is not at the center of the edge profile but instead at the edge of the profile. Due to this the estimated edge position (with noise and with the application of a GF with a SD of 6 pixels) is about 11 pixels away from the ideal position (Table 3.5). As illustrated in section 3.3.1 an error such as this would produce an error on the estimated focal length and the principle point of: $f \pm 1$ pixel, and $u_s/v_s \pm 5$ pixels. Accounting for this effect would not significantly improve the result presented in Table 3.6.

3.3.2.2 Slope of the edge profile fit to a straight line: DMF & LF methods

Fitting a line to the 1D RT is likely the most apparent and straightforward way to determine when the edge angle matches the RT angle. However, finding the most appropriate line to fit to the noisy data is a difficult task. A low pass smoothing operation (a Gaussian filter), should be implemented to reduce the noise and then the correct line length and position, in s, in the 1D RT must be established to achieve the best line fit to the data.

The following methods were both thoroughly investigated: the method of determining a measure of the slope of the edge in the 1D RT by using a derivative filter followed by a mean filter (termed the DMF method) of a prescribed length and the method of fitting a line to the 1D RT with a predefined length in s. For both of these methods the Gaussian noise smoothing filter as well as the length of the fitted line, or equivalently the length of the mean filter, were varied to determine the variables which give the best result. The methods were attempted with a SD ranging between $\sqrt{2}$ and 9 pixels with the length of the line/mean filter ranging between $49 - 63$ pixels (recall edge width is $w = 59$ pixels). The optimization of the line/DMF length along with the low pass GF is an entangled problem. A large SD will smooth the corners of the 1D RT of the edge profile, as shown in Fig. 3.7, and thus affects the optimal line length to fit to the 1D RT.

When using the derivative and mean filter to measure the slope of the best line fit between two points separated by the prescribed MF length the analysis was completed with varying SD of the Gaussian filter and varying edge lengths. First, the analysis was completed using a MF length of 56 pixels and varying the SD from $\sqrt{2} - 9$ pixels. This showed that a lower SD, between $2 - 5$ pixels, gave the best result. Next the analysis was completed using a GF with SD of 2, 3, 4, and 5 pixels and varying the MF length from $49 - 63$ pixels. This then showed that with low SD the best result was obtained with a longer edge lengths:

- for a SD of 2 pixels, the best result was obtained with MF length $55 - 57$ pixels
- for a SD of 3 pixels, the best result was obtained with MF length $53 - 55$ pixels
- for a SD of 4 pixels, the best result was obtained with MF length $52 - 54$ pixels
- for a SD of 5 pixels, the best result was obtained with MF length $50 - 52$ pixels

All of the results were similar with the best result from all data sets attained with a SD of 4 pixels and a length of 53, see Tables 3.7 & 3.8.

Similarly the method of fitting a line to the 1D RT (LF method) with a predefined

Table 3.7: Error in the angle and position of the edge detected using **a derivative filter followed by a mean filter with a length of 53 pixels**, compared to the theoretical edge angle and position. Noise was present and a Gaussian filter with a SD of **4 pixels** was used. The RMS error for a single projection is shown for the first three projections and the average RMS error of all 50 projections is given.

Projection or Average	Angle [deg]	Position [pixels]
Proj. 1	0.006	1.5
Proj. 2	0.003	1.3
Proj. 3	0.004	1.1
Avg. of all 50	0.0046	1.45

Table 3.8: Comparison of the homography calibration parameters calculated using the estimated $(\widetilde{\varphi}, \widetilde{s})$ from the **derivative filter and mean filter method** with the ground-truth initial view IC parameters $\mathbf{K_0^{Sim}}$. The max absolute value, SD, and mean values were found for the difference between the estimated and ground-truth IC parameters of 50 projections simulated with random C-arm deformation and noise. A Gaussian filter with a standard deviation of **4 pixels** was applied to the 1D RT. (All units are pixels.)

Difference with K^{Sim}	K^H_{Sim} Δf	K^H_{Sim} Δu_s	K^H_{Sim} Δv_s
mean	-3.6	-7.7	-0.3
SD	1.5	4.3	4.8
max $\lvert \cdot \rvert$	7.2	17.6	13.5

length was attempted with various SDs of the GF and varying line lengths. The results were better with lower SDs and higher line lengths, with the best result obtained with a length of 60 pixels and SD of 2, see Tables 3.9 & 3.10. Again the results were very similar and showed only small variations when the line length and SD differed from 60 and 2 pixels respectively.

The two methods of measuring the slope of the profile of the edge in the 1D RT both perform quite well in comparison to the other methods. These methods, however, perform well for different reasons. The second method fits the best line to all the data points at the position designated by the mid point of the line at some RT angle. The first method, on the other hand, fits a line through only the first and last two data points in the line of prescribed length although the best line (line with the highest slope) is

Table 3.9: Error in the angle and position of the edge detected by **fitting a line of length 60 pixels** to the 1D RT, compared to the theoretical edge angle and position. Noise was present and the SD of the Gaussian filter was **2 pixels**. The RMS error for a single projection is shown for the first three projections and the average RMS error of all 50 projections is given.

Projection or Average	Angle [deg]	Position [pixels]
Proj. 1	0.007	1.1
Proj. 2	0.002	1.4
Proj. 3	0.004	1.6
Avg. of all 50	0.0045	1.67

Table 3.10: Comparison of the homography calibration parameters calculated by **fitting a line of length 60 pixels** to the 1D RT to estimate the edge angle and position, with the ground-truth initial view IC parameters $\mathbf{K_0^{Sim}}$. The max absolute value, SD, and mean values were found for the difference between the estimated and ground-truth IC parameters of 50 projections simulated with random C-arm deformation and noise. A Gaussian filter with a standard deviation of **2 pixels** was applied to the 1D RT. (All units are pixels.)

Difference with K^{Sim}	K^H_{Sim} Δf	K^H_{Sim} Δu_s	K^H_{Sim} Δv_s
mean	3.5	-7.2	9.6
SD	2.0	4.0	4.5
max $\lvert \cdot \rvert$	7.5	16.6	18.4

found for all positions along the edge profile of the 1D RT. Therefore to find the best fitted line to the edge profile all the data points should be included in the fit to the line, of prescribed length, and the best line should be found for all positions. This leads to an adaptation which combines the benefits of the previous two methods by measuring the slope of the best fit line through all the data at all feasible positions along the edge profile in the 1D RT.

Using this adaptation to measure the slope of the best fit line, evaluations were completed with varied SDs of the GF and varied line lengths. The results displayed only a slight improvement in the estimation of the IC parameter describing the focal length, (an improvement of 0.3 pixels in the standard deviation of Δf), while there was an increase in computation time. Thus the advantages of the adaptation were deemed

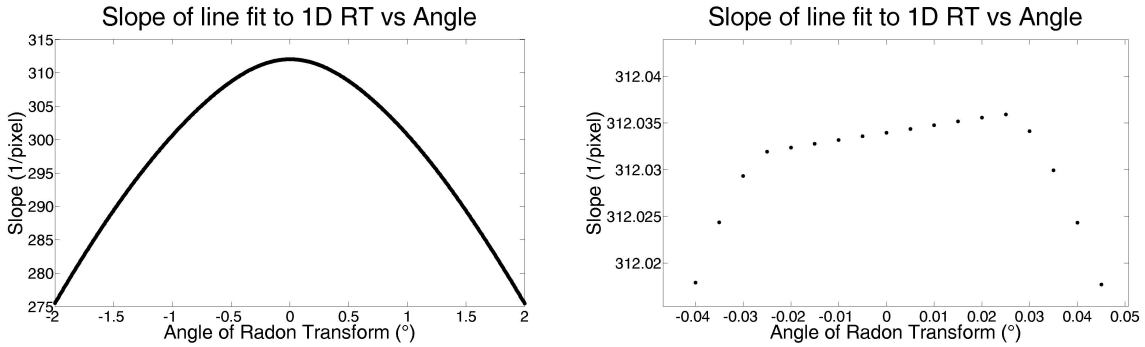

(a) Slope vs RT angle θ without simulated C-arm deformation $\varphi = 0^o$

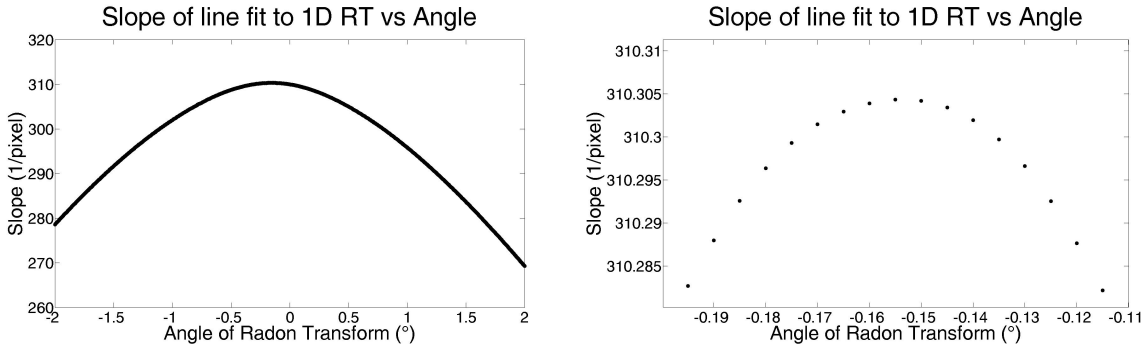

(b) Slope vs RT angle θ with simulated C-arm deformation $\varphi = -0.152^o$

Figure 3.24: Curve of the slope of the best fit line to the 1D RT versus the Radon transform angle (slope vs RT angle θ) in the presence of noise. The length of the fitted line was 60 pixels and a GF with a SD of 2 pixels was applied to the 1D RT.

insignificant and unnecessary.

All three methods of determining the slope of the fitted line displayed similar curves of the slope vs the RT angle which is displayed in Fig. 3.24.

The two methods presented above (derivative of a mean filter (DMF) & linear fit (LF)) ultimately provide the most accurate edge determination methods.

3.3.2.3 Radon transform fit to a 3rd degree polynomial

In order to portray the 1D RT and reduce noise affects a polynomial of degree three was fit to the 1D RT. The polynomial allows many different means of estimating the edge angle and position however the number of data points and possibly also the position in which to acquire these points must be determined. Several of these different means of

estimating $(\widetilde{\varphi}, \widetilde{s})$ were implemented but ultimately none of them performed better than the previous method of fitting a line to the 1D RT indicating that using a polynomial to characterize the 1D RT does not provide an advantage over a simple linear fitting.

In this study their were four methods implemented to measure the slope of the edge profile and one method to measure the curvature of the shoulder regions of the edge profile in the 1D RT. In all five implementations both the length of the fitted polynomial and the standard deviation of the GF were altered to find the optimal result.

Three of the four implemented methods of measuring the slope gave very similar results: the method of finding the maximum of the first derivative of the polynomial, $\max(f')$, using the value of the first derivative of the polynomial at the s_z location in which the second derivative of the polynomial is equal to zero, $f'(s_z)$ with $f''(s_z) = 0$, and finding the two locations, s_1 and s_2 in which the first derivative is equal to zero $f'(s_1) = f'(s_2) = 0$ and then finding the line through these two points.

The fourth method of determining the slope of the 1D RT fit with a polynomial gave significantly better results compared to the other methods but was still not an improvement over a simple line fitting to the 1D RT. This method involved averaging all values of the first derivative of the polynomial. This approach is similar to the first implemented method of measuring the slope of the profile in the previous subsection (applying a mean filter with specified length to the derivative of the 1D RT). The optimal result was achieved with a polynomial length of 60 pixels and standard deviation of 2 pixels, see Tables 3.11 & 3.12.

Table 3.11: Error in the angle and position of the edge detected by **averaging all the values of the first derivative** of the fitted polynomial with length **60 pixels**, compared to the theoretical edge angle and position. Noise was present and the SD of the Gaussian filter was **2 pixels**.

Projection or Average	Angle [deg]	Position [pixels]
Proj. 1	0.004	0.7
Proj. 2	0.005	1.6
Proj. 3	0.004	1.5
Avg. of all 50	0.0051	1.30

The last attempt of estimating the edge angle and position from the polynomial involved measuring the R^2 correlation coefficient of the polynomial recognizing that the RT angle for which $\theta \approx \varphi$ would have the lowest R^2 value when the polynomial length was somewhat greater than the length of the edge profile in the image. The best result

Table 3.12: Comparison of the homography calibration parameters calculated by **averaging all the values of the first derivative** of the fitted polynomial with length **60 pixels** to estimate the edge angle and position, with the ground-truth initial view IC parameters $\mathbf{K_0^{Sim}}$. A Gaussian filter with a standard deviation of **2 pixels** was applied to the 1D RT. (All units are pixels.)

Difference with K^{Sim}	K^H_{Sim} Δf	K^H_{Sim} Δu_s	K^H_{Sim} Δv_s
mean	-1.9	-7.7	1.9
SD	3.3	4.8	5.6
max$\lvert\cdot\rvert$	9.0	17.8	12.3

was obtained when the polynomial length was 69 pixels and the GF had a SD of 3 pixels, as shown in Tables 3.13 & 3.14.

Table 3.13: Error in the angle and position of the edge detected by measuring **the $\mathbf{R}^2$ correlation coefficient** of the fitted polynomial with length **69 pixels**, compared to the theoretical edge angle and position. Noise was present and the SD of the Gaussian filter was **3 pixels**.

Projection or Average	Angle [deg]	Position [pixels]
Proj. 1	0.008	0.6
Proj. 2	0.010	0.9
Proj. 3	0.006	0.4
Avg. of all 50	0.0087	1.06

Table 3.14: Comparison of the homography calibration parameters calculated by measuring **the $\mathbf{R}^2$ correlation coefficient** of the fitted polynomial with length **69 pixels** to estimate the edge angle and position, with the ground-truth initial view IC parameters $\mathbf{K_0^{Sim}}$. A Gaussian filter with a standard deviation of **3 pixels** was applied to the 1D RT. (All units are pixels.)

Difference with K^{Sim}	K^H_{Sim} Δf	K^H_{Sim} Δu_s	K^H_{Sim} Δv_s
mean	-0.3	-9.0	-6.0
SD	2.7	9.4	7.9
max$\lvert\cdot\rvert$	5.8	26.4	22.1

3.3.2.4 Fitting of the edge profile to a cubic spline or directly using the 1D RT

Methods of fitting a cubic spline to the 1D RT or using the 1D RT directly were implemented to attempt to improve edge detection by avoiding the potentially error prone process of selecting the position and number of data points used to estimate the edge angle. Additionally a cubic spline fit provides a very good fit to the data which can characterize the 1D RT while reducing noise affects.

The 2nd derivative of the cubic spline fit was exploited to measure the curvature of the shoulder regions of the edge profile in the 1D RT after application of various Gaussian filters to reduce noise before fitting. Similarly the 1D RT was smoothed various GFs and it's 2nd derivative was used directly to estimate the edge angle. Both procedures gave analogous results with the optimal result obtained using a GF with a SD of 7 pixels. Tables 3.15 & 3.16 show the results of the estimation of the edge angle from the 2nd derivative of the 1D RT.

Table 3.15: Error in the angle and position of the edge detected using the **2nd derivative of the 1D RT** (or equivalently the cubic spline), compared to the theoretical edge angle and position. Noise was present and the SD of the Gaussian filter was **7 pixels**.

Projection or Average	Angle [deg]	Position [pixels]
Proj. 1	0.009	1.5
Proj. 2	0.006	1.6
Proj. 3	0.004	1.6
Avg. of all 50	0.0067	1.59

The 1st derivative of the cubic spline was also used to measure the slope of the edge profile using a MF. The SD of the GF and the length of the MF were varied with the best result, displayed in Tables 3.17 & 3.18, obtained with a MF length of 55 pixels and a SD of 3 pixels.

3.3.2.5 Edge detection using the Canny edge detector and Hough transform

To evaluate our edge detection techniques against the commonly used techniques in the literature edge detection was completed using the Canny edge detector (CED) for detection of edge pixels and then the Hough transform to localize the edge structure

Table 3.16: Comparison of the homography calibration parameters calculated using the **2nd derivative of the 1D RT** (or equivalently the cubic spline) to estimate the edge angle and position, with the ground-truth initial view IC parameters $\mathbf{K_0^{Sim}}$. A Gaussian filter with a standard deviation of **7 pixels** was applied to the 1D RT. (All units are pixels.)

Difference with K^{Sim}	K^H_{Sim} Δf	K^H_{Sim} Δu_s	K^H_{Sim} Δv_s
mean	-2.0	-10.2	-4.7
SD	2.1	5.4	7.9
max$\lvert\cdot\rvert$	7.4	23.4	30.7

Table 3.17: Error in the angle and position of the edge detected using the **1st derivative of the cubic spline**, compared to the theoretical edge angle and position. Noise was present and the SD of the Gaussian filter was **3 pixels**.

Projection or Average	Angle [deg]	Position [pixels]
Proj. 1	0.003	1.5
Proj. 2	0.004	1.6
Proj. 3	0.002	1.1
Avg. of all 50	0.0049	1.53

Table 3.18: Comparison of the homography calibration parameters calculated using the **1st derivative of the cubic spline** to estimate the edge angle and position, with the ground-truth initial view IC parameters $\mathbf{K_0^{Sim}}$. A Gaussian filter with a standard deviation of **3 pixels** was applied to the 1D RT. (All units are pixels.)

Difference with K^{Sim}	K^H_{Sim} Δf	K^H_{Sim} Δu_s	K^H_{Sim} Δv_s
mean	-2.7	-4.2	-0.7
SD	1.5	5.3	4.7
max$\lvert\cdot\rvert$	7.1	15.1	10.4

from the binary image. The CED was implemented via the Matlab image processing toolbox [Matlab 2014] with two inputs: the standard deviation (SD) of the derivative of a Gaussian filter (DGF) applied to find the image gradient, and the low and high threshold to identify and link the weak and strong (respectively) edge pixels.

For our simulated image it was found that the default thresholding by the CED based on the maximum of the image gradient was sufficient to find and link all the edge pixels. The SD of the DGF was varied from $2-50$ pixels to find the SD which produces the best result relative to the GT edge parameters, (φ_T, s_T), and GT IC parameters. The results varied mildly when the CED was provided with a SD in the range from $10-35$ pixels with the best result achieved between $17-19$ pixels.

Table 3.19 presents the root-mean square (RMS) edge error for the first three projections as well as the average RMS error for the full 50 projection simulation when the CED was applied with a SD of 17 pixels. Table 3.20 shows the difference in the IC parameters calculated by the HC method using the estimated $(\widetilde{\varphi}, \widetilde{s})$ compared to the GT IC parameters for all 50 projection images. Figure 3.25 displays a simulated image with noise and with random C-arm deformation before and after the image has been treated by the CED.

Table 3.19: Error in the angle and position of the edge detected using the **Canny edge detector and Hough transform**, compared to the theoretical edge angle and position. Noise was present and the CED used a Gaussian filter with a SD of **17 pixels**.

Projection or Average	Angle [deg]	Position [pixels]
Proj. 1	0.000	1.0
Proj. 2	0.017	20.1
Proj. 3	0.012	3.5
Avg. of all 50	0.0162	11.49

Table 3.20: Comparison of the homography calibration parameters calculated using the estimated $(\widetilde{\varphi}, \widetilde{s})$ from the **Canny edge detector and Hough transform** method, and the GT initial view IC parameters $\mathbf{K_0^{Sim}}$. A Gaussian filter with a standard deviation of **17 pixels** was applied to the 1D RT. (All units are pixels.)

Difference with K^{Sim}	K^H_{Sim} Δf	K^H_{Sim} Δu_s	K^H_{Sim} Δv_s
mean	-2.3	-3.6	-4.3
SD	25.7	18.6	17.8
max $\lvert \cdot \rvert$	66.0	58.4	48.0

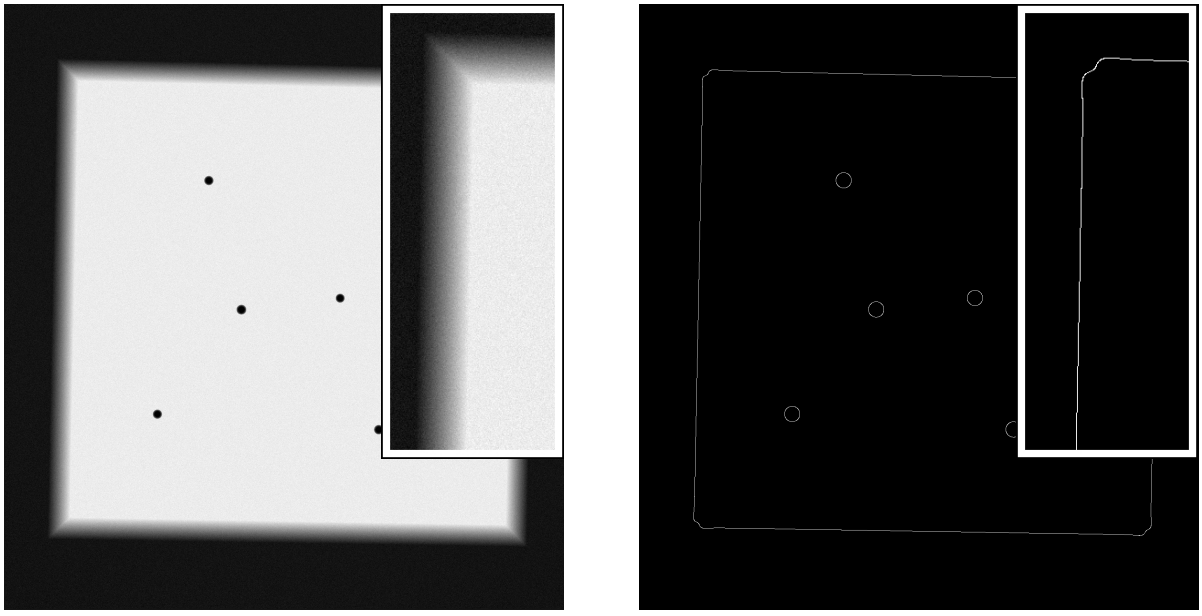

(a) Simulated image with noise

(b) Simulated image with noise after application of the CED

Figure 3.25: Example of a simulated image with noise before and after the application of the Canny edge detector.

3.3.2.6 Edge detection using the Canny edge detector and Radon transform

The Canny edge detector (CED) was implemented as in the above method with the high and low threshold values decided based on the max of the image gradient while the SD of the DGF varied from $2 - 50$ pixels.

As in the previous method there was little affect on the estimated edge angle and the IC parameters when the SD varied between $10 - 35$ pixels with the best results obtained with a SD in the range of $13 - 17$ pixels.

Table 3.21 shows the error in the estimated angle and position of the detected edge when using a CED with SD of 17 pixels compared to the GT edge angle and position. Table 3.22 gives the error of the calculated IC parameters using the estimated angle and position compared to the GT IC parameters for all 50 projections. Figure 3.26 shows the plot of the max after the application of the CED and Radon transform with and without simulated C-arm deformation.

Table 3.21: Error in the angle and position of the edge detected using the **Canny edge detector and Radon transform**, compared to the theoretical edge angle and position. Noise was present and the CED used a Gaussian filter with a SD of **17 pixels**.

Projection or Average	Angle [deg]	Position [pixels]
Proj. 1	0.000	0.1
Proj. 2	0.003	0.6
Proj. 3	0.013	0.6
Avg. of all 50	0.0068	0.77

Table 3.22: Comparison of the homography calibration parameters calculated using the estimated $(\widetilde{\varphi}, \widetilde{s})$ from the **Canny edge detector and Radon transform** method, and the ground-truth initial view IC parameters $\mathbf{K_0^{Sim}}$. A Gaussian filter with a standard deviation of **17 pixels** was applied to the 1D RT. (All units are pixels.)

Difference with K^{Sim}	K^H_{Sim} Δf	K^H_{Sim} Δu_s	K^H_{Sim} Δv_s
mean	-1.9	-0.6	1.1
SD	1.8	8.0	7.6
max $\lvert \cdot \rvert$	5.0	30.4	19.2

3.3.2.7 Derivative of a Gaussian filter after the Radon transform - Canny filter type approach

To mimic the CED method of edge detection, the derivative of a Gaussian filter with a large standard deviation was applied to the 1D RT and the maximum was found. As in both of the previous CED implementations the method was repeated with a SD of the DGF applied to the 1D RT between $10 - 21$ pixels to find the best SD and best result. The result did not change drastically when using a SD between 13 and 21 pixels, with the best result obtained between 15 and 18 pixels. Tables 3.23 & 3.24 show the error relative to the GT of the estimated angle and position of the detected edge and the calculated IC parameters for all 50 projections when the DGF method was implemented with a SD of 17 pixels.

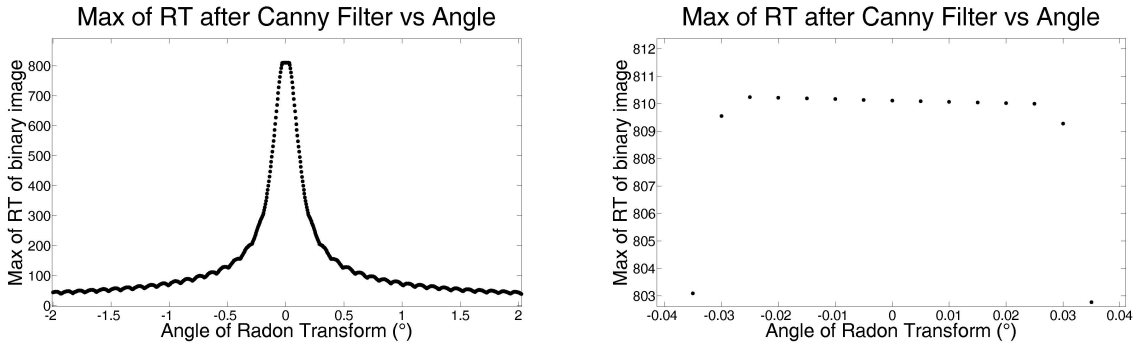

(a) Max of the CED and Radon transform without simulated C-arm deformation $\varphi = 0^o$

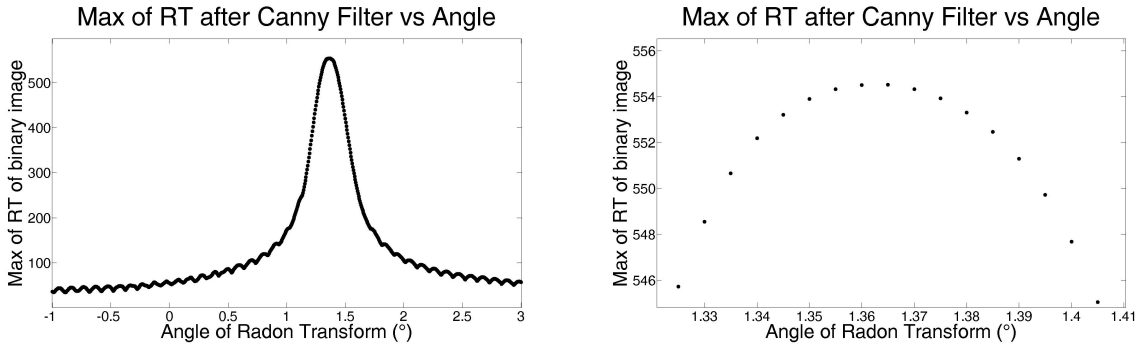

(b) Max of the CED and Radon transform with simulated C-arm deformation $\varphi = -0.152^o$

Figure 3.26: Curve of the max after application of the Canny edge detector and Radon transform versus the Radon transform angle in the presence of noise. The CED employed a Gaussian filter with a SD of 17 pixels.

Table 3.23: Error in the angle and position of the edge detected using the max of **the derivative of a Gaussian filter**, compared to the theoretical edge angle and position. Noise was present and the SD of the Gaussian filter was **17 pixels**.

Projection or Average	Angle [deg]	Position [pixels]
Proj. 1	0.006	0.6
Proj. 2	0.007	0.9
Proj. 3	0.007	0.8
Avg. of all 50	0.0070	1.05

Table 3.24: Comparison of the homography calibration parameters calculated using **the derivative of a Gaussian filter** to estimate the edge angle and position, and the ground-truth initial view IC parameters $\mathbf{K_0^{Sim}}$. A Gaussian filter with a standard deviation of **17 pixels** was applied to the 1D RT. (All units are pixels.)

Difference with K^{Sim}	K^H_{Sim} Δf	K^H_{Sim} Δu_s	K^H_{Sim} Δv_s
mean	1.0	1.7	9.7
SD	2.0	9.1	9.2
max $\lvert \cdot \rvert$	4.6	45.8	37.4

3.3.3 Discussion on optimal edge detection methods

The maximum after derivative filter method was discovered to be insufficient for the determination of the edge angle and position in the presence of noise. Various GFs were used to attempt to reduce noise effects however the results were far from being adequate for edge determination purposes.

The DMF & LF slope methods were discovered to be the best methods of edge detection in simulated conditions with noise and C-arm deformation. The method of measuring the slope of a fitted line LF to the edge profile displayed a slight improvement to the method of applying a derivative filter and a mean filter DMF of specified length (see Tables 3.9 & 3.10 and Tables 3.7 & 3.8 on pages 83 and 84). However a weakness of both of these methods is that they require the input (or estimation) of the edge width and standard deviation of the GF.

The accuracy demonstrated from these results show firstly, that measuring the slope of the edge profile is the best indicator of when the edge angle, φ, can be approximated by the RT angle, θ. Secondly, the results indicate that a simple linear fit (or derivative filter) more accurately represents the data compared to a polynomial or cubic spline fitting.

From the above simulation studies predictions on the appropriate SD of the Gaussian smoothing filter and approximate edge width/line length can be inferred. The LF method showed the best result with a SD of 2 pixels and edge width of 60 pixels and therefore a low SD and a line length which is roughly the same as the width in the image (recall $w = 59$ pixels) should be used for the optimal results. In this case only a very low SD is required being as the linear fitting of the data also acts to smooth or reduce noise effects while measuring the slope of the line. Further note that the optimal line length

determined from simulation studies is slightly longer than the measured edge width in the image. Intuitively one would assume that the fitted line length must be less than or equal to the measured edge width however due to the Gaussian smoothing filter applied to the data, the edge profile is slightly extended as displayed in Fig. 3.7(page 51).

The DMF method experiences the same effect from smoothing and it follows that the MF/line length is dependent on the level of smoothing from the GF. In this case there is no linear fitting step to reduce noise and consequently the optimal SD of the GF is slightly larger than the LF method at about $4-5$ pixels. After smoothing this method measures the slope of a line between endpoints separated by the MF length. The analysis shows that the optimal accuracy is achieved when the MF length is the same length as only the linear part of the 1D RT after smoothing. Thus the slope of only the linear part of the smoothed profile is measured, and if the SD is increased the linear part decreases, refer again to Fig 3.7. As a result the appropriate MF length, l, to be used can be approximated by the following formula: $l \simeq w - 1.5 * SD$.

The polynomial fitting for the first four edge determination methods (page 85) were based on various ways of measuring the slope of the edge profile from the polynomial. These methods did not provide satisfactory results which leads to the assumption that there may be small inaccuracies in the polynomial fitting. Similarly for the last implemented method, using the R^2 correlation coefficient to estimate the angle of the edge did not produce suitable results. This could possibly be due to inaccuracies in the polynomial fitting or possibly because the method has a reduced angular sensitivity compared to the edge profile slope measurement.

The 1st Derivative of the Cubic spline fitting to estimate the edge parameters did not produce an improvement on either the LF method or the closely related DMF method (Tables 3.17 & 3.18 on page 89). This signifies that a cubic spline fitting is less accurate than either a linear fitting or a simple derivative filter. Some inaccuracies are the result of errors in the fitting of the cubic spline in the shoulder regions of the edge profile, which are displayed in Fig. 3.20(b). In spite of the inaccuracies, the results are informative and likely useful when attempting to characterize an edge profile which has severely non linear nature.

When using the Hough transform after application of the Canny edge detector (CED), a technique commonly used in the literature, edge detection failed to give acceptable results. This outcome is not surprising being as the Hough transform is a useful

but non specific technique for edge detection of all types of lines or edges which are not necessarily thick or straight edges.

Exploiting the 2nd Derivative of the 1D RT to estimate the edge angle and position further did not cause improvement, however this attempt is noteworthy because it did not require knowledge of the edge width in the image. Estimation in this case is based on the curvature of the shoulder regions, or rather, how quickly the edge profile changes from regions without much intensity change (ex. pixels measured in the image FOV just outside the collimator edge profile) to the changing intensity in the collimator edge, see Fig. 3.7 & 3.21. This method is quite unlike other methods and may simply not have the same sensitivity on the edge parameter estimation as other methods.

Estimation of the edge parameters from the 2nd derivative of the 1D RT, only requires the input of the SD of the GF which in this case does not depend on the width of the edge in the image and showed optimal performance with a GF SD of 7 pixels. When using a SD between $5-8$ pixels lead to an increase in the error on u_s and v_s of ± 2 pixels combined.

The Canny edge detector technique and DGF method are the two remaining methods which have been studied. Although these methods did not improve upon the LF and DMF methods they did produce suitable results and only required the input of the SD of the Gaussian smoothing filter.

To contrast these two methods the first method uses the Canny edge detector to apply the derivative of a 2D Gaussian filter to find the image gradient and then determines the edge angle and position using the RT on the resulting binary image (termed CFRT method for short). The 2nd, Canny type, approach first applies the Radon transform to the image to obtain a 1D profile similar to Fig. 3.7 for each RT angular increment and subsequently uses the derivative of a 1D Gaussian filter to estimate the edge position and angle.

For both the DGF and CFRT methods the SD of the GF is required which should be based on the width of the edge in the image. The analysis show that a wide range of SDs give acceptable results. In the simulation studies above the optimal SD of the GF was found to be 17 pixels, while results with a SD of between $14-27$ pixels lead to a combined increase in the error on u_s and v_s of ± 2 pixels in most cases and less than ± 5 pixels in others.

The DGF approach surprisingly does not perform better than edge detection using

the Canny filter followed by the Radon transform (CFRT) on the Canny generated binary image. This suggests that a single 1 pixel wide binary edge signal is sufficient to obtain an adequate degree of angular sensitivity with the given image noise level and simulated deformation. In addition to this, it indicates that producing a binary image of the edge signal, from the original, likely reduces noise and background affects which could cause inaccuracies. It should be noted that the max absolute errors on the IC of these methods (DGF: $\max|u_s/v_s| = 46$ pixels, Canny filter followed by the Radon transform (CFRT): $\max|u_s/v_s| = 30$ pixels) suggests that the IC methods produce some large IC mis-estimations compared to the LF or DMF methods (LF/DMF: $\max|u_s/v_s| = 18$ pixels).

3.3.3.1 Summary of optimal edge detection methods

Although the LF method requires the input of the approximate edge width, the accuracy of this method would still be an improvement over the above methods (2nd derivative of the 1D RT, DGF, and CFRT) if the edge width were known to within roughly ± 8 pixels. This limit on the edge width estimation should be easily attainable.

Given the above analysis more stringent experimentation will be performed on the LF, DGF, and CFRT methods. The LF method exhibits the best performance while the DGF method gives a simplified, possibly less error prone, analysis check and the CFRT method contrasts the results of the previous two with a technique commonly used in the literature. The edge detection approach utilizing the 2nd derivative of the 1D RT was omitted from future studies as it could be potentially error prone due to the required estimation of the GF SD and is unlikely to provide an improvement over the LF method with real data.

The root-mean square (RMS) error on the position and angle determination by the LF, DGF and CFRT methods was: $(\sigma\varphi_{\bar{RMS}},\sigma s_{\bar{RMS}})$=$(0.0045^o$,1.67 pixels$)_{LF}$, $(0.0070^o$,1.05 pixels$)_{DGF}$, $(0.0068^o$,0.77 pixels$)_{CFRT}$, whereas the edge angle and position were measured to within 0.005^o and the nearest pixel. The sensitivity experiment of subsection 3.3.1 showed that when assuming the edge determination method can determine $\widetilde{\varphi}$ and $\widetilde{s}$ to the nearest 0.005^o and pixel, the edge angle and position error should be: $(\sigma\varphi_{\bar{RMS}},\sigma s_{\bar{RMS}})$=$(0.0013^o$,0.29 pixels). The fact that this estimation accuracy is not obtained by our methods signifies that there is either a bias in the measurement or the adopted step size (0.005^o, 1) is smaller than the degree of accuracy that can be measured.

For future studies and real data evaluations the LF method would be performed using a GF filter with a SD of 2 pixels and a line length approximately the same length

as the width of the edge in the image: $l = width$. Both the DGF and CFRT methods would be performed with a SD based on the width of the edge in the image: $SD = \sqrt{width} * 2 + 2$. These should provide suitable edge detection results for edges which have similar widths and noise levels to our simulation studies.

3.4 Further Evaluations of Edge Detection

As an informative analysis the effects due to noise and C-arm deformation will be separately examined in simulation studies. Further, an analysis was performed to indicate the edge detection accuracy due to the random variation of a single C-arm deformation parameter (for example the detector tilt angle Θ), as well as the accuracy when varying two deformation parameters together. These studies can provide further insight into the edge detections reliability, deformation sensitivity, and potential sources of measurement bias. Lastly the homography intrinsic calibration (IC) results using edges in the image FOV will be compared to the homography calibration (HC) using spherical marker (implemented in chapter 2) and the gold-standard full offline calibration method.

3.4.1 Effects from noise and simulated C-arm deformation

To discover the effects on the accuracy of the edge detection and IC from added noise to simulated data the three methods of edge detection (LF, DGF, and CFRT) were implemented on the same 50 projection scan with randomly simulated C-arm deformation without added noise. Comparison of the results generated without noise but with C-arm deformation with the previous results which included both noise and randomly simulated C-arm deformation will illustrate the error of the edge detection and IC due to added noise.

Similarly a single simulated projection from the 50 projection scan was selected and replicated 50 times with noise added individually to each image before implementing the methods of edge detection. Comparing the results produced without deformation but with noise to the previous results (section 3.3.2) indicate the error related to C-arm deformation. This analysis can be performed by adding noise to projections which contain a static random level of deformation as well as projections with no deformation (ie. the collimator lines parallel to the image rows and columns).

Linear fit LF edge detection method: The evaluation without noise but with the same random deformation showed no improvement on the estimated line positions while having notable improvement on the edge angle estimation, $\sigma\varphi_{\bar{RMS}}$. The improved line angle estimation leads to an increase in the accuracy of the IC parameters relative to the GT simulation conditions. Recall that this method utilizes a linear fitting which acts to reduce noise while measuring the slope and thus in noiseless conditions there may not be a significant improvement.

Additionally, implementing the LF method with noise but without deformation the error of the estimated edge angle increases. This indicates that the edge position estimation is influenced by deformation while the edge angle estimation is influenced by noise.

Table 3.25: Comparison of edge detection and intrinsic calibration accuracy using the **linear fit method (LF)** with and without simulated deformation and noise.

Trial	Avg. RMS error (from GT)		IC parameter error (from GT)		
	[degrees]	[pixels]	[pixels]		
	$\sigma\varphi_{\bar{RMS}}$	$\sigma s_{\bar{RMS}}$	σ_f	σ_{u_s}	σ_{v_s}
with deformation with noise	0.0045	1.67	2.0	4.0	4.5
with deformation only	0.0030	1.67	1.5	3.0	3.7
with noise - no def.	0.0062	1.14	0.0	5.9	5.6
with noise - static def.	0.0066	1.71	0.6	3.2	4.8

When simulated images are generated with noise but without deformation, hence the collimator edges are parallel to the image rows and columns there is a decrease in the accuracy of the IC. This is due to a decrease in the angular sensitivity described in subsection 3.1.1.2(page 53) together with a slight bias due to the image background. These factors are also the cause of the mean error between the homography IC and the GT IC seen in Table 3.10.

When static deformation is present the collimator edges are no longer parallel to the image rows and columns and thus the sensitivity is no longer affected leading to a more accurate IC estimation. This IC estimation demonstrates that fluctuating noise affects the angle estimation which affects the IC. The fact that the angle estimation of the simulated projection with static deformation contains more error than the estimated angle with both noise and random deformation signifies that there is a reduced accuracy for this particular level of static deformation relative to the average accuracy of the randomly deformed simulated projections.

Derivative of a Gaussian filter: When using the DGF method to implement edge detection the evaluation with deformation (no noise) only displays a slight improvement over the evaluation with both deformation and noise which signifies that the method is resilient in the presence of noise and generally IC parameter error arises from simulated deformation. This is further illustrated by a significant improvement in the IC parameter estimation in the presence of noise without deformation or with static deformation. IC results with noise but without deformation are less accurate than the results with static deformation likely also due to the decreased sensitivity in the edge detection when the collimator edges are parallel to the rows and columns of the image. Lastly note that the edge angle estimation, $\sigma\varphi_{\bar{RMS}}$, with static deformation appears to be less accurate than the estimation without deformation yet the IC parameters have improved accuracy. This is potentially caused by an angle estimation error which is consistent for all the projections with static deformation (opposed to a random angle estimation error without deformation) which can lead to an accurate IC parameter estimation. (This affect is further described in subsection 3.3.1.1.)

Table 3.26: Comparison of edge detection and intrinsic calibration (IC) accuracy using the **derivative of a Gaussian filter method (DGF)** with and without simulated deformation and noise.

Trial	Avg. RMS error (from GT)		IC parameter error (from GT)		
	[degrees]	[pixels]	[pixels]		
	$\sigma\varphi_{\bar{RMS}}$	$\sigma s_{\bar{RMS}}$	σ_f	σ_{u_s}	σ_{v_s}
with deformation with noise	0.0070	1.05	2.0	9.1	9.2
with deformation only	0.0051	1.05	1.6	9.0	7.0
with noise - no def.	0.0065	0.64	0.0	5.8	5.6
with noise - static def.	0.0076	0.91	0.6	3.4	4.2

Canny edge detector & Radon transform: This method of edge detection implements the CED and the Radon transform to perform edge detection in an approach commonly used in the literature. This approach is similar to the DGF method and behaves similarly. The analysis without noise but with deformation again showed a slight improvement compared to the same analysis with noise which indicates the method is resilient in the presence of noise. The edge detection and IC estimation in the presence of noise and with static deformation displays a significant improvement in accuracy compared to the evaluations with both noise and random deformation. However contrary to

the previous methods, when edge detection was completed with noise and without deformation, hence the collimator edges are parallel to the rows and columns of the image, the evaluations exhibit perfect estimation of the IC parameters. This indicates that this method likely still has the reduced sensitivity when the edges are parallel to the image rows or columns, however the Canny edge detector removes any noise or background affects which may bias the edge parameter estimates.

Table 3.27: Comparison of edge detection and intrinsic calibration (IC) accuracy using the **Canny edge detector and Radon transform (CFRT)** with and without simulated deformation and noise.

Trial	Avg. RMS error (from GT)		IC parameter error (from GT)		
	[degrees]	[pixels]	[pixels]		
	$\sigma\bar{\varphi}_{RMS}$	$\sigma\bar{s}_{RMS}$	σ_f	σ_{u_s}	σ_{v_s}
with deformation with noise	0.0068	0.77	1.8	8.0	7.6
with deformation only	0.0062	0.78	1.6	8.1	6.3
with noise - no def.	0.0000	0.10	0.0	0.0	0.0
with noise - static def.	0.0053	0.79	0.9	4.8	3.6

3.4.2 Single and multiple deformation parameter variation

Similar to the study previously achieved in subsection 2.2.4, page 38, the effects of single and multiple parameter deformation were studied. The evaluations show the sensitivity (or IC error relative to the GT, σ_f, σ_{u_s}, σ_{v_s}) of each individual deformation parameter and the error interdependence of multiple parameters ((z_d, x_d), (z_d, Φ), (z_d, η), (x_d, Θ), (x_d, Φ), (x_d, η), (Θ, Φ)). Ten projections were simulated for each analysis. In both exercises, the deformation parameters were free to vary randomly with the same conditions as the previous evaluations (see subsection 1.2.3.3, page 23). Further the average RMS error on the edge angle and position estimation are examined to observe the edge detection sensitivity to single and multiple parameter deformation. To illustrate the error affects due only to single and multiple parameter deformation the edge detection procedure was completed in the absence of noise.

This investigation proved to be fairly important as it reveals some edge detection and IC sensitivities specifically with the Canny filter followed by the Radon transform (CFRT) method. First we will examine the typical edge detection and IC errors which would result from single parameter deformation. Following this the edge detection and

IC estimation results of single and multiple parameter deformation will be compared between the three methods under investigation.

The Φ detector rotation is around the u-axis of the detector which causes the collimator edges aligned with the v-axis to rotate in the image resulting in the alteration of the v_s and f intrinsic parameters. Conversely, the Θ rotation is about the v-axis causing rotation in the collimator edges aligned with the u-axis and alteration of the u_s and f parameters. On the other hand, the η rotation is in the plane of the detector which, alone, has no affect on the intrinsic parameters, though that is not to say it does not have an affect on the angle of the edges in the image.

The Φ and Θ detector rotation can affect both the edge position and angle in the image and, as it may be apparent, the displacement of the detector (or z_d, y_d, x_d deformation) would only affect the edge positions.

The error of the edge angle/position and IC estimation due to deformation of each parameter individually is presented in the top portion of Tables 3.28, 3.29, & 3.30 for the LF, DGF, and CFRT methods respectively. The focal length estimate is dependent on the edge positions in the image which vary for all but η deformation, thus the data exhibits focal length estimation error with any deformation except η. Being as the focal length is on the order of 6,000 pixels, generally errors in the estimation of the position or angle of the edges have a significant effect on σ_f, although it relates to less than a 0.05% error which is considered minuscule for 3D reconstruction purposes. Further note that given the typical level of sensitivity on the edge angle estimation compared to the edge position, the Φ and Θ angular deformation produces substantially more error in the u_s and v_s parameters than any other deformation. This further validates that the IC is more sensitive to the edge angle estimation than the position.

Multiple parameter deformation is presented in the bottom of Tables 3.28, 3.29, & 3.30 for all three methods. Ordinarily the edge angle and position estimation error was approximately the same as the single parameter variations, except when both Φ and Θ varied together which caused an increase in the $\sigma\varphi_{\bar{RMS}}$ error similar to the addition of both errors from the individual deformation. Roughly the multiple parameter error is simply the addition of the contributions from the single parameter deformation errors, though there are some clear exceptions which will be discussed further. It is important to note that all three methods were applied to the same simulated images.

The LF method displays an improvement in the edge angle determination accuracy compared to the DGF and CFRT methods while it shows decreased edge position accuracy. In most cases this leads to an improved u_s and v_s estimation with a slight increase in the focal length estimation error.

Table 3.28: The **linear fit method (LF)** edge detection and IC estimation error resulting from single and multiple parameter random deformation, in the absence of noise. Note the dash signifies 0.0 pixel error, or 0.000 degree error in $\sigma\bar{\varphi}_{RMS}$. (All units are pixels except where otherwise indicated).

Deformation Parameter	z_d	y_d	x_d	Φ	Θ	η	-
σ_f	3.7	1.5	1.5	1.5	1.1	-	
σ_{u_s}	-	0.2	-	-	3.2	-	
σ_{v_s}	-	-	0.2	3.2	-	-	
$\sigma\bar{\varphi}_{RMS}$	-	-	-	0.0018^o	0.0017^o	0.0020^o	
$\sigma\bar{s}_{RMS}$	1.4	1.3	1.3	1.3	1.3	1.2	
Deformation Parameters	(z_d, x_d)	(z_d, Φ)	(z_d, η)	(x_d, Θ)	(x_d, Φ)	(x_d, η)	(Θ, Φ)
σ_f	1.1	2.2	3.0	1.5	1.8	1.9	1.3
σ_{u_s}	-	-	-	3.5	-	1.4	3.6
σ_{v_s}	0.2	3.3	-	0.1	4.6	0.2	4.3
$\sigma\bar{\varphi}_{RMS}$	-	0.0015^o	0.0016^o	0.0018^o	0.0026^o	0.0014^o	0.0030^o
$\sigma\bar{s}_{RMS}$	1.4	1.3	1.5	1.4	1.3	1.5	1.4

The DGF method obtains a stable and reliable edge determination and IC estimation with slightly more error than the LF method. This is not the case when considering the performance of the CFRT method which revealed large estimation errors. Though the observed errors may appear to be single random error estimations in the small sample size of ten projections, this actually is not the case. The errors are due to mis-estimations of at least two projection images and often four or more smaller mis-estimated projections. Further these mis-estimations are not attributed to statistically rare large random fluctuations in the deformation parameters but rather the inability of the Canny edge detector Radon transform method to accurately measure very small edge angles close to 0^o or 90^o. This is a direct result of the image binary conversion by the CED and the lack of sensitivity when measuring the angle of a line/edge which is parallel to the image columns or rows, as described in subsection 3.1.1.2 on page 53. When the edge signal is either a single straight line or even a broken line spread out over two rows or columns accurate measurement of the edge angle is not possible using the binary image generated by the Canny edge detector.

When all six parameters, which specify the detector position and orientation vary randomly at the same time (as in the evaluations of subsection 3.3.2) it rarely occurs

Table 3.29: The **derivative of a Gaussian filter method (DGF)** edge detection and IC estimation error resulting from single and multiple parameter random deformation, in the absence of noise. Note the dash signifies 0.0 pixel error, or 0.000 degree error in $\sigma\bar{\varphi_{RMS}}$. (All units are pixels except where otherwise indicated).

Deformation Parameter	z_d	y_d	x_d	Φ	Θ	η	-
σ_f	3.0	1.2	1.2	1.6	1.2	-	
σ_{u_s}	-	0.2	-	-	5.6	-	
σ_{v_s}	-	-	0.2	4.0	-	-	
$\sigma\bar{\varphi_{RMS}}$	-	-	-	0.0024^o	0.0026^o	0.0019^o	
$\sigma\bar{s_{RMS}}$	0.7	0.7	0.7	0.7	0.7	0.6	
Deformation Parameters	(z_d, x_d)	(z_d, Φ)	(z_d, η)	(x_d, Θ)	(x_d, Φ)	(x_d, η)	(Θ, Φ)
σ_f	2.3	1.6	3.9	1.5	1.4	2.0	1.9
σ_{u_s}	-	-	0.2	5.4	-	0.1	4.7
σ_{v_s}	0.2	4.3	0.2	0.2	4.9	0.2	4.2
$\sigma\bar{\varphi_{RMS}}$	-	0.0016^o	0.0016^o	0.0023^o	0.0028^o	0.0014^o	0.0034^o
$\sigma\bar{s_{RMS}}$	0.7	0.8	0.8	0.9	0.7	0.8	0.8

that the edge angle is parallel (or close to parallel) with the image columns or rows and therefore large deviations from the GT seldom occur as they have in the above Table 3.30. This does however account for the somewhat larger values of the maximum deviation from the GT (Table 3.22 page 92).

This lack of sensitivity is only present in the CFRT edge determination and does not occur in either the LF or DGF methods.

3.4.3 Comparison of intrinsic calibration from edges, spherical markers, and the gold-standard calibration method

The last evaluation compares the IC accuracy when using the linear fit (LF) method with simulated edges in the FOV, the standard spherical marker phantom implemented in chapter 2, and also the gold-standard full offline calibration method using six spherical markers at the isocenter. The evaluation was completed with noise and random C-arm deformation as in Table 3.10 (page 84) & Table 2.4 (page 38). Both homography calibration (HC) methods used the single view IC provided by the GT simulation

Table 3.30: The **Canny edge detector and Radon transform (CFRT)** edge detection and IC estimation error resulting from single and multiple parameter random deformation, in the absence of noise. Note the dash signifies 0.0 pixel error, or 0.000 degree error in $\sigma\bar{\varphi_{RMS}}$. (All units are pixels except where otherwise indicated).

Deformation Parameter	z_d	y_d	x_d	Φ	Θ	η	-
σ_f	4.2	1.2	1.2	1.2	1.2	-	
σ_{u_s}	2.1	0.2	-	1.0	7.5	-	
σ_{v_s}	-	-	0.2	23.0	-	-	
$\sigma\bar{\varphi_{RMS}}$	0.0005^o	-	-	0.0084^o	0.0035^o	0.0047^o	
$\sigma\bar{s_{RMS}}$	0.4	0.2	0.2	0.3	0.3	0.1	
Deformation Parameters	(z_d, x_d)	(z_d, Φ)	(z_d, η)	(x_d, Θ)	(x_d, Φ)	(x_d, η)	(Θ, Φ)
σ_f	2.5	2.1	2.8	2.1	1.1	2.0	1.9
σ_{u_s}	-	-	-	5.6	-	3.1	17.2
σ_{v_s}	2.0	31.6	-	1.0	16.9	2.3	7.9
$\sigma\bar{\varphi_{RMS}}$	0.0004^o	0.0123^o	0.0049^o	0.0043^o	0.0073^o	0.0026^o	0.0103^o
$\sigma\bar{s_{RMS}}$	0.4	0.3	0.4	0.4	0.3	0.4	0.3

conditions, $\mathbf{K}_0^{Sim}$.

It is clear that the HC from the linear fit edge detection method does not provide an improvement on the HC simply using four spherical markers attached to the x-ray source. Furthermore, the spherical marker IC result (with image noise and C-arm deformation) performs better than the IC from the LF edge detection method in the absence of noise (but with deformation) or on a static deformed series of images with noise (Table 3.25). This indicates that the process of edge detection at any level of C-arm deformation or image noise can not be accomplished with the same sensitivity as the localization of spherical markers in an image by a simple gray level center of mass weighting.

Nevertheless, the LF IC method demonstrates slightly better results than the full offline gold-standard calibration method. However as discussed in section 2.3, the validity of the comparison of only the intrinsic parameters from a full calibration method to a process which only performs IC is in question.

Table 3.31: Comparison of the IC accuracy of the homography calibration using edges in the FOV (Linear fit method) (left), the HC using spherical markers (as seen in Table 2.4) (center), and the gold-standard full offline calibration method (right). The max absolute value, SD, and mean values were found for the difference between the estimated and ground-truth IC parameters of 50 projections simulated with random C-arm deformation and noise. (All units are pixels.)

Difference with K^{Sim}	K^H_{LF} Δf	K^H_{LF} Δu_s	K^H_{LF} Δv_s	K^H_M Δf	K^H_M Δu_s	K^H_M Δv_s	K^{GS} Δf	K^{GS} Δu_s	K^{GS} Δv_s
mean	3.5	-7.2	9.6	0.0	-0.9	-0.7	-0.3	-0.0	-0.4
STD	2.0	4.0	4.5	0.1	1.1	1.0	6.7	5.2	5.8
max $\lvert\cdot\rvert$	7.5	16.6	18.4	0.3	3.4	2.7	22.0	13.8	20.3

3.4.4 Discussion on further evaluations of edge detection

The further evaluations presented in this section illustrated the affects of noise and deformation on the methods of edge detection, revealed the limited sensitivity of the Canny filter followed by the Radon transform (CFRT) method, and compared the homography IC from lines to the IC from markers and the gold-standard method.

3.4.4.1 The effects from image noise and C-arm deformation of all six parameters on the performance of the edge detection methods

To recap the results from this analysis, the edge position estimation is only sensitive to C-arm deformation while the edge angle estimation is particularly sensitive to noise and less sensitive to C-arm deformation. The LF edge detection method and IC is most sensitive to noise while the DGF and CFRT methods are more sensitive to C-arm deformation.

A close inspection of the edge estimation error from the DGF and CFRT methods reveals that their errors are inherently due to different factors despite their very similar operation, behaviour, and errors. Though we have made the statement that deformation is the primary cause of error in the CFRT edge detection, the single/multi parameter deformation study showed that it is in fact the lack of deformation which causes these errors - edge errors close to $0^o/90^o$ can not be properly estimated. On the other hand, the estimation errors associated with the DGF method seem to result from an overall estimation error or bias in all edges of all projections with, although, a small number (~ 2) severely mis-estimated edges causing the larger maximum deviations.

If the image quality was degraded and contained more noise the LF method accuracy would also be degraded but this could be compensated for by increasing the SD of the GF used for smoothing before the linear fit. On the other hand, the DGF and CFRT methods would likely perform equally as well if the image noise was increased with perhaps a slight decrease in the accuracy of the DGF method.

Overall this analysis shows that the LF edge detection method would most likely out perform both the DGF and CFRT methods in any feasible situation.

3.4.4.2 Single and multiple parameter C-arm deformation

This study confirmed that the LF method is a more reliable means of estimating the edge angle/position and the IC parameters during simulated C-arm deformation without added image noise. This study also exposed the CFRT methods inability to estimate the edge angle (and thus the IC parameters) when the true edge angle was close to 0^o or 90^o (parallel to the image columns or rows).

When the simulated projection produces edges which are exactly at $0^o/90^o$ (hence no C-arm deformation) the possible edge angle sensitivity is decreased as described in subsection 3.1.1.2, page 53. The LF and DGF methods have a loss of sensitivity and also a slight bias in the angle estimation due to the image background and noise. The CFRT method has the same decreased sensitivity but because the Canny edge detector converts the image (edge and background) to a binary image of the edge structure, the resulting image has no background or noise bias so the edge angle estimation without C-arm deformation is perfect (as shown in Table 3.30). When the edge angle is orientated close to $0^o/90^o$ (within $\approx \pm 0.110^o$) but not exactly parallel to the rows or columns the limited sensitivity of the LF and DGF methods is significantly improved. Alternatively, the binary signal produced by the CED can not distinguish this small angular deviation and can not accurately determine the edge angle. Thus the LF and DGF methods can more accurately estimate the edge angle in this situation.

The next section will implement these methods of edge determination on real images of the x-ray tube collimator in the field of view (FOV) during a C-arm scan. This analysis will depict how likely it would be for the collimator edges to be close to $0^o/90^o$ during a real C-arm scan, and thus how likely errors due to the loss of angular sensitivity near $0^o/90^o$ are to occur.

3.4.4.3 Comparison of homography calibration method with edges, spherical markers and with the gold-standard calibration

This analysis illustrated that the detection of spherical markers in an image by a gray level center of mass weighting has significantly more accuracy than the detection of edges in an image. This conclusion should not be a surprise given the sub-pixel accuracy of the center of mass weighting. If instead we consider the equivalent situation of performing the HC using the intersection points of the four imaged edges we can compare the possible accuracy of these intersection points with the measured accuracy of the four imaged spherical markers. The measured RMS error of the projection of the four spherical markers (with image noise and C-arm deformation) was on average 0.027 pixels. Noting that the simulated edges in the image are approximately 1100 pixels in length, we can calculate the angular sensitivity required to achieve an RMS error of 0.027 pixels on the intersection point of two lines.

Assuming the position, s, of one line, and both the position and angle of the second line are perfectly estimated then an angular error of $\arctan(0.027/550) = 0.0028^o$ would produce the same RMS error obtained when imaging spherical markers. If both the positions of the two lines were known but the angles were not an angular error of $\arctan(\frac{0.027}{\sqrt{2}}/550) = 0.0020^o$ would produce the 0.027 pixel RMS error of the intersection point. From our simulations studies the minimum angular RMS error which has been achieved is only 0.0045^o which quite obviously could not produce the same level of accuracy as when imaging spherical markers.

However, the IC accuracy obtained should still be sufficient for a good reconstruction image quality, and give similar 3D image quality as the gold-standard full offline calibration method. This hypothesis will be tested in chapter 4 with simulation studies.

3.5 Edge Detection Applied to C-arm Projections of the X-ray Tube Collimator

An analysis of edge detection was completed using images of the x-ray tube collimator from our C-arm during a 190^o scan. This evaluation will assess the reliability of edge detection by the three aforementioned methods (LF, DGF, CFRT) applied to real data as well as the potential sensitivities and problems which can affect the reliability of edge detection with real projection image data which may contain an object in the FOV.

In order for IC of the C-arm to be possible after edge detection a method of initial

view IC must be implemented. Additionally, when using real data, the estimated IC lacks a suitable means of comparison since there is no GT C-arm calibration to compare our results to. The full offline gold-standard calibration is possible (by imaging the gold-standard phantom described in subsection 1.2.1.4 page 14) however, as previously discussed, the full calibration method yields a significant amount of IC parameter variability and consequently any IC comparison with this method is not viable.

3.5.1 Edge detection with real data

The edge detection methods can be analyzed using real data by doing a comparison of the trend or change in the measured edge angles and positions of the four edges from each of the three methods. The trend in the measured edge parameters is shown as a function of the C-arm orbital angle. Furthermore, this evaluation can be achieved on multiple scans of the collimator in the FOV.

There are a few notable differences between edge detection using real data and simulation data. First of all, there may be an object in the field of view. If this object is homogeneous and expanding the image FOV the edge detection accuracy may be decreased being as the edge profile would overlap with the object and the change in intensity between the collimator (region without photons passing) and the image FOV/object (the max photon flux) would be reduced. Essentially this would result in a decreased edge profile width - which could be accounted for - and an increase in the image noise if the object is any less than perfectly homogeneous. On the other hand, if the object is not homogeneous and contains edge like structures, these structures may be misinterpreted as the edge, although this is unlikely unless the object edge structure was in the correct position and had a similar edge width or intensity gradient as the real edges. In the event that the object has edge structure which is close to the collimator edge position in the image, the object edge structure and the real collimator edge may overlap causing an incorrect edge estimation.

Secondly, real edge detection is different than what has been accomplished for simulation studies because the widths of the real collimator edges are different. This has been discussed in subsection 1.2.1.1 on page 11 where the widths have been approximately measured to be: $L = 64 \pm 5$pixels, $R = 27 \pm 2$pixels, $T = 42 \pm 2$pixels, $B = 55 \pm 5$pixels. Thus, as was the case with simulation studies, the measured edge widths are used in order for the detection of each edge.

The DGF and CFRT methods utilized a SD of the Gaussian filter which is based on the width of each edge: $SD = \sqrt{width} * 2 + 2$. The LF method implements a Gaussian

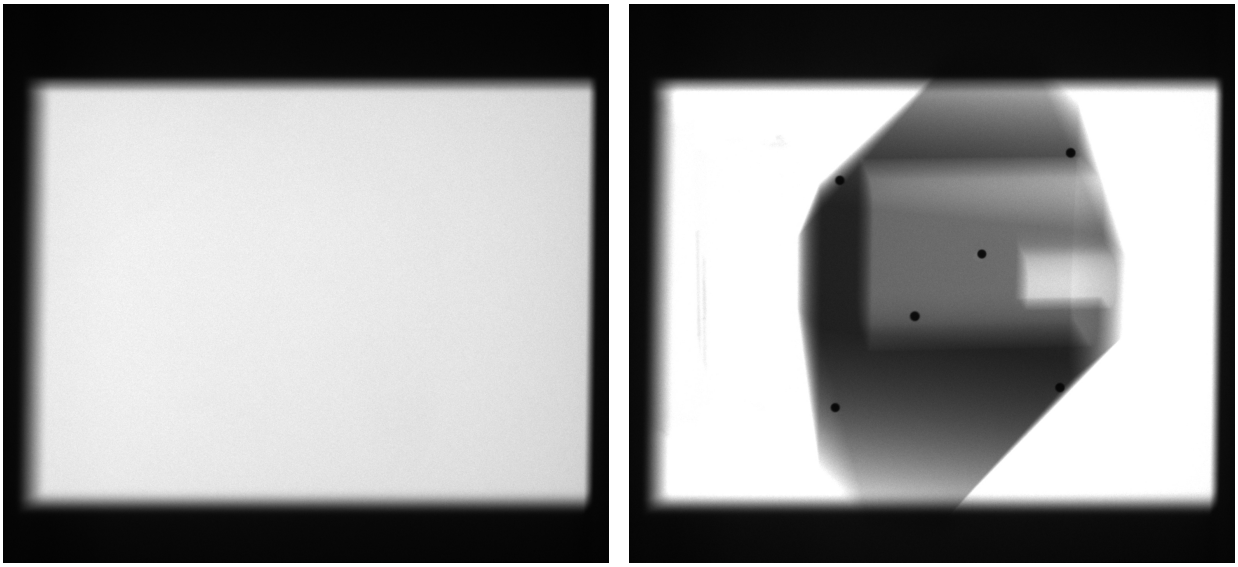

(a) Projection image of collimator (no object)

(b) Projection image of collimator with the gold-standard phantom positioned at the isocenter

Figure 3.27: Projection images from two C-arm scans of the x-ray tube collimator for edge detection. The projection images were obtained at a projection angle of 174^o of the 190^o scan.

smoothing filter with a SD of 2 pixels (the SD is the same for both real and simulation data because the noise level is approximately the same), and a fitted line with the same length as the width of each edge.

3.5.2 Results of edge detection on real data

Edge detection was implemented by each of the three edge detection methods on two C-arm scans. The first scan had nothing in the FOV (no object), while the second scan contained the gold-standard phantom positioned at the isocenter and located at the center of the FOV (with object). A single projection image from each of these scans can be seen in Fig. 3.27.

3.5.2.1 Edge detection method comparison

The best way to observe the differences between the implemented edge detection methods is to plot the positions and angles determined by each method as a function of projection

angle (or C-arm orbital angle). Fig. 3.28 shows the estimated positions and angles for the right and top edges by the three edge detection methods: LF, DGF, CFRT. Only the right and top edges are shown from scan 1 as the left and bottom edges gave similar results. Additionally, scan 2 exhibited the same behaviour between the edge detection methods as scan 1.

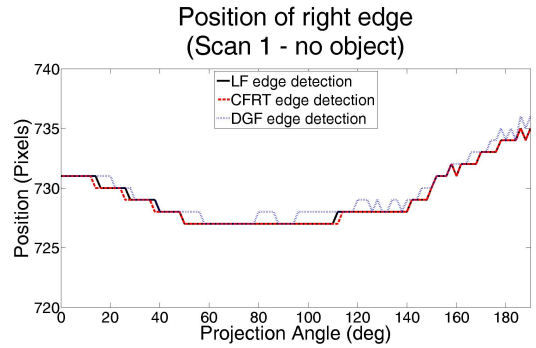

(a) Estimated position of right edge

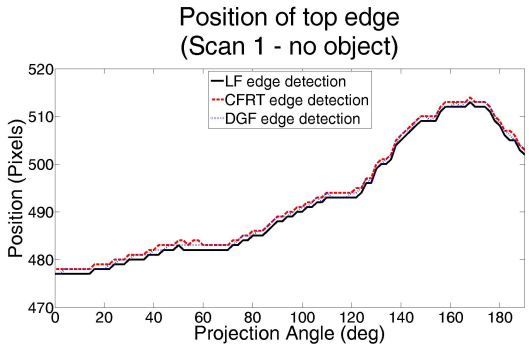

(b) Estimated position of top edge

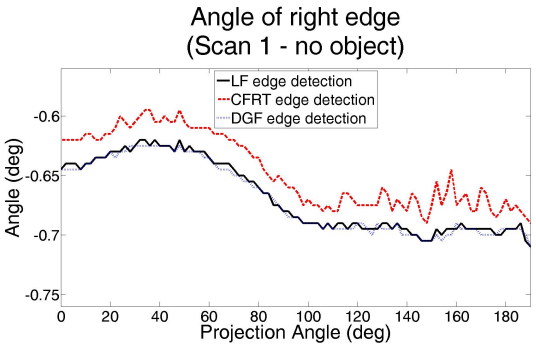

(c) Estimated angle of right edge

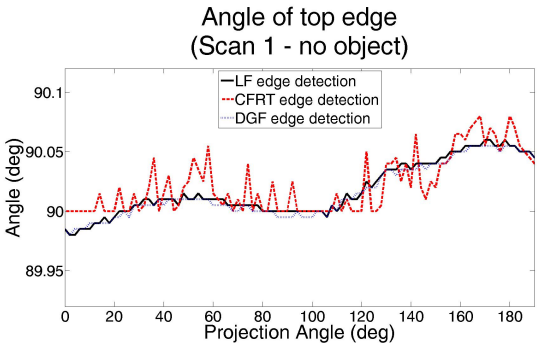

(d) Estimated angle of top edge

Figure 3.28: Estimated positions and angles of right and top edges by the three edge detection methods. The C-arm scan used for this analysis only contains the collimator edges without an object in the FOV.

The estimated positions by the three methods were very similar for all edges. The variation of the top and bottom edge positions was significantly greater than the variation of the right and left edges. This difference is also quite apparent in the projection images of the scan (also depicted in Fig. 1.2 on page 12). Recall that the axis of orbital rotation is the u-axis (or the vertical image axis), thus the top and bottom edge movement relates to detector displacement which is parallel to the orbital rotation axis.

The right and top angle estimation depict some striking differences in estimation

between the CFRT method and the DGF/LF methods. With the left and right angle estimations there is a significant angular offset between the estimations by the CFRT and DGF/LF methods. Further, the CFRT edge angle estimations display substantial variations compared to the DGF/LF methods, specifically with the top and bottom edges (as shown in Fig. 3.28(d)) but also with the left and right edges. The true edge angles are not known, therefore we can't conclusively say which method estimations are closer to the true values. Although, the CFRT method has considerably more angular variation which is unlikely to represent the true angle estimation given that the variation appears to be noise like, in which a low pass filter would show a clear trend in the data. Additionally, the fact that the LF and DGF methods closely agree indicates they are most likely more accurate than the CFRT method.

From this evaluation and the previous simulation evaluations we can make the assumption that the LF method of edge detection is the more accurate and reliable method.

3.5.2.2 Typical edge angle and position variation

The LF method of edge detection was implemented on scan 1 (no object) and the mean, standard deviation, range, min and max edge angles and positions are displayed in Table 3.32. This assessment demonstrates the typical change in the estimated edge positions and angles with real data which gives an indication of the level of C-arm deformation experienced.

Table 3.32: Angle and position estimations of the edges of the x-ray tube collimator of a typical C-arm scan. The linear fit method of edge detection was implemented on a C-arm scan with no object in the field of view.

Value	Angle [deg]				Position [pixel]			
	Left	Right	Bottom	Top	Left	Right	Bottom	Top
mean	-1.03	-0.67	89.97	90.02	-707.9	729.2	-587.4	491.8
SD	0.0209	0.0301	0.0111	0.0228	4.4	2.3	13.1	12.2
Min	-1.06	-0.71	89.945	89.98	-713	727	-604	477
Max	-0.975	-0.62	89.99	90.06	-698	735	-565	513
range	0.085	0.09	0.045	0.08	15	8	39	36

As stated previously this evaluation shows that the range of the top/bottom edge positions is larger than the left/right edges most likely due to a greater C-arm detector displacement in this direction. Also the position of the right edge has a slightly smaller

range than the left edge, possibly due to the differences in the edge widths ($L = 64 \pm$ 5pixels, $R = 27 \pm 2$pixels) which could decrease the accuracy of the left edge position estimate or improve the accuracy of the right position estimate.

Observe that the top/bottom edges are orientated very close to 0^o while the left/right edges are orientated at an angle. Three of the four edge angles have a similar range, roughly 0.09^o while the bottom angle has about half this range. Consequently the SD of the bottom angle is about half of the other edge angle SD. Lastly note that the right position angle has a similar range as the left and top edge angles while exhibiting a larger SD, indicating it has a larger estimation error. This larger angular estimation error is likely also due to the smaller edge width.

From these evaluations it can be inferred that a larger edge width allows for a better edge angle estimation while at the same time reducing the edge position precision. And vise versa, a smaller edge width increases the precision of the position estimate while decreasing the precision of the edge angle estimate.

Additionally, the above table shows the typical range and standard deviation of the edge angles estimates: range $\approx 0.09^o$ and SD $\approx 0.025^o$. Assuming there is no in plane detector rotation, η, this would correspond to a detector rotation in Φ or Θ of: Θ/Φ range $\approx 1.01^o$ and Θ/Φ SD $\approx 0.28^o$. The detector displacement (y_d,x_d) can be presumed to be: range ≈ 7.3 mm and SD ≈ 2.4 mm based on the estimated edge positions assuming there is no detector rotation, which is clearly not the case however the correction would be small.

3.5.2.3 Edge detection comparison between scans

The next edge detection investigation implements the LF method to show the trend in all edge angles and positions of both scans. Fig. 3.29 displays the edge positions of all four edges in both scans, while Fig. 3.30 displays the angles.

Both scans were acquired in the same orbital rotation direction and both starting at 0^o however the angle and position parameters are not necessarily the same in both scans. The angles and positions of the edges would be the same if the C-arm scan geometry was exactly the same (hence reproducible geometry). Observations of the C-arm system during orbital rotation and image acquisition reveal that the source and detector undergo a significant amount of motion due to C-arm system vibration. We can assume that this vibration is non reproducible and therefore the source and detector geometry are not reproducible. In any case, to attempt to discern the level of reproducibility between these two scans likely may not be valid being as there is an object in the FOV in scan 2

which could slightly alter the image and edge detection process. C-arm reproducibility will not be discussed further in this section.

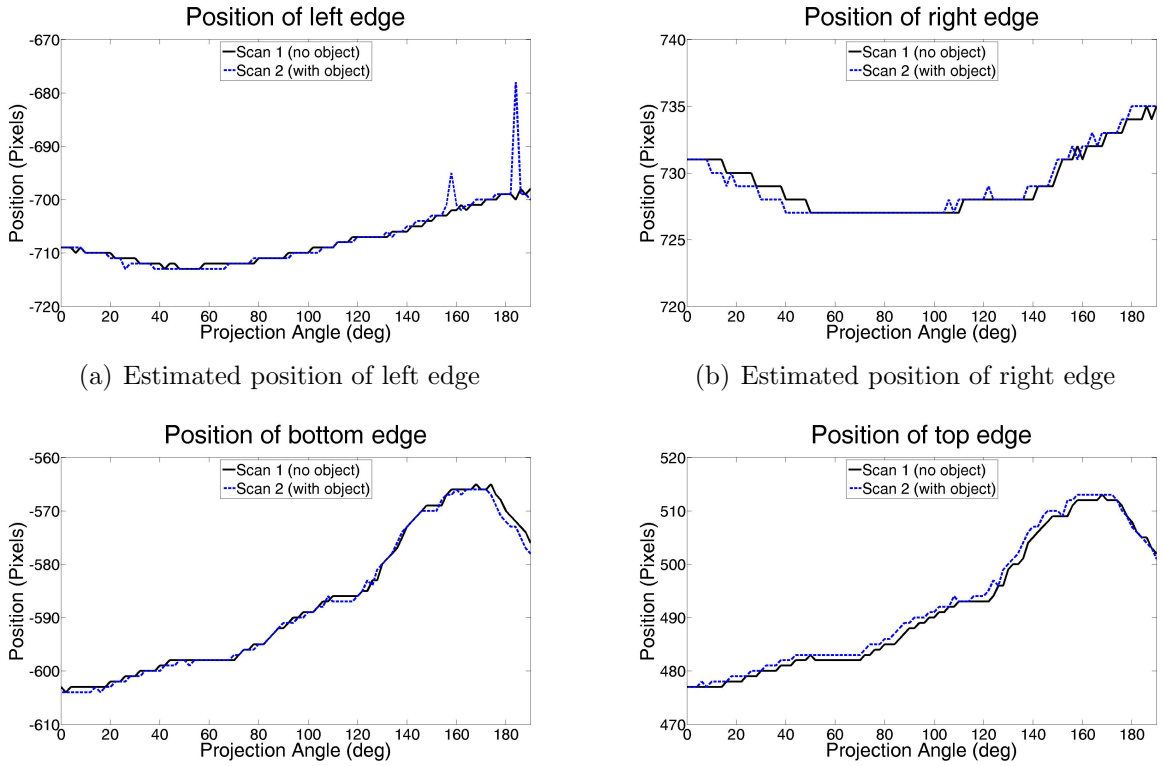

(a) Estimated position of left edge

(b) Estimated position of right edge

(c) Estimated position of bottom edge

(d) Estimated position of top edge

Figure 3.29: Estimated edge positions by the linear fit method of edge detection in two scans (with and without an object).

Again it can be noted that generally the left and right edge positions vary by a significantly smaller margin compared to the top and bottom edges. Additionally the figures show that the behaviour of both the top and bottom, and left and right edges, are almost the same, hence during the scan, as the bottom edge moves up on the image the top edge follows simultaneously, and vise versa.

Fig. 3.29(a) and Fig. 3.30 display substantial differences in the edge position and angle estimations between the two scans. These differences are certainly due to the object in the FOV in the second scan. All three edge detection methods give very similar estimations of the edge angles and positions of scan 2. The position and angle mis-estimations of the left and right edges are visible in the image and understandable. They are the result of the patient/object table being imaged laterally causing a vertical

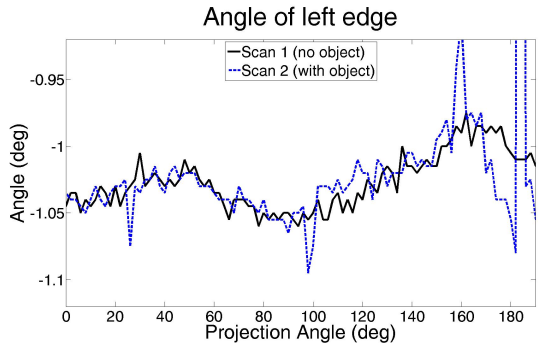

(a) Estimated angle of left edge

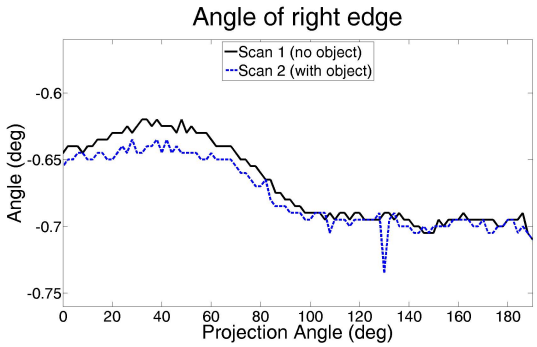

(b) Estimated angle of right edge

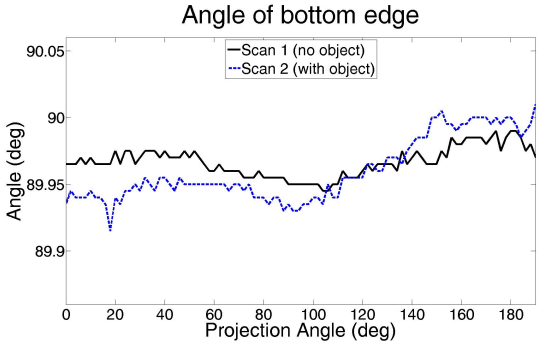

(c) Estimated angle of bottom edge

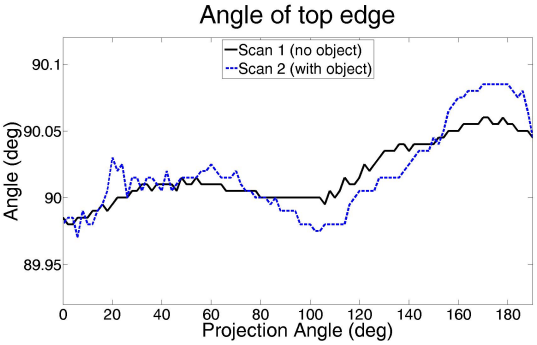

(d) Estimated angle of top edge

Figure 3.30: Estimated edge angles by the linear fit method of edge detection in two scans (with and without an object)

line or edge in the image which may overlap with the left or right edge in the image. This affect is visible in the left edge causing the mis-estimation at projection (or orbital) angle 158^o and 184^o. An example is shown in Fig. 3.31 at the projection angle 184^o. At this angle the projection of the table completely overlaps the left edge causing the enormous mis-estimations in the position and angle of the edge. When the orbital angle is 186^o the projection of the table no longer overlaps the image edge and the edge position is correctly estimated while a small error remains in the estimation of the edge angle.

The edge detection method requires the approximate edge width for a proper estimation of the edge position and angle. As explained above when the field of view contains a homogeneous object - or in the case of the left edge of Fig. 3.31(b) the projection of the non-transparent patient table - it acts to reduce the change in intensity from the minimum (no photon flux through the collimator) to the maximum flux through the field of view and object. This results in a reduced edge width and consequently a

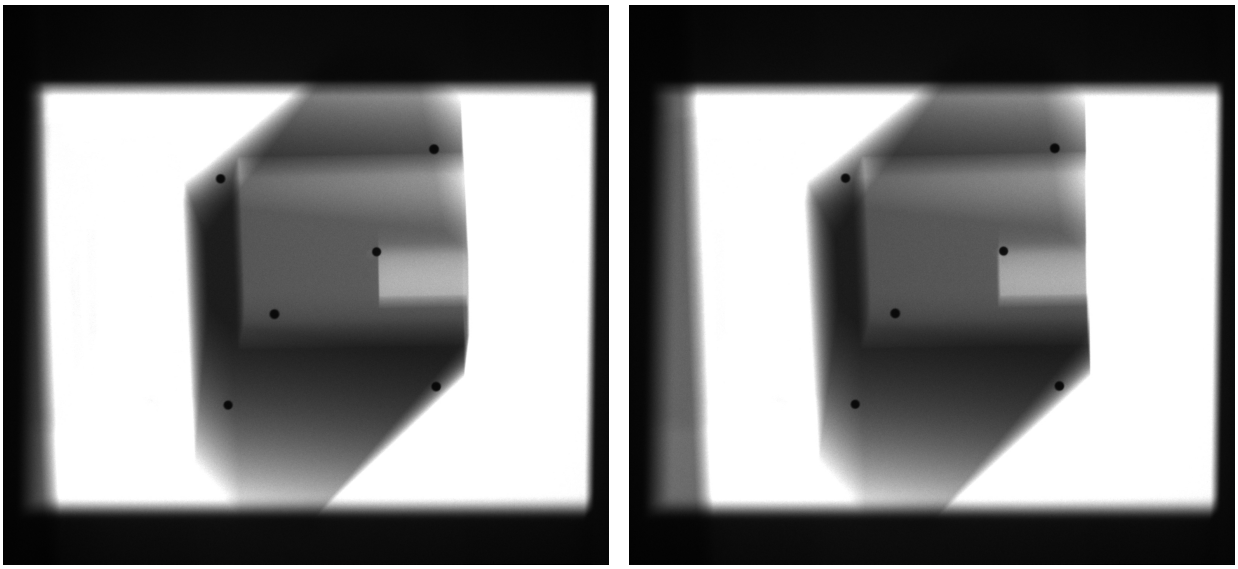

(a) Projection image of collimator edge and table edge overlapping (184^o)

(b) Projection image of collimator edge without overlapping table edge (186^o)

Figure 3.31: Two projection images from the C-arm scan of the collimator and gold-standard phantom. Edge detection fails for the left edge in (a) due to the edge of the table (imaged laterally) overlapping with the collimator edge at 184^o. There is no edge detection problem in (b) at angle 186^o.

bias or error in the edge angle estimation.

The bottom and top edge angle estimations of scan 2, Fig. 3.30(c,d), exhibit a small bias relative to scan 1 for most of the projection images of the scan. This bias is also due to the object in the field of view. As seen in Fig. 3.31 the gold-standard phantom overlaps with the top and bottom edges, but only partially. The position in which the phantom overlaps with the edge creates and dictates the bias of the edge angle estimation. This affect can be seen in the bias of the bottom edge angle which is underestimated from 0^o to $\approx 100^o$ and overestimated from $\approx 140^o$ to 190^o (Fig. 3.30(c)). As seen in Fig. 3.31 at 184^o the gold-standard phantom primarily overlaps the bottom edge along the left half of the edge. As the C-arm rotates the position of the phantom rotates in the image such that when the orbital angle is between $\approx 100^o$ to $\approx 140^o$ the phantom overlaps the bottom edge along the middle of the edge (creating no bias/error), and when the orbital angle is less than $\approx 100^o$ the phantom overlap region is along the right half of the bottom edge. This causes the edge angle estimation bias which is underestimated until $\approx 100^o$ and over estimated after $\approx 140^o$.

3.5.3 Discussion regarding edge detection in real C-arm images

These results have indicated that the edge angle (and occasionally position) estimation is highly sensitive to the object in the field of view. In some cases an edge in the image is overlapped by some edge like structure from the object in the image causing severe mis-estimations of the edge angle and position. Furthermore, a predictable bias in the edge angle estimation would occur when the object in the FOV overlaps only a partial edge region. In most situations these errors cannot be accounted for or corrected easily. If, on the other hand, the object spans the FOV and is more or less homogeneous the edge angle and position errors most likely can be accounted for and corrected.

When comparing the methods of edge detection applied to a scan of the collimator edges without an object in the FOV, the position estimations of all three methods closely agreed with each other. However, when comparing the angle estimations of the three methods the CFRT method significantly differed from the LF and DGF methods and also showed greater variation in the angular estimation.

Additionally, when comparing the bias and errors in the edge angle estimations of scan 2 from the three edge detection methods, all three methods show very similar trends and angle mis-estimations. However in almost every case the DGF and CFRT methods generate a greater angular deviation from scan 1 due to the bias and mis-estimations of the edge angles and positions. These results are a strong indication that the LF

method provides more accurate edge detection in real data conditions than the other two methods.

It should be noted that in this analysis the collimator was closed much more than required in order for the edges to be visible in every deformed projection image. The collimator position can be adjusted such that the edge structure is always visible in the image while the field of view is maximized. In doing so the errors due to the object in the FOV could be reduced.

The real data assessment has shown that the standard angular range is on the order of 0.09^o and that the edges may have some inherent rotation (for example the left edge is orientated at -1.06 ± 0.05) while other edges (the top and bottom) may be nearly parallel to the image columns or rows. This indicates that the edge angle estimation of real data could likely suffer from the reduced sensitivity when the edge is nearly 0^o or 90^o and therefore the Canny filter followed by the Radon transform method could not be sufficient for real data edge angle estimation.

Chapter 4

Application to 3D Image Reconstruction

Résumé du Chapitre 4 en Français

Dans ce chapitre, nous appliquons nos méthodes de calibration intrinsèque afin de reconstruire en 3D un objet à partir de projections radiographiques multiples (à calibrer).

Nous avons simulé des projections radiographiques 2D incluant le collimateurs, du bruit, des déformations de C-arm et bien sûr la projection d'un objet 3D à reconstruire.

Nous avons comparé les reconstructions à partir

- des paramètres de calibration connus
- des paramètres de calibration estimés par une méthode globale de calibration standard utilisant une mire 3D dans le champs de vue
- des paramètres intrinsèques estimés par notre méthode de calibration utilisant la détection de la projection du collimateur dans les projections et des paramètres extrinsèque exacts
- des paramètres intrinsèques estimés par notre méthode de calibration utilisant la détection de la projection du collimateur dans les projections et de paramètres extrinsèques estimés par par une méthode globale de calibration standard utilisant une mire 3D dans le champs de vue.

Les résultats confirment que notre méthode est très sensible à l'estimation des paramètres de calibration dans l'image de référence. Nous analysons les erreurs et proposons des méthodes pour améliorer les résultats.

Summary

This chapter evaluates our method of edge detection and homography intrinsic calibration (IC) through 3D image reconstruction (IR) of 2D simulated projection images. Simulated projection images of the collimator in the field of view and the six marker gold-standard calibration phantom positioned at the isocenter provide a means for evaluating our intrinsic calibration method compared to both the gold-standard full offline calibration method along with the ground-truth (GT) simulation conditions. Image reconstruction methods are provided by the Reconstruction toolkit (RTK) [Rit *et al.* 2014]. In this work 3D IR is only utilized for evaluation purposes, we do not attempt to improve on reconstruction methods or consider the accuracy of IR methods.

4.1 Introduction to Cone-Beam Image Reconstruction Methods

In our case image reconstruction involves the process of finding the 3D object function which corresponds to the 2D acquired projection data. The objective is to associate every 2D image pixel to the correct 3D voxels. This is analogous to finding the ray or line between the source and detector through 3D space for every projection image. Thus, the precise geometry of the source and detector relative to the 3D world coordinate frame must be known.

The projection operator $\mathbf{P}$ defines the projection of the object function, f, to generate the data d:

$$\begin{array}{rccc} \mathbf{P}: & \mathbb{R}^n & \longrightarrow & \mathbb{R}^{n-1} \\ & \text{object} & \longrightarrow & \text{data} \\ & f & \longrightarrow & d \end{array}$$

This is an inverse problem as the data, d, has been measured and we must find f such that $\mathbf{P}f = d$. If $\mathbf{P}$ is linear than its inverse operator, the back-projection operator, $\mathbf{P}^{\#}$ plays an important role:

$$\begin{array}{rccc} \mathbf{P}^{\#}: & \text{data} & \longrightarrow & \text{object} \\ & d & \longrightarrow & f \end{array}$$

Cone-beam 3D IR techniques generally fall into two categories: analytic and iterative. Iterative techniques perform IR by a process of repetitive operations of back-projection, $\mathbf{P}^{\#}$, (smearing the 2D detector measurements across the 3D volume) and forward-projection, $\mathbf{P}$, (re-projection of these smeared values onto the detector plane) [Noo 1998].

Thus IR is reduced to a simple, but computationally intensive, optimization problem. This optimization type approach is generally considered a non-exact or approximate method while analytic methods are considered exact as they use direct analytic formulas (based on some assumptions) to compute the solution. However analytic methods require that the projection imaging trajectory satisfies the Tuy condition [Tuy 1983]. In 3D, the object function f at point r can be reconstructed if any plane passing in the vicinity of r crosses the trajectory (non-tangentially). Usually the C-arm trajectory is circular which generally does not satisfy the Tuy condition except for the plane containing the circular trajectory. Cone-beam analytic reconstruction is most often accomplished by a filtered back-projection (FBP) algorithm introduced by Feldkamp, Davis, and Kress FDK in 1984 [Feldkamp *et al.* 1984]. This 3D cone-beam algorithm is an approximated algorithm adapted from the 2D situation.

This work deals with 3D image reconstruction from cone-beam x-ray projections rotating with a near circular trajectory around 360^o by using the Feldkamp Davis & Kress cone-beam reconstruction (FDK) algorithm from RTK. The following gives a brief introduction to IR and the FDK algorithm. For further details refer to Chapter 3 of Kak and Slaney [Kak & Slaney 1988] or [Turbell 2001, Noo 1998].

The principles of cone-beam 3D reconstruction can be best introduced by describing the concepts of 2D parallel beam and 2D fan-beam reconstruction then expanding this to the 3D cone-beam problem.

In the monochromatic and simplified case, x-ray projection images measure the intensity, I, or flux of x-rays through the object which interact with the detector:

$$I = I_0 \exp\left(- \int_0^L f(l)\, \mathrm{d}l \right)$$

where $f(l)$ represents the attenuation characteristics of the object function along the line L. When considering multiple projections around a 2D planar object, this object function can be expressed as $f(x, y)$ on the 2D plane containing the object.

After image processing the object function can be represented as the line integral from the detector to the source through the object:

$$- \ln \frac{I}{I_0} = \int_0^L f(x, y)\, \mathrm{d}l$$

Recall that this image processing step is not required for our simulation generated

data as we directly generate the $-\ln \frac{I}{I_0}$ projection image (and pixel values) using the Radon transform.

In the parallel beam imaging situation with a 2D planar object the projection of this object at an angle θ is illustrated in Fig. 4.1.

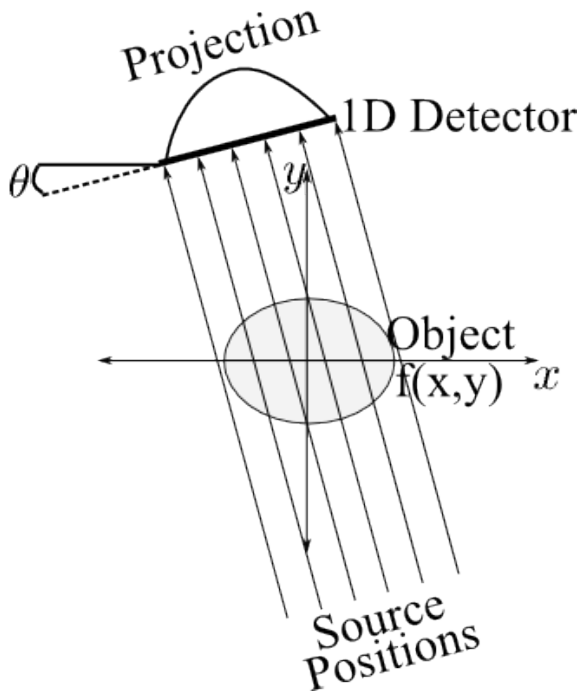

Figure 4.1: An illustration of a 2D object function being imaged on a 1D detector by multiple parallel x-ray beams.

The line integral along the line L can also be expressed using the Dirac delta distribution in x and y and it follows that the projection at angle θ ($\mathbf{P}_\theta$) is:

$$d(\theta, s) \stackrel{\text{def}}{=} \mathbf{P}_\theta f(s)$$

$$d(\theta, s) = \iint_{\mathbb{R}^2} f(x, y)\delta(s - x\cos\theta - y\sin\theta)\,\mathrm{d}x\,\mathrm{d}y \tag{4.1}$$

This formula may be familiar to the reader as it is simply the 2D Radon transform also described in Chapter 3.

The 2D parallel projection of the object function at angle θ in the space domain produces measurements along a single line at angle θ in the frequency domain. If the

detector contained an infinite number of pixels and an infinite number of projections were obtained between $0^o \leq \theta < 180^o$, then every line in the frequency domain would be measured allowing for a perfect reconstruction of the 2D object using the 2D inverse Fourier transform. This is the principle which the foundations of image reconstruction are based on called the Fourier slice theorem [Kak & Slaney 1988]. The theorem states that the Fourier transform of a projection at angle θ, $\widehat{\mathbf{P}_\theta f}(\sigma)$, is equal to the 2D Fourier transform of the object function $\widehat{f}(\sigma\vec{\theta})$:

$$\widehat{\mathbf{P}_\theta f}(\sigma) = \widehat{f}(\sigma\vec{\theta}) \qquad \text{with} \qquad \vec{\theta} = \begin{pmatrix} \cos\theta \\ \sin\theta \end{pmatrix} \tag{4.2}$$

Clearly, sampling over infinite angles using a detector with infinite pixels is not possible so in reality the entire frequency domain is not sampled and the reconstructed image becomes an approximation. Sampling around N_θ angles (between $0^o \leq \theta < 180^o$) with a detector with N_s pixels produces N_θ lines with N_s points measured along each line in the frequency domain, Fig. 4.2. As shown in Fig. 4.2(b) this results in an under-sampling of the high frequency components of the image relative to the low frequency components - hence more points measured closer to the frequency domain origin. This can be compensated for by filtering (usually using a ramp filter) in the frequency domain or equivalently in the space domain. Back-projection of this filtered projection data generates the reconstruction of the 2D object function. Thus we have introduced the notion of filtered back-projection for 2D IR.

The FBP algorithm is directly derived from the inverse Fourier transform of the Fourier slice theorem Eq. (4.2):

$$f(x,y) = \iint_{\mathbb{R}^2} \widehat{f}(\xi_1,\xi_2) e^{+2i\pi(\xi_1 x + \xi_2 y)} \, \mathrm{d}\xi_1 \, \mathrm{d}\xi_2$$

$$f(x,y) = \int_0^\pi \int_{\mathbb{R}} \widehat{f}(\sigma\vec{\theta})|\sigma| e^{+2i\pi\sigma(x\cos\theta + y\sin\theta)} \, \mathrm{d}\sigma \, \mathrm{d}\theta$$

$$f(x,y) = \int_0^\pi \left(\int_{\mathbb{R}} \widehat{\mathbf{P}_\theta f}(\sigma)|\sigma| e^{+2i\pi\sigma\vec{\theta}\cdot\binom{x}{y}} \, \mathrm{d}\sigma \right) \mathrm{d}\theta \tag{4.3}$$

The parallel beam geometry previously discussed utilizes a pencil beam x-ray source which translates to irradiate each pixel individually, and at all projection angles sampled.

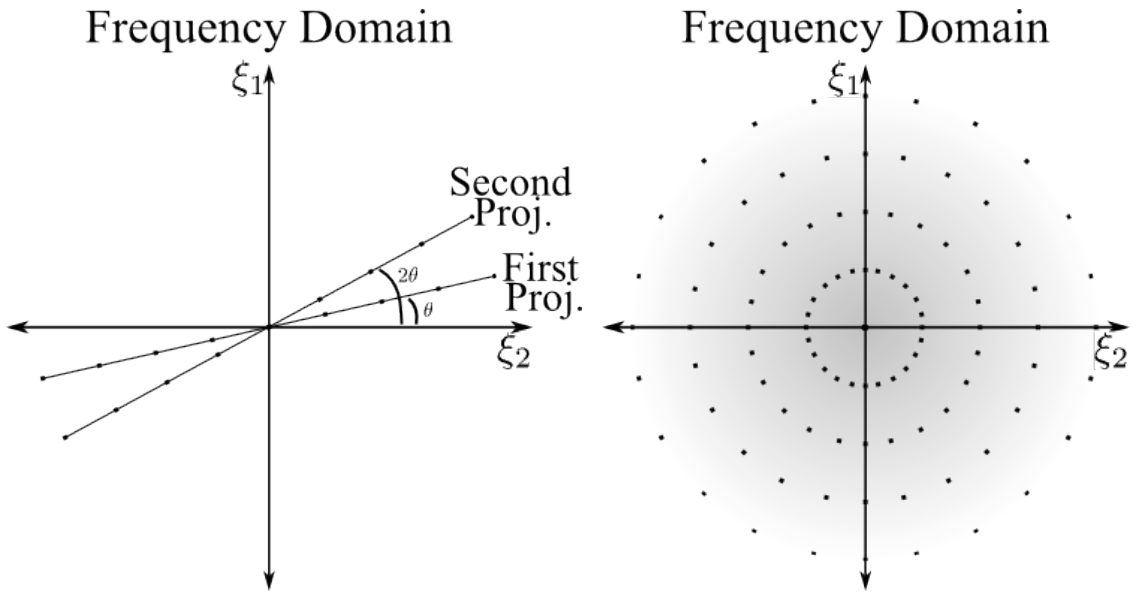

(a) Depiction of frequency domain measurments from the first two projections

(b) Depiction of the frequency domain measurements of a full scan

Figure 4.2: A depiction of the frequency domain sampling from multiple parallel beam measurements. The 1D projection images of a 2D object at the angles θ and 2θ on a 1D detector with 11 pixels provides 11 measurements at each angle in the frequency domain displayed as dots. A full scan provides the measurements shown in (b), in which the low frequency domain is oversampled relative to the high frequency domain - hence there are more measurements at lower values of ξ_1 and ξ_2 in the frequency domain.

This situation requires a considerable amount of acquisition time. A more feasible acquisition method adopts a fan-beam x-ray source to irradiate all pixels of the detector at each projection angle, Fig. 4.3(a). Fan-beam projection data can simply be re-sorted into equivalent parallel projection data along different angles at which the projection data is sampled. This is shown in Fig. 4.3 where the pixel measured by the dashed line in (a) is equivalent to a parallel projection at the projection angle of Fig. 4.3(b).

With this implementation, however, the parallel projections generated by the rotating fan-beam data acquisition are not uniformly sampled throughout the object function. The FBP in fan-beam geometry is obtained from the FBP in parallel beam geometry (Eq. (4.3)) by the change of variables from (θ, s) to the variables of the fan-beam geometry.

To extend this to 3D object reconstruction, a simple 2D fan beam approach can

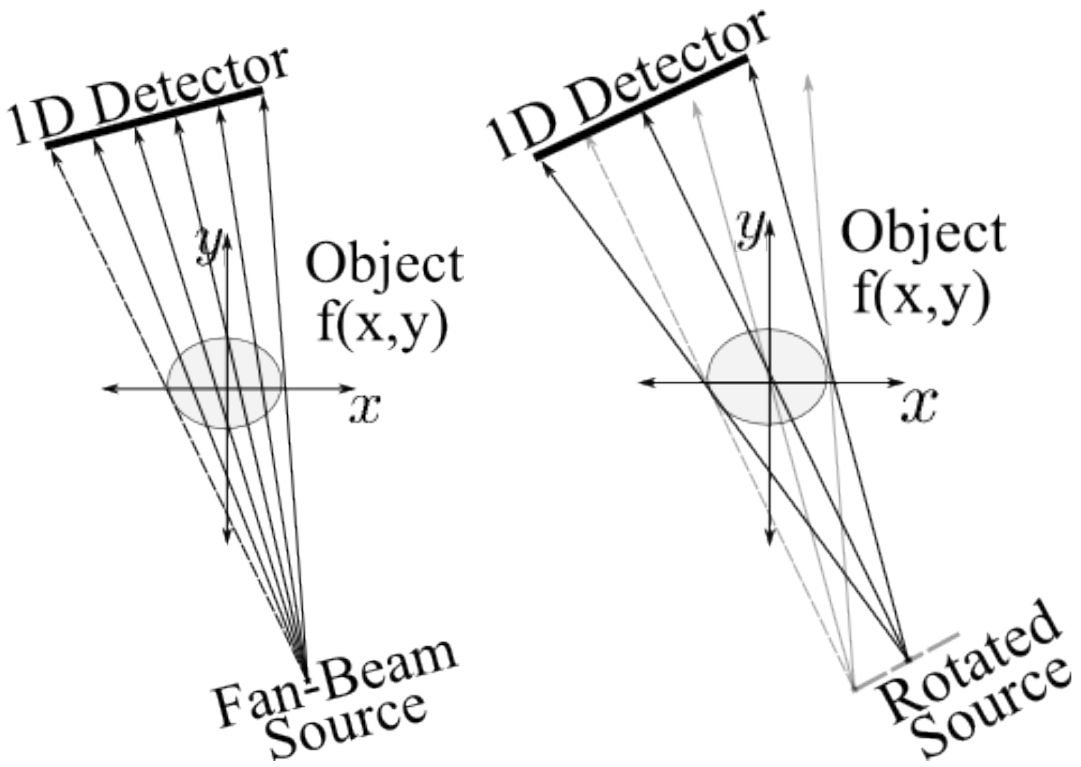

(a) The fan-beam projection of a 2D object onto a 1D detector.

(b) Depiction of how fan-beam data can be re-sorted into parallel beam data.

Figure 4.3: Each ray from a fan beam projection can be re-sorted into an equivalent parallel projection ray obtained at a different orbital angle. The ray represented by a dashed line in (a) is analogous to a parallel projection ray at the rotated source position of (b).

be implemented in which multiple fan beam projections are acquired around the object but also along the z axis. The 3D object function $f(x, y, z)$ can be obtained as multiple slices from 2D fan-beam reconstructions in z. This requires multiple rotations around the object function, one for each 2D reconstructed slice.

Instead, using a cone-beam x-ray source (shown in Fig. 4.4) which projects the 3D object onto a 2D detector as the source rotates along a circular trajectory generates all the data required to reconstruct the 3D object with a single rotation. As mentioned earlier this would be performed by the FDK cone-beam filtered back-projection algorithm. The filtering of the projection data is achieved along the 2D planes parallel to the source trajectory as if the rows of the 2D projection data were obtained from a rotating

fan-beam source which acquires each row of the 2D projection individually. However, the FDK algorithm uses adapted weights to take into account the cone-beam geometry during the back-projection from the 2D detector to the source [Feldkamp *et al.* 1984].

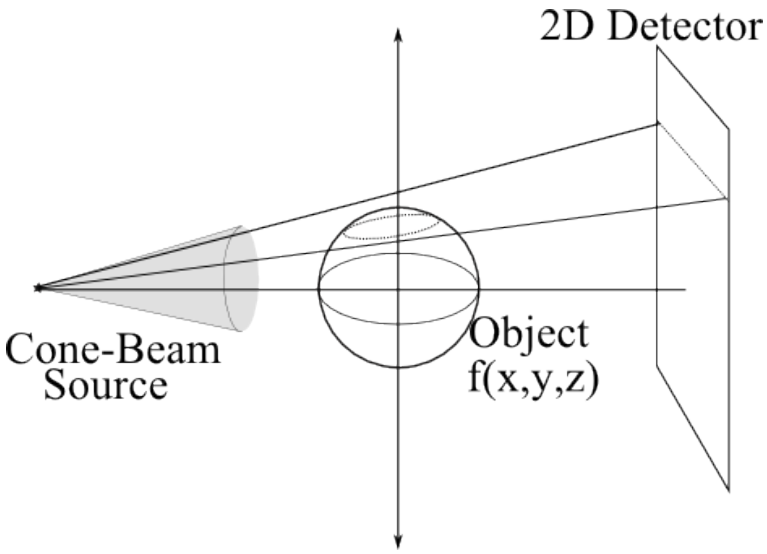

Figure 4.4: An illustration of a cone-beam projection of a 3D object composed of a series of fan-beam 1D projections across the 2D detector.

The FDK algorithm provides an approximate solution for 3D cone-beam image reconstruction (IR) acquired with a circular trajectory which does not satisfy the Tuy condition. Nevertheless, the FDK algorithm has been shown to provide an acceptable level of error in both real and simulation experiments [Feldkamp *et al.* 1984, Turbell 2001].

4.2 Conditions and Implementation of Reconstruction

The evaluations in this study comprise of 29 simulated C-arm scans, each with 101 projection images with added image noise and obtained with randomly varying C-arm geometry. The simulated images contained both the collimator edges and the six markers of the gold-standard calibration phantom. The objective is to perform image reconstruction from each of the 29 scans using either known or estimated geometric calibration parameters. Therefore, each geometric calibration will generate a different reconstructed image for each scan which can be compared individually to evaluate the calibration

Table 4.1: The maximum and standard deviation of the varied C-arm deformation parameters for simulation experiments.

Calibration Parameter	z_d [mm]	y_d [mm]	x_d [mm]	Φ [deg]	Θ [deg]	η [deg]	t_z [mm]	t_y [mm]	t_x [mm]
SD	3.45	3.20	3.20	0.60	0.60	0.20	0.30	1.65	1.65
Maximum	±13.8	±12.8	±12.8	±2.4	±2.4	±0.8	±1.2	±6.6	±6.6

method. Additionally, the reconstructed images from all 29 simulated scans can provide a statistical measure of the calibration accuracy. The simulated collimator edges would be removed from the projection images before reconstruction while the six marker gold-standard phantom (displayed in Fig. 1.8 on page 26) provide the object to be reconstructed and evaluated.

Simulated C-arm deformation

The C-arm source and detector geometry are described by nine geometric parameters: the source position (t_z, t_y, t_z), the detector position relative to the source (z_d, y_d, x_d), and the detector orientation (Φ, Θ, η). In these experiments the simulated C-arm deformation varied randomly but not by the same level as the simulation experiments previously described. In the earlier evaluations of the IC method randomly simulated C-arm deformation was described by a Gaussian with a standard deviation (SD) based on the max deformation measured by Daly et al. [Daly *et al.* 2008]. The real data analysis in Chapter 3 revealed that C-arm deformation was far less than what was originally simulated. Additionally, Chapter 3 demonstrated that collimator edge detection has a decreased sensitivity when the edges were close to $0^o/90^o$. Consequently, for these reconstruction evaluations the standard deviation of the randomly simulated deformation parameters was roughly estimated as $1/4^{th}$ of the maximum deformation measured by Daly et al. (ie. $1/4^{th}$ of the previously simulated deformation). The standard deviation and maximum allowed deformation can be seen in Table 4.1 for each of the nine geometric parameters.

With these conditions the variations in the simulated edge angles and positions would still be significantly greater (by an order of magnitude) than the measured variations in real data conditions. Further, the simulated edges would often be close to $0^o/90^o$ with these conditions.

Implementation of Reconstructions

Projection images for reconstruction were simulated while the source and detector rotated a full 360^o around the isocenter. For all reconstruction experiments 101 projection images were simulated. The large number of projection images and the full 360^o orbital rotation would reduce the inaccuracies that could result from the reconstruction algorithm due to insufficient data. The purpose of this experimentation is not to evaluate the accuracy of the reconstruction algorithm, but the accuracy of the calibration method.

The Reconstruction toolkit (RTK) [Rit *et al.* 2014] package was implemented to provide four reconstructions for each of the 29 simulated C-arm scans. As previously mentioned, the RTK package performs cone-beam FDK reconstruction with a near planar source trajectory, ie. the source positions lie on or close to a plane.

For each scan the four reconstructed images are generated using:

1. the ground-truth (GT) C-arm intrinsic and extrinsic calibration
2. estimated IC from the detection of the collimator edges and the exact GT extrinsic calibration
3. the estimated IC (as in #2) and the erroneous extrinsic calibration parameters containing errors to replicate the level of estimation error which would occur due to a four marker extrinsic calibration method
4. the estimated intrinsic and extrinsic parameters from the gold-standard full calibration method

The estimated IC is accomplished using the linear fit (LF) method of edge detection. Recall that the homography IC method must be initialized with a known or measured single view IC. As discussed in Chapter 2 (section 2.3) an accurate means of measuring a single view IC should be possible in real data conditions using our gold-standard calibration phantom. Chapter 2 also describes the affect which occurs if there is an error in the reference IC, the error gets transfered to the estimated intrinsic calibration parameters of every projection of a scan as a static bias. This affect can occur if there is error on the reference IC or, equivalently, if there is an error on the estimated edge angles or position in the reference image for which the IC parameters are measured.

In #2 the extrinsic calibration parameters are provided by the known GT conditions while in #3 the GT extrinsic parameters are perturbated by a uniform random error in order to imitate the expected error due to a simple (and common) extrinsic calibration method using a four marker planar phantom at the isocenter of the C-arm system. This four marker extrinsic calibration technique is a common approach in the field of

computer vision and could be easily adopted for our imaging system. This extrinsic calibration has been implemented and investigated by Burnier in [Burnier 2015]. This work presents the typical error on the estimated source or optical center location and the estimated orientation of the camera system in the world coordinate frame. From this work we can extrapolate a typical extrinsic calibration error for our imaging system based on the imaging conditions of both cameras. However, note that in our application the estimated IC is produced separately from the extrinsic calibration hence their is no coupling procedure to ensure the two calibrations are coherent and possibly reduce the associated errors of both calibrations.

The gold-standard full offline calibration is implemented as in [Mennessier *et al.* 2009, Spencer *et al.* 2012] using the imaged locations of the six spherical markers. Though this is an offline method in which the calibration is computed before scanning the object to be reconstructed, it will be employed as an online method in our investigation - the calibration is determined for the same scan which is to be reconstructed. Further, the object to be reconstructed is in fact the same object which provides the calibration, the six markers of the gold-standard phantom.

Reconstruction Evaluation

The IR using the GT calibration, #1, will show the reconstruction errors due to the projection image noise and the reconstruction algorithm. Comparison of this this GT reconstructed image with the IR using the GT extrinsic calibration with the estimated IC from the detection of the collimator edges will give an analysis of the collimator edge detection IC affect on the reconstructed image quality. The full gold-standard calibration, #4, demonstrates the reconstructed image quality obtained from a typical C-arm calibration method. The full calibration IR quality can be exhibited from this gold-standard IR compared with the reconstructed images using the collimator estimated IC and an extrinsic calibration with a typical level of error expected when using a four marker calibration technique, #3.

All four calibration methods will be evaluated based on their accuracy in reconstructing six spherical markers which span the 3D volume. To provide a quantitative measure of the quality of the IRs the imaged markers can be fit to a 3D ellipsoid. From the reconstructed images a threshold can be applied to remove all noise like voxels which are less than roughly $1/4$ of the 3D image max. From this thresholded image the six markers can be located and all voxels in the 3D vicinity of the marker can be used to provide a ellipsoid fitting of the marker. This ellipsoid fitting will produce the 3D position of the center of the ellipsoid along with the three radii of the object. The ratio

of the minimum radii over the maximum expresses the similarity between the fitted ellipsoid and a sphere. If the IR quality is exceptional the ellipsoid fitting will produce a sphere like object (with a radii ratio of ~ 1) at the correct position, while if the IR is poor an elongated ellipsoid will result with significantly different radii and possibly at an incorrect position.

4.3 Results of Image Reconstruction

The rendered reconstructed images contained $256 \times 256 \times 256$ square voxels, with a voxel side length of 0.5 mm, which is roughly 2.7 pixels on the projection image. Four reconstructed images were generated for each of the 29 scans. Each reconstructed image contains three pairs of markers centered in three different slices: two markers in the center slice, two 62.5 voxels above the center slice, and another two 62.5 voxels below the center slice. The cone-beam reconstruction algorithm should provide the same level of accuracy for each pair of markers.

The ellipsoid fitting generates the 3D position and fitted radii for each marker, however all 3D voxels of the marker are exploited to fit the ellipsoid using a least squares optimization approach. As a result the determined ellipsoid radii are under estimated. The 3D position of this ellipsoid would be well estimated.

We will first present the results of IR using the ground-truth (GT) geometry before comparing it with the other three geometries.

Preliminary evaluation using the ground-truth calibration for IR

All GT reconstruction gave identical results for all 29 scans despite the varying C-arm geometry between projection images and scans. This would be expected as the voxel size and number of projections would likely remove all noise affects that could be transferred to the reconstructed image.

When visually observing the slices of the GT IR the diameter of all six markers is observed to be precisely 5 voxels in length, width, and depth. This measurement exactly agrees with the diameter of the simulated markers, 2.5 mm.

Comparison of the 3D positions of the six simulated markers with the estimated 3D center positions of the fitted ellipsoids from the images demonstrates zero deviation between the GT IRs and the actual marker positions. The 3D locations are accurate to within the nearest voxel which indicates there is no distortion or error due to the

Table 4.2: Average from all 29 scans of the reconstructed marker RMS position error between the ground-truth and the estimated calibrations: estimated IC with ground-truth extrinsic parameters, estimated IC with reproduced extrinsic calibration error, gold-standard calibration.

Marker Position	Marker position RMS difference with ground-truth IR [voxels]		
	Estimated IC	Estimated IC+EC	Gold-standard
Top	0.8	0.8	0.0
Center	0.8	0.8	0.0
Bottom	0.8	0.8	0.0
All	0.8	0.8	0.0

projection image noise or the reconstruction algorithm.

The radii of the fitted ellipsoid differ from each other on the order of $1/2$ of a voxel for any of the six markers (ie. the ellipsoid is not exactly a sphere). The exact position of the marker within the voxels is not symmetric and therefore the estimated radii may differ from each other although this difference is within the round off error.

Complete evaluation

Given that the GT IRs produce accurate marker positions and radii the reliability of our IRs can be evaluated based on their similarity with these reconstructions. The center slice from the IR generated by each of the four calibrations can be visually compared in Fig. 4.5 for one of the four scans. Table 4.2 presents the average root-mean square (RMS) difference of the positions of the reconstructed markers between the IR using the GT calibration and the other three calibrations. Additionally, Table 4.3 shows the average ratio of the min to max radii for each of the four reconstructions. These values are shown for the average of the top markers, center markers, and bottom markers along with all markers for all 29 reconstructions.

The above tables and figure clearly show that the gold-standard full calibration produces exceptional results which are almost identical to the GT reconstruction with the given voxel size. The images appear visually indistinguishable for all six markers (Fig. 4.5(b)), the RMS position difference was less than the error (Table 4.2), and the radii min to max ratio was identical within the error (Table 4.3).

On the other hand, the reconstructions using the estimated IC calibrations from the collimator edges exhibits significant loss of quality. It is also apparent that the

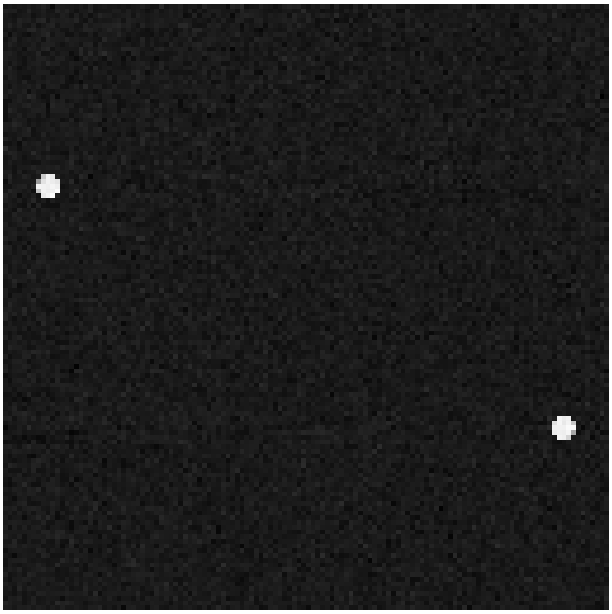

(a) Slice from the ground-truth IR

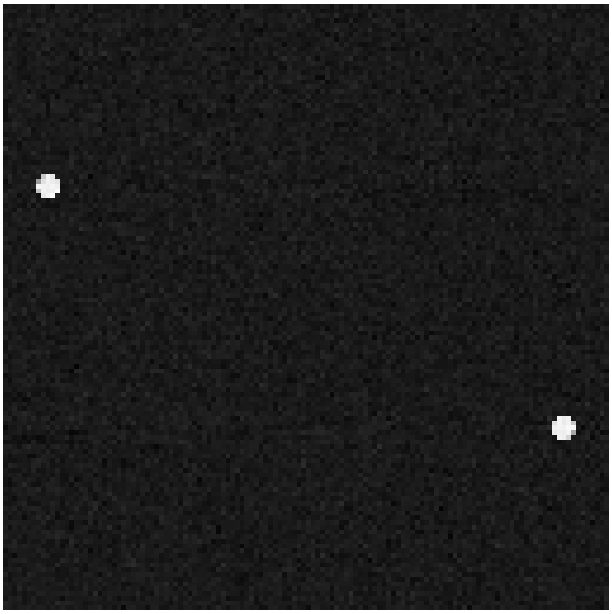

(b) Slice from the IR using the full gold-standard calibration

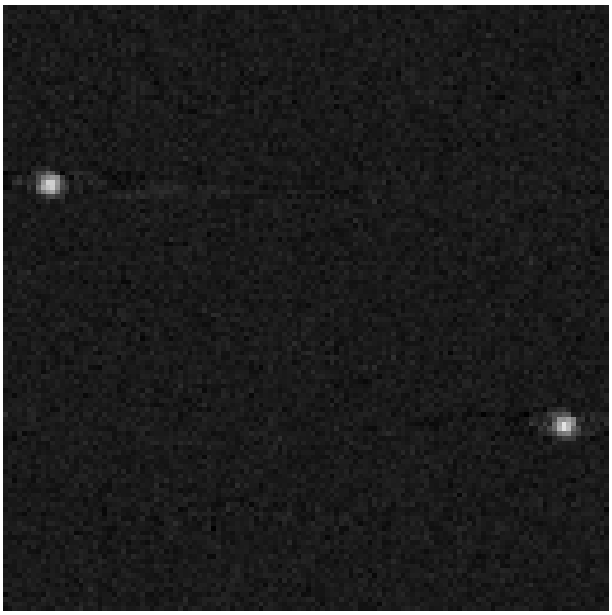

(c) Slice from the IR using the collimator edge determined IC

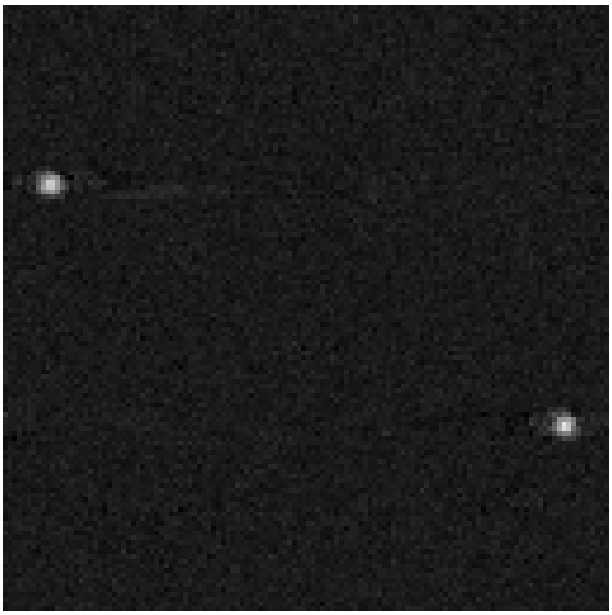

(d) Slice from the IR using the edge determined IC with typical extrinsic calibration errors

Figure 4.5: Image reconstruction comparison of the four different calibrations of a typical scan. The images were reconstructed with $256 \times 256 \times 256$ voxels of size 0.125 mm^3. The images show slice 128 of the reconstruction which has been cropped to size 128×128 to more clearly show the markers. The image gray level was set to the same window and level for comparison.

Table 4.3: Average from all 29 scans of the reconstructed marker radii ratio from the four calibrations: ground-truth, estimated IC with ground-truth extrinsic parameters, estimated IC with reproduced extrinsic calibration error, gold-standard calibration.

Marker Position	Ellipsoid radii ratio, $^{min(r)}/_{max(r)}$			
	Ground-truth	Estimated IC	Estimated IC+EC	Gold-standard
Top	0.8	0.6	0.6	0.8
Center	0.9	0.6	0.6	0.9
Bottom	0.8	0.6	0.6	0.8
All	0.8	0.6	0.6	0.8

reconstructions with estimated IC and either GT extrinsic parameters or reproduced extrinsic calibration error seem indistinguishable: all six markers are visually comparable, same average RMS position error, and same average radii ratio. This indicates that the reproduced extrinsic calibration error from a typical four marker extrinsic calibration technique seems to have no influence on the results. However, when comparing the RMS difference between the marker positions from these two methods demonstrated they were in fact slightly different with an average RMS difference from all markers in all 29 scans of 0.2 voxels. This technique is known to provide very reliable performance (provided conditions are suitable) so this result should not be a surprise. These two calibration procedures gave very similar results for all 29 scans.

A key observation from this analysis is that the degraded image quality of the estimated IC reconstruction is not the same for each reconstructed scan. In fact it changes quite dramatically between scans. (The reason for this may be apparent to an attentive reader.) Due to the error in estimating the collimator edge positions and angles in the initial reference image in which the single view IC parameters are known (or have been measured by another means) results in a static error of the estimated intrinsic calibration parameters of every projection image of the scan. This has been demonstrated and discussed by Daly et al. [Daly *et al.* 2008]. Chapter 3 has shown the inaccuracies of the edge detection process (in the presence of noise and C-arm deformation), the estimated IC varies by: $\sigma_u = 4.0$, $\sigma_v = 4.5$, $\sigma_f = 2.0$. Therefore the edge determination of the initial reference image would contain this same random estimation error. In the event the initial reference estimation contains a large bias, the IR is severely degraded, while if the initial reference image is well estimated a good quality IR ensues.

Fig. 4.5(c) displays an IR with (roughly) the average IR quality of the 29 scans. Fig. 4.6(a) exhibits the best attainable IR quality from the 29 scans while Fig. 4.6(b)

(a) Slice 128 from the reconstruction with minimum estimated IC error

(b) Slice 128 from the reconstruction with maximum estimated IC error

Figure 4.6: Two image reconstructions using the calibration from the estimated IC and GT extrinsic calibration to show the max and min errors due to the estimated calibration. The images were reconstructed with $256 \times 256 \times 256$ voxels of size 0.125 mm^3. The image gray level was set to the same window and level for comparison.

shows an IR with the worst image quality. The set of 29 scans produced about 4 reconstructions with the quality exhibited in Fig. 4.6(b), while most IRs were obtained with similar quality shown in Fig. 4.5(c). A comparison of the ellipsoid radii ratio in these three examples further demonstrates the estimated IC best, typical, and worst IR quality. The six marker average of the ratio of the minimum fitted radii to the maximum fitted radii for these three examples has been found to be:

- ground-truth IR radii ratio = 0.9
- the estimated IC best IR - radii ratio = 0.8 (Fig. 4.6(a))
- the estimated IC typical - radii ratio = 0.7 (Fig. 4.5(c))
- the estimated IC worst IR - radii ratio = 0.2 (Fig. 4.6(b))
- the estimated IC average for all IRs - radii ratio = 0.6

The level of static bias (Δu, Δv, Δf) in the estimated IC parameters causes quite

distinct results. When there is a static bias in the estimation of the u_s parameter the result is a simple translation of the reconstructed image without any image quality degradation. The scanning acquisition follows a circular trajectory in which the rotation axis is parallel to the u-axis. Thus, a static bias in the estimation is equivalent to translation of the 3D volume by $\Delta u/M$, where M is the magnification factor. Of the 29 scans a static bias on the order of $\Delta u = 8.2$ pixels occurred roughly five times. In scan 10 this results in a detector shift of $\Delta d = 1.5$ mm $= 3$ voxels and a 3D image translation of $\Delta y = 1.7$ voxels. Comparison of the RMS position difference between the GT and estimated IC reconstruction also showed a 1.7 voxel difference.

When there is a static bias in the estimation of v_s, the situation is rather different. In this case, an error of Δv is analogous to a detector translation in the plane of the source and detector trajectory (perpendicular to the axis of rotation. This causes an angular dependent error in the back-projection of the imaged marker (illustrated in Fig. 4.7). An error of this type produces severe degradation of the image quality depicted in Fig. 4.6(b). In this figure the magnitude of the static error is so large the back-projection of the marker actually creates a torus, or donut, shape in the 3D reconstruction horizontally and in the plane of the image. Consequently the single marker looks like two separate markers in the slice view of the image.

Static error in the focal length has a similar but significantly reduced affect as the Δv error. The Δf error creates an angular dependent back-projection error but reduced by a factor of $\tan\gamma$, where γ is the angle in the trajectory plane between the central cone-beam ray and the ray passing through the center of the marker: $\Delta d = \Delta f \tan\gamma \approx \Delta v$. The resulting error is dependent on the marker position in 3D space but in this analysis relates to roughly a $1/4^{th}$ reduction compared to the Δv error.

The random error in the estimated IC (σ_u, σ_v, σ_f) produces some image quality degradation, however the quality depicted in Fig. 4.6(a) should be attainable if the edge parameters can be accurately measured in the reference image, and of course the reference single view IC can be accurately measured.

4.4 Discussion

The application to 3D image reconstruction (IR) of our intrinsic calibration method using the collimator edges has produced results with varying degrees of suitability in terms of reconstructed image quality. The results varied significantly due to the edge determination estimation in the initial or reference image for which the single view IC is known or has been measured. In the event of erroneous estimation of the collimator edge

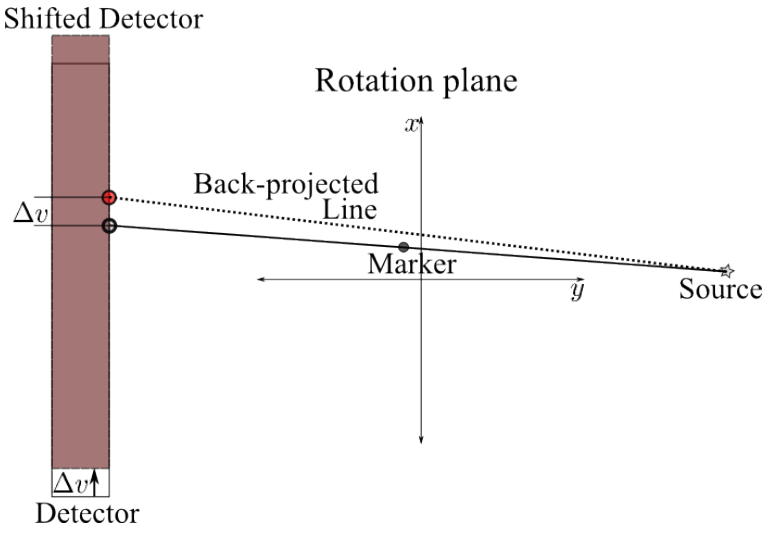

(a) Single back-projection of marker into 3D volume

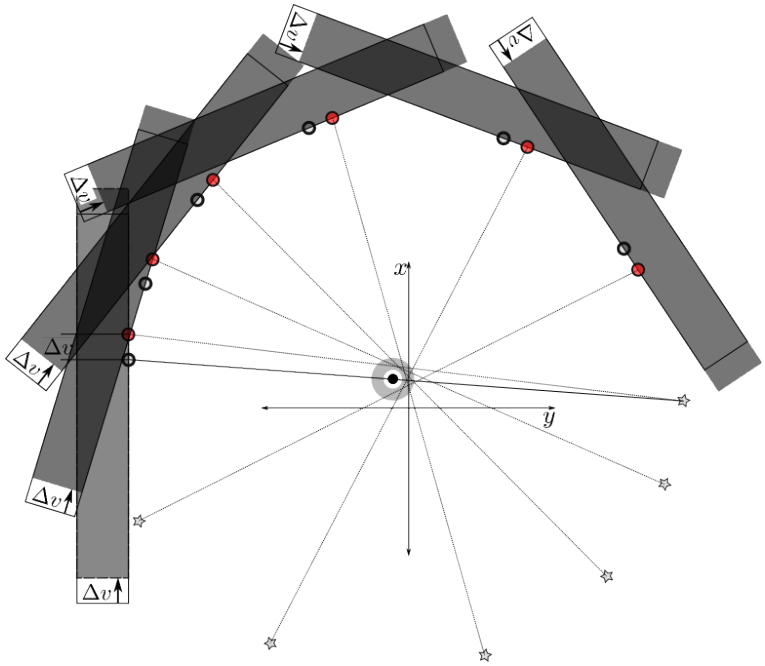

(b) Multiple back-projections of marker as source rotates creates a torus shape in the 3D volume

Figure 4.7: Diagram illustrating the consequence of a static detector position error in the plane of orbital rotation on 3D image reconstruction. The erroneous back-projection during a 360^o scan creates a torus shape in the 3D volume circling the true location of the marker.

positions or angles in this reference image a static error in the estimated IC parameters results which can cause severe degradation of the reconstructed image quality. The principle observation from this study is the clear evidence that the edge detection process for the initial reference image must be achieved with the absolute highest possible degree of accuracy. Even a slight IC bias could eliminate the advantage of using an online calibration method for reconstruction purposes.

Also these evaluations have shown that when the extrinsic calibration is provided by either the ground-truth conditions or a perturbated extrinsic calibration which imitates the level of error which would occur in a four planar marker calibration method the reconstructed images obtained are nearly identical. This reveals that the typical four marker extrinsic calibration approach is reliable and should not contribute much to the image reconstruction errors. If the accuracy of the estimated IC were increased it is clear that eventually the errors from the extrinsic calibration would be observable.

The variations of the estimated IC between projection images has significantly less effect than a static bias. However, when the edge detection process was achieved with good precision and only a small bias in the IC parameters occurred, the quality of the reconstructed image was still not an improvement compared to the IRs produced with the full gold-standard calibration.

Although, the gold-standard calibration has two advantages compared to the edge detection IC that may improve its relative IR quality. First, by using the six imaged markers to produce the gold-standard calibration and then using this calibration to reconstruct the same six markers in the 3D volume provides an unfair advantage to the gold-standard calibration method. The extent of this advantage is unknown and should be tested by reconstructing six markers at a different position in the 3D volume and projection images - hence scan the six marker phantom once for calibration, rotate and translate the phantom and scan again for reconstruction. And secondly, the gold-standard calibration is an offline calibration approach which in real implementation can suffer from non-reproducibility affects between scans, however in these evaluation the gold-standard calibration is used as an online method

As discussed in Chapter 2, the gold-standard calibration method displays a significant variation in the estimated IC parameters with no static bias. Based on the accuracy of the gold-standard IRs compared to the GT IRs, it can be inferred that the full gold-standard calibration method produces a very accurate estimation of the back-projection from the detector to the source, through the 3D volume. This, however, does not indicate that it can provide a practical estimation of the calibration parameters for any single projection.

Further, the effectiveness of the gold-standard calibration method indicates that a full calibration approach in which extrinsic and intrinsic parameters are estimated together or simply the full 12 parameter(up to scale) projection matrix is likely much more appropriate. This suggests that image reconstruction using intrinsic and extrinsic calibration parameters which have been determined by separate processes is less accurate (or more error prone). Instead a method should be adapted which couples the two calibration procedures, such that the imaged collimator edges and the extrinsic calibration phantom (possibly four planar markers at the C-arm isocenter) are utilized together to determine all nine calibration parameters which specify the C-arm geometry and characterize the lines from the detector to the source, through the 3D volume.

Chapter 5

Conclusions and Future work

Résumé du Chapitre 5 en Français

Nous concluons ce travail par une discussion sur la sensibilité de notre méthode de détermination des paramètres intrinsèques d'un C-arm des problèmes associés. Nous proposons des idées pour améliorer ce travail. Nous proposons, dans un travail à venir, de coupler notre calibration intrinsèque utilisant les projections du collimateur dans les radiographies avec les projections d'une mire de calibrage dans le FOV contenant un nombre minimal de marqueurs.

Summary

The purpose of this research is to provide an improvement to classical methods of C-arm geometry calibration, a process required for 3D image reconstruction. The collection of projection images for reconstruction involves the rotation of the C-arm x-ray source and detector around its gantry. During this process there may be a significant amount of C-arm deformation. With the classical calibration approach this deformation is assumed to be reproducible (ie. the deformation is identical between multiple scans), however this is not always the case as vibrational or other non-reproducible motion may occur. If the geometry changes between scans then the scan of the object to be reconstructed must be imaged and simultaneously calibrated, termed online calibration.

Images of the collimator in the field of view (FOV) provides essentially free information of the C-arm intrinsic calibration during the scan. If the extrinsic calibration can be measured during the scan by another means then the two methods together generate the full online calibration of the C-arm. Full online calibration has the potential to deliver higher quality reconstructed images while removing the possibly problematic process of offline calibration.

This research attempts to derive, establish, and evaluate a method of C-arm intrinsic calibration using only the collimator edges in a projection image.

Intrinsic calibration technique using markers

As an initial step, the intrinsic calibration (IC) technique was introduced and tested with simulation conditions using markers. Possible sensitivities which may arise were discussed.

Only four imaged markers (of any size or 3D location) attached to the x-ray source are required to determine the variation of the IC parameters between projection images. For full IC a single view reference IC must be provided by another means. The accuracy of the IC technique was evaluated when initialized using the ground-truth simulation conditions and a single view gold-standard calibration.

The imaged markers provided a precise measurement of the variation of the IC parameters between views: $\sigma_f = 0.1$ pixels, $\sigma_{u_s} = 1.1$ pixels, $\sigma_{v_s} = 1.0$ pixels. However these evaluations demonstrated the necessity for a very accurate initial single view IC: if the initial single view IC contains any errors, these errors are transferred to the IC parameters of every view of the scan causing a static bias.

As a result, an initial IC cannot be provided by a single view of the gold-standard phantom, although an accurate initial IC could be provided using a static C-arm while rotating the gold-standard phantom 360^o manually or on a turntable.

Collimator Edge Detection

Chapter 3 represents the bulk of this research. It deals with the difficult and problematic process of measuring the angles and positions of the thick straight collimator edges in an x-ray image. The investigation is extensive and thorough because the edge parameters must be established with the utmost precision in order to be used for calibration purposes.

Several possible methods of estimating the edges in an image were analyzed through simulation studies and compared with some commonly used edge detection techniques. Ultimately a technique was developed and optimized for thick straight lines in x-ray images with various degrees of image noise:

1. Application of the radon transform at angle θ to obtain a 1D profile of the edge

2. Smoothing of this profile with a low pass Gaussian filter adapted for the appropriate level of image noise
3. Fitting a line to the 1D profile with the same length as the edge profile width, w, in the image
4. Measuring the slope of this line at angle θ: $m(\theta)$
5. Applying steps 1-4 at n angular increments in the desired angular range: θ_i with $i = 1...n$
6. Finding the maximum slope from all lines: $\max = m(\widetilde{\phi})$
7. Locating the mid-point of the maximum slope line: $\widetilde{s}$
8. Produces the estimated edge parameters: $(\widetilde{\phi}, \widetilde{s})$
9. Repeat steps 1-8 for each edge in all projection images

Our developed technique provided an improvement over the commonly used methods evaluated in this study which utilize the Canny edge detector (CED) along with the Radon transform to determine the edge parameters. Further, the CED methods were found to suffer from a loss of sensitivity and inability for accurate determination of edges which are close to $0^o/90^o$ (edges parallel to the image rows or columns). Whereas our method showed only a slight loss of sensitivity very close to $0^o/90^o$.

When edge detection was implemented using real projection images of the x-ray collimator in the FOV the evaluations confirmed that the performance of our method was more stable and gave better agreement between scans. Most importantly this study revealed the sensitivities of edge detection when there is an object in the FOV. Clearly if edge like structure overlap with the imaged edge there would be severe mis-estimations but additionally an angular estimation bias occurs if an object overlaps any part of the edge, unless the object is completely homogenous and overlaps the edge symmetrically around the center.

In summary we have developed a method of thick straight edge detection in x-ray images which provides an improved estimation accuracy compared to standard techniques used in the literature. Our edge detection method can detect edges of various thicknesses, with adequate sensitivity at all angles, and able to adapt to the level of image noise. The edge detection accuracy, measured in simulation studies: $\sigma\bar{\varphi_{RMS}} = 0.0045^o$ and $\sigma\bar{s_{RMS}} = 1.67$ pixels. This can be compared to the best technique commonly used in the literature: $\sigma\bar{\varphi_{RMS}} = 0.0068^o$ and $\sigma\bar{s_{RMS}} = 0.77$. Note that for intrinsic calibration purposes the edge angle estimation is most important as the edge position error is relative to some theoretically defined location within the thick edge. The difference

between the position estimation and the theoretically defined location may be consistent for all estimations and therefore meaning-less.

Although, when detecting edge positions and especially angles at this incredibly high precision, any method of detection would acquire a significant loss of accuracy due to any objects in the field of view which overlap with the imaged edges.

Edge detection for intrinsic calibration and image reconstruction

Next our method of edge detection was utilized for IC, a required step before image reconstruction.

It has been proposed that an accurate measurement of the single view IC can be obtained by rotating (manually or on a turntable) the gold-standard phantom and obtaining multiple projection images to achieve a reliable estimate (by averaging) of the static intrinsic parameters of the reference image. This justifies the use of the ground-truth IC for our initial reference IC. Recall that any error in the reference view IC would cause a static error in the IC of all views of the scan.

In simulation conditions, the variation of the IC parameters measured using our method of edge detection was less accurate than using spherical markers attached the source. Our evaluations exhibited an error of: $\sigma_f = 2.0$ pixels, $\sigma_{u_s} = 4.0$ pixels, $\sigma_{v_s} = 4.5$. This increase in error is due to a reduced sensitivity when estimating the edge angle and position in the image rather than a gray level center of mass weighting. Furthermore, and surprisingly more important, due to the erroneous estimation of the edge angle and positions in the initial reference image a varying level of static bias or error can occur in the IC parameters of every view of the scan.

The application of IC from edge detection to image reconstruction (IR), first and foremost demonstrated that image quality is severely degraded by a static error in the v_s (where the v-axis is perpendicular to the axis of orbital rotation). An error in the focal length degraded the image quality also but to a lesser extent, while a u_s error simply translated the image. It is assumed that if our edge detection IC contains even a slight bias it would no longer be suitable for image reconstruction and therefore it is imperative to remove this source of error for future studies.

Errors induced by the IC parameter variation (opposed to a static error) also degraded the reconstruction image quality. In the event the IC parameters contained no static bias from either the estimation of the edge angle and position in the reference view or the initial reference IC, the variation of the IC parameters exhibited a reconstruction

image quality which was not as good as the gold-standard calibration method, although it is known that our gold-standard reconstructed images contained an unfair advantage which would improve their image quality to some extent. In future studies these advantages must be eliminated to provide an appropriate reconstruction comparison with our calibration methods.

5.1 Discussion and Future work

At this stage the reconstruction evaluations indicate that the IC using the collimator edges in the FOV is not suitable for calibration purposes unless the following things are corrected or improved:

1. Initial reference IC measurement - cannot contain errors
2. Reference image edge determination measurement - higher precision required
3. Edge determinations of all projection images of a scan - must be improved
4. Method of extrinsic calibration required
5. Problematic edge determination with object in FOV

#1 As discussed, any error in the reference IC creates a static bias which has severe effects on the reconstructed image. We have proposed the use of multiple projections of the gold-standard phantom rotating 360^o on a turntable to measure the IC parameters of a stationary C-arm. This must be tested with real C-arm data scans. Additionally, there are a variety of other ways this initial single view IC may be measured, potentially with more accuracy. One possible method utilizes two views of a simple four marker planar phantom positioned at the isocenter as described in [Sturm & Maybank 1999].

#2 The evaluations of edge detection showed that image noise led to an inaccurate edge angle estimation which results in an inaccurate IC. Further it showed that several projections of a static deformed image of the collimator edges with varying noise (essentially multiple projection images of the collimator edges from a stationary C-arm) improves the level of edge detection accuracy. Therefore, very similar to #1, the initial reference edge detection can be improved by acquiring many projection images of the static non-changing collimator edges, estimating the edges in each image, and then averaging the estimated angles and positions of each edge to obtain a more accurate edge determination in the reference image. This protocol would be performed during

the same process of acquiring images of the rotating gold-standard phantom which gives the initial reference IC.

Preliminary investigations with simulation studies confirmed this hypothesis. In future work this technique must be attempted and evaluated with real C-arm images of the collimator.

#**3** Being as the level of IC parameter variation between views causes a degradation in the image reconstruction, the precision of estimation of the edge parameters must be improved at least until the image reconstruction (IR) quality is similar to the gold-standard IR quality. There are several ways to provide some improvement on the overall edge detection process.

First of all instead of requiring an approximate estimation of the edge width in the image a method can be applied using the 2nd derivative of the 1D Radon transform (RT) (similar to the edge detection method discussed in subsection 3.3.2.4 on page 88) to determine an edge width estimation accurate to within $0.5 \times \sqrt{2}$ pixels. Secondly, due to the image background, specifically at the intersection point between two perpendicular edges, a very small edge angle determination bias occurs in both simulation and real data conditions. The affect is small ($\sim 0.002^o$) however this could be compensated for to improve the accuracy of the edge angles. Further, the angular step size at which the Radon transform is performed should be better investigated as it may be possible to improve the edge angle estimation by sampling the Radon transform at a more appropriate angular step size.

An important prospect which could improve the IC would be to use a non-square collimator which has several edges in the image FOV. A hexagonal collimator, for example, would give six edges in which to determine an optimized and improved homography IC. Using a hexagonal collimator, however, has some disadvantages which may make the technique ineffective. Using the Radon transform for edge detection requires that the edges or lines are close to or exceeding the image boundaries. Hexagonal collimator edges would be shorter than square collimator edges and therefore having a decreased signal to noise ratio (in the 1D RT) and therefore a decreased edge angle and position sensitivity. The relative ratio of advantage to disadvantage is unknown and should be investigated.

Lastly, the comparison between the edge determination and spherical marker determination in an x-ray image indicates that edge detection cannot provide the same sensitivity as the gray level center of mass sub-pixel localization of spherical markers. With this aspect in mind, it may be possible to modify the collimator design, or provide

our own adapted collimator attached to the x-ray source with some desired characteristics to improve the IC estimation. To start, the sensitivity of the edge determination process to the width of the edge should be investigated. From the real data edge detection analysis it was proposed that the edge angle estimation is improved if the edge width is wider, while the edge position improves with a decreased edge width. If this is the case a new collimator could be designed (based on the cone-beam x-ray source angle) to give the optimal edge width in the image and produce the best estimation of the IC parameters for reconstruction purposes.

Another approach to producing a more accurate estimation of the IC would be to simply make very small holes in the collimator (with the same direction as the ray from cone-beam source which would pass through these holes). These holes (with appropriate direction) would produce a spherical marker like image on the detector which can be localized with a gray level weighting with sub-pixel accuracy. A downside to this approach is that it requires a larger detector in order to image the small holes away from the collimator edges, or alternatively, reduces the FOV since the collimator must be closed enough to image these holes. Furthermore, one of the most attractive advantages of using the IC of the C-arm is that it requires no adaptation to the C-arm or addition of any other calibration object. Moreover, no information about the collimator must be known, the calibration is based only on the imaged locations of the edges and a single reference image and IC. Any C-arm can take advantage of this technique as all C-arms posses a built-in collimator. By requiring a modified collimator for implementation removes this advantage.

#4 An issue which has not been dealt with in this research is the necessary extrinsic calibration of the C-arm. We have suggested the use of a simple four marker planar calibration technique. This technique is stable and reliable given that the four planar markers are imaged between 30^o and 150^o, where 0^o is the orientation in which the source lies on the plane containing the four markers. Outside of this angular range the four marker extrinsic calibration becomes ill posed [Sturm & Maybank 1999]. When considering a four marker planar phantom at the isocenter of a rotating C-arm system ($> 180^o$), it is clear that a single planar phantom cannot provide the extrinsic calibration for all orbital angles. This issue can be resolved by using at least two orthogonal planar phantoms. The six marker gold-standard phantom contains three planes composed of four markers which can be utilized in simulation conditions and with real C-arm data to allow the extrinsic calibration with a standard computer vision technique (see [Hartley & Zisserman 2004, Burnier 2015, Sturm 2013]).

Using the gold-standard phantom for online extrinsic calibration is not possible as

the calibration phantom cannot be simultaneously scanned with the patient/object. As an approximation it could be assumed that the extrinsic calibration is reproducible. Thus an offline extrinsic calibration can be achieved together with the online IC.

Alternatively, these calibration planes can be provided by four markers embedded in the patient table with another two (or four) protruding orthogonally out of the patient table which become visible in the FOV as the C-arm rotates. These two orthogonal planes of markers give the necessary conditions for online extrinsic calibration. Unfortunately, with this approach the markers must be removed from the projection images before reconstruction which can be a difficult process and interfere with the image of the object in some regions.

As well, there are certainly other possible methods to achieve the extrinsic calibration without the use of markers. For example, the extrinsic calibration could be given by exploiting redundant information which is acquired during parallel, fan, or cone-beam data acquisition [Desbat & Spencer 2014, Clackdoyle & Desbat 2013] also called range conditions or data consistency conditions (DCC).

Coupling - #1, #2, #3 and #4 It can be inferred that a calibration process which determines both the intrinsic and extrinsic calibration simultaneously and with optimization would be a substantial enhancement to the currently suggested methods and additionally could completely eliminate the requirement for an initial reference IC and edge detection (#**1** and #**2**). Imaging a four marker planar phantom with known 3D marker locations to attain the extrinsic calibration, produces eight measurements for the six parameter calibration. Similarly, the imaged collimator edges, in two views, produce eight measurements. Therefore, two views of the collimator and a four marker planar phantom with known marker locations, yields 24 measurements for the (9×2) 18 unknown parameters which completely specify the C-arm geometry in both views. In conclusion, the coupling of the intrinsic and extrinsic calibrations should give more than enough information to solve (and possibly optimize) the C-arm geometric parameters of every view with no need for an error prone initial reference IC and edge image.

#**5** The edge detection process in real data conditions has revealed that the accuracy of the results is incredibly sensitive to an object in the FOV. If the object overlaps with the edges in any way it is sure to produce an incorrect angular (and possibly positional) estimation. As the operator has little control over the object in the FOV this is a difficult, if not impossible problem to solve in some cases.

As previously discussed even a homogeneous object could cause an edge angle and

position error because it reduces the width of the edge profile. This problem could be corrected by the automatic detection of the edge width in the image, an improvement mentioned earlier. When an object which is not homogeneous overlaps the entire edge, the edge profile would suffer from noise like affects. This can be compensated for by increasing the level of smoothing from the low pass Gaussian filter. This image noise level adaptation could be achieved automatically based on a measure of the homogeneity (or variability) in the image FOV close to the edges.

When an object only partially overlaps with the imaged edges a significant angle mis-estimation occurs. In theory this could also be detected by the variation in the edge width and the angular bias compensated for though the process would be cumbersome and error prone.

Ultimately due to the required precision of the edge determination process if there is any object to edge overlap the accuracy will be reduced. As proposed in #**3**, an adapted collimator with small holes could completely remove the complications when dealing with an object in the FOV.

Summary of future work

- Correct, if possible, any minor biases or errors in the edge detection method
  - implement automated edge width and noise determination
  - adapt Radon transform edge detection to allow for sub-pixel position estimation
- Develop, evaluate, and implement method of coupling between a four marker extrinsic calibration method and the collimator intrinsic calibration
  - test with both simulation and real data experiments
- Using real data experiments, evaluate the method of more accurate reference IC (using rotating gold-standard phantom) and simultaneous reference edge determination using multiple images from a static C-arm
  - extrinsic calibration determined from four planar marker phantom, or
  - method of extrinsic calibration (potentially using data consistency conditions)
- With the full calibrations from the above two methods, perform 3D image reconstruction and compare these two methods with the gold-standard generated reconstruction.
- Perform further investigations into edge detection sensitivity
  - with object in the FOV
  - at various x-ray tube voltages and currents

Bibliography

[Abràmoff *et al.* 2004] Michael D. Abràmoff, Paulo J. Magalhães and J. Ram. Sunanda. *Image processing with ImageJ.* Biophotonics International, vol. 11, no. 7, pages 36–43, 2004. (Citations pages 22 and 34.)

[Amiri *et al.* 2013] Shahram Amiri, David R Wilson, Bassam a Masri and Carolyn Anglin. *A low-cost tracked C-arm (TC-arm) upgrade system for versatile quantitative intraoperative imaging.* International journal of computer assisted radiology and surgery, pages 1–17, dec 2013. (Citations pages 5 and 6.)

[Beylkin 1987] G. Beylkin. *Discrete radon transform.* IEEE Transactions on Acoustics, Speech, and Signal Processing, vol. 35, no. 2, pages 162–172, 1987. (Citation page 49.)

[Bronnikov 1999] AV Bronnikov. *Virtual alignment of x-ray cone-beam tomography system using two calibration aperture measurements.* Optical Engineering, pages 381–386, 1999. (Citation page 7.)

[Burnier 2015] C Burnier. *Reconstruction 3D à partir de plusieurs prises de vue.* Rapport technique, Ecole Supérieure de Chimie Physique Electronique de Lyon, Lyon, 2015. (Citations pages 8, 129 and 145.)

[Burns & Hanson 1986] J Brian Burns and Allen R Hanson. *Extracting Straight Lines.* IEEE Transactions on Pattern Analysis and Machine Intelligence, vol. 8, no. 4, pages 425–455, 1986. (Citations pages 44, 45 and 47.)

[Canny 1986] John Canny. *A computational approach to edge detection.* IEEE transactions on pattern analysis and machine intelligence, vol. 8, no. 6, pages 679–698, 1986. (Citation page 44.)

[Chan *et al.* 2008] Yvonne Chan, Jeffrey H. Siewerdsen, Mark a. Rafferty, Douglas J. Moseley, David a. Jaffray and Jonathan C. Irish. *Cone-beam computed tomography on a mobile C-arm: Novel intraoperative imaging technology for guidance of head and neck surgery.* Journal of Otolaryngology - Head and Neck Surgery, vol. 37, no. 1, pages 81–90, 2008. (Citation page 3.)

[Cho *et al.* 2005] Youngbin Cho, Douglas J. Moseley, Jeffrey H. Siewerdsen and David a. Jaffray. *Accurate technique for complete geometric calibration of cone-beam computed tomography systems.* Medical Physics, vol. 32, no. 4, pages 968–983, 2005. (Citation page 4.)

[Clackdoyle & Desbat 2013] Rolf Clackdoyle and Laurent Desbat. *Full data consistency conditions for cone-beam projections with sources on a plane.* Physics in medicine and biology, vol. 58, no. 23, pages 8437–56, dec 2013. (Citation page 146.)

[Clackdoyle & Mennessier 2011] R Clackdoyle and C Mennessier. *Centers and centroids of the cone-beam projection of a ball.* Physics in medicine and biology, vol. 56, no. 23, pages 7371–91, dec 2011. (Citation page 33.)

[Copeland *et al.* 1995] Anthony C. Copeland, Gopalan Ravichandran and Mohan M. Trivedi. *Localized radon transform-based detection of ship wakes in SAR images.* IEEE Transactions on Geoscience and Remote Sensing, vol. 33, no. 1, pages 35–45, 1995. (Citations pages 43, 44, 45 and 49.)

[Coppini & Demi 1993] G Coppini and M Demi. *An artificial vision system for X-ray images of human coronary trees.* Pattern Analysis and ..., vol. 15, no. 2, pages 156–162, 1993. (Citation page 9.)

[Daly *et al.* 2008] M. J. Daly, J. H. Siewerdsen, Y. B. Cho, D. a. Jaffray and J. C. Irish. *Geometric calibration of a mobile C-arm for intraoperative cone-beam CT.* Medical Physics, vol. 35, no. 5, pages 2124–2136, 2008. (Citations pages 4, 5, 24, 40, 127 and 133.)

[Deans 1981] Stanley R. Deans. *Hough Transform from the Radon Transform.* IEEE Transactions on Pattern Analysis and Machine Intelligence, vol. PAMI-3, no. 2, pages 185–188, 1981. (Citation page 45.)

[Deriche 1987] R. Deriche. *Using Canny's criteria to derive a recursivley implemented Optimal edge detector.* International Journal of Computer Vision, vol. 1, no. 2, pages 167–187, 1987. (Citation page 44.)

[Desbat & Spencer 2014] Laurent Desbat and Benjamin Spencer. *Calibration with DCC in tomography.* In SURGETICA, pages 3–5, 2014. (Citation page 146.)

[Duda & Hart 1972] Richard O. Duda and Peter E. Hart. *Use of the Hough transformation to detect lines and curves in pictures.* Communications of the ACM, vol. 15, no. 1, pages 11–15, jan 1972. (Citations pages 44 and 45.)

[Faugeras 1993] Olivier Faugeras. Three-dimensional Computer Vision: A Geometric Viewpoint. MIT Press, 1993. (Citation page 15.)

[Feldkamp *et al.* 1984] LA Feldkamp, LC Davis and JW Kress. *Practical cone-beam algorithm.* JOSA A, vol. 1, no. 6, pages 612–619, 1984. (Citations pages 4, 10, 121 and 126.)

[Gorges *et al.* 2006] Sébastien Gorges, Erwan Kerrien, Marie-Odile Berger, Yves Trous-

set, Jérémie Pescatore, René Anxionnat and Luc Picard. *An effective technique for calibrating the intrinsic parameters of a vascular C-arm from a planar target.* In SPIE Medical Imaging, volume 6141, pages 61411W–61411W–10, mar 2006. (Citations pages 2 and 7.)

[Gorges 2007] Sébastien Gorges. *Vers un système de navigation 3D en neuroradiologie interventionnelle.* PhD thesis, Henri Poincaré, 2007. (Citations pages 2 and 7.)

[Götz & Druckmüller 1995] W. A. Götz and H. J. Druckmüller. *A fast digital Radon transform - An efficient means for evaluating the Hough transform.* Pattern Recognition, vol. 28, no. 12, pages 1985–1992, 1995. (Citations pages 43, 45 and 49.)

[Hartley & Zisserman 2004] R.I. Hartley and A. Zisserman. Multiple View Geometry in Computer Vision. Cambridge University Press, ISBN: 0521540518, second édition, 2004. (Citations pages 15, 30 and 145.)

[Hofstetter *et al.* 1999] R. Hofstetter, M. Slomczykowski, M. Sati and L. P. Nolte. *Fluoroscopy as an imaging means for computer-assisted surgical navigation.* Computer Aided Surgery, vol. 4, no. 2, pages 65–76, 1999. (Citation page 3.)

[Jaffray *et al.* 2002a] David a Jaffray, Jeffrey H Siewerdsen, Gregory K Edmundson, John W Wong, Alvaro a Martinez, William Beaumont Hospital and Royal Oak. *Flat-panel cone-beam CT on a mobile isocentric C-arm for image-guided brachytherapy.* Proc. SPIE, vol. 4682, pages 209–217, 2002. (Citation page 3.)

[Jaffray *et al.* 2002b] David a. Jaffray, Jeffrey H. Siewerdsen, John W. Wong and Alvaro a. Martinez. *Flat-panel cone-beam computed tomography for image-guided radiation therapy.* International Journal of Radiation Oncology Biology Physics, vol. 53, no. 5, pages 1337–1349, aug 2002. (Citations pages 3 and 4.)

[Kak & Slaney 1988] A. C. Kak and Malcolm Slaney. *Chapter 3: Algorithms for reconstruction with nondiffracting sources.* In Principles of Computerized Tomographic Imaging, numéro 1, pages 49–112. IEEE Press, 1988. (Citations pages 121 and 123.)

[Khoury *et al.* 2007] A. Khoury, J H Siewerdsen, C M Whyne, M J Daly, H J Kreder, D J Moseley and D a Jaffray. *Intraoperative cone-beam CT for image-guided tibial plateau fracture reduction.* Computer aided surgery : official journal of the International Society for Computer Aided Surgery, vol. 12, no. 4, pages 195–207, 2007. (Citation page 3.)

[Lavest *et al.* 1998] Jean-Marc Lavest, Marc Viala and M Dhome. *Do We Really Need an*

Accurate Calibration Pattern to Achieve a Reliable Camera Calibration? Computer Vision ECCV'98, pages 158—-, 1998. (Citation page 7.)

[Maier *et al.* 2011] A. Maier, J.-H. Choi, A. Keil, C. Niebler, M. Sarmiento, A. Fieselmann, G. Gold, S. Delp and R. Fahrig. *Analysis of vertical and horizontal circular C-arm trajectories.* In SPIE Medical Imaging, volume 7961, pages 796123–796123–8, 2011. (Citation page 4.)

[Maintz *et al.* 1996] J.B.a. Maintz, P.a. Van Den Elsen and M.a. Viergever. *Evaluation of ridge seeking operators for multimodality medical\nimage matching.* IEEE Transactions on Pattern Analysis and Machine Intelligence, vol. 18, no. 4, pages 353–365, 1996. (Citation page 9.)

[Matlab 2014] Matlab. Radon Transform, Image Processing Toolbox User's Guide, version 8.3.0 (R2014a). The Mathworks Inc., Natick, Massachusetts, 2014. (Citations pages 55, 71, 73 and 89.)

[Mennessier *et al.* 2009] C Mennessier, R Clackdoyle and F Noo. *Direct determination of geometric alignment parameters for cone-beam scanners.* Physics in medicine and biology, vol. 54, no. 6, pages 1633–60, mar 2009. (Citations pages 4, 7, 8, 14, 23, 33, 34 and 129.)

[Mitschke & Navab 2003] M. Mitschke and N. Navab. *Recovering the X-ray projection geometry for three-dimensional tomographic reconstruction with additional sensors: Attached camera versus external navigation system.* Medical Image Analysis, vol. 7, no. 1, pages 65–78, 2003. (Citations pages 2, 5, 6 and 9.)

[Mitschke *et al.* 2000] Matthias Mitschke, Nassir Navab and Oliver Schütz. *Online geometrical calibration of a mobile C-arm using external sensors.* In SPIE Medical Imaging, volume 3976, pages 580–587, 2000. (Citations pages 5 and 6.)

[Murphy 1986] Lesley M. Murphy. *Linear feature detection and enhancement in noisy images via the Radon transform.* Pattern Recognition Letters, vol. 4, no. 4, pages 279–284, 1986. (Citation page 45.)

[Navab & Mitschke 2001] Nassir Navab and Matthias M. Mitschke. *Method and apparatus using a virtual detector for three-dimensional reconstruction from x-ray images.* United States Patent No.:6236704 B1, 2001. (Citations pages 2, 6 and 9.)

[Navab *et al.* 1996] Nassir Navab, Ali R. Bani-Hashemi, Matthias M. Mitschke, David W. Holdsworth, Rebecca Fahrig, Allan J. Fox and R. Graumann. *Dynamic Geometrical Calibration for 3-D Cerebral Angiography.* In Richard L. Van Metter and Jacob Beutel, editeurs, SPIE Medical Imaging, volume 2708, pages

361–370, apr 1996. (Citation page 5.)

[Navab *et al.* 1999] N. Navab, A. Bani-Kashemi and M. Mitschke. *Merging visible and invisible: two Camera-Augmented Mobile C-arm (CAMC) applications.* In Proc. 2nd IEEE and ACM International Workshop on Augmented Reality (IWAR'99), pages 134–141, 1999. (Citations pages 6 and 9.)

[Noel *et al.* 2006] Peter B. Noel, Kenneth R. Hoffmann, Snehal Kasodekar, Alan M. Walczak, Sebastian Schafer, Peter B Noël, Kenneth R. Hoffmann, Snehal Kasodekar, Alan M. Walczak and Sebastian Schafer. *Optimization of three-dimensional angiographic data obtained by self-calibration of multiview imaging.* Medical Physics, vol. 33, no. 10, page 3901, sep 2006. (Citation page 3.)

[Noo *et al.* 2000] F Noo, R Clackdoyle, C Mennessier, T a White and T J Roney. *Analytic method based on identification of ellipse parameters for scanner calibration in cone-beam tomography.* Physics in medicine and biology, vol. 45, no. 11, pages 3489–3508, 2000. (Citation page 4.)

[Noo 1998] Frédéric Noo. *Méthodes numériques directes de reconstruction d'images tridimensionnelles à partir de projections coniques.* PhD thesis, Universite de Liege, 1998. (Citations pages 10, 120 and 121.)

[Orth *et al.* 2008] Robert C Orth, Michael J Wallace and Michael D Kuo. *C-arm cone-beam CT: general principles and technical considerations for use in interventional radiology.* Journal of vascular and interventional radiology: JVIR, vol. 19, no. 6, pages 814–820, jun 2008. (Citation page 3.)

[Parker 1982] DL Parker. *Optimal short scan convolution reconstruction for fan beam CT.* Medical Physics, vol. 9, no. 2, pages 254–257, 1982. (Citation page 4.)

[Rey *et al.* 1990] Maria T. Rey, James K. Tunaley, J. T. Folinsbee, Paul a. Jahans, John a. Dixon and Malcolm R. Vant. *Application of Radon transform techniques to wake detection in Seasat-A SAR images.* IEEE Transactions on Geoscience and Remote Sensing, vol. 28, no. 4, pages 553–560, 1990. (Citations pages 43 and 45.)

[Rit *et al.* 2014] S Rit, M Vila Oliva, S Brousmiche, R Labarbe, D Sarrut and G C Sharp. *The Reconstruction Toolkit (RTK), an open-source cone-beam CT reconstruction toolkit based on the Insight Toolkit (ITK).* Journal of Physics: Conference Series, vol. 489, page 012079, 2014. (Citations pages 8, 120 and 128.)

[Schuetz & Mitschke 2002] Oliver Schuetz and Matthias Mitschke. *X-ray apparatus for producing a 3D image from a set of 2D projections.* United States Patent

No.:6379041 B1, 2002. (Citation page 9.)

[Schuetz 2001] Oliver Schuetz. *X-ray apparatus for producing a 3D image from a set of 2D projections*. United States Patent No.:6206566 B1, 2001. (Citations pages 2 and 9.)

[Siewerdsen *et al.* 2005] J. H. Siewerdsen, D. J. Moseley, S. Burch, S. K. Bisland, A. Bogaards, B. C. Wilson and D. A. Jaffray. *Volume CT with a flat-panel detector on a mobile, isocentric C-arm: Pre-clinical investigation in guidance of minimally invasive surgery*. Medical Physics, vol. 32, no. 1, page 241, jan 2005. (Citations pages 3 and 5.)

[Spencer & Desbat 2014] Benjamin Spencer and Laurent Desbat. *On-line C-arm Intrinsic Calibation: Simulation Study*. In IEEE Nuclear Science Symposium Conference Record, page (to appear), 2014. (Citation page 30.)

[Spencer *et al.* 2012] B Spencer, R Clackdoyle, C Mennessier and T Xu. *Distortion Correction, Geometric Calibration, and Volume Reconstruction for an Isocentric C-Arm X-Ray System: Preliminary Studies*. In Proc. of the second international conference on image formation in X-ray computed tomography, pages 279–283, 2012. (Citations pages 7, 14, 23, 33 and 129.)

[Strobel *et al.* 2003] Norbert Strobel, Benno Heigl, Thomas Brunner, O Schütz, M Mitschke, Karl Wisent and Thomas Mertelmeier. *Improving 3D image quality of x-ray C-arm imaging systems by using properly designed pose determination systems for calibrating the projection geometry*. In SPIE Medical Imaging, pages 943–954, 2003. (Citations pages 4 and 5.)

[Sturm & Maybank 1999] P.F. Sturm and S.J. Maybank. *On plane-based camera calibration: A general algorithm, singularities, applications*. Proceedings. 1999 IEEE Computer Society Conference on Computer Vision and Pattern Recognition (Cat. No PR00149), vol. 1, pages 432–437, 1999. (Citations pages 8, 30, 143 and 145.)

[Sturm 2000] Peter Sturm. *Algorithms for plane-based pose estimation*. In Computer Vision and Pattern Recognition, volume 89221, pages 706–711, 2000. (Citation page 30.)

[Sturm 2013] Peter Sturm. *Some lecture notes on Geometric Computer Vision*. Rapport technique, University of Grenoble, 2013. (Citations pages 15, 32 and 145.)

[Toft 1996] Peter Toft. *The Radon Transform Theory and Implemtentaion*. PhD thesis, Technical University of Denmark, 1996. (Citation page 49.)

[Turbell 2001] Henrik Turbell. *Cone-beam reconstruction using filtered backprojection*.

PhD thesis, Linköpings universitet, 2001. (Citations pages 121 and 126.)

[Tuy 1983] Heang K. Tuy. *An Inversion Formula for Cone-Beam Reconstruction.* SIAM Journal on Applied Mathematics, vol. 43, no. 3, pages pp. 546–552, 1983. (Citation page 121.)

[Zhang & Couloigner 2007] Qiaoping Zhang and Isabelle Couloigner. *Accurate Centerline Detection and Line Width Estimation of Thick Lines Using the Radon Transform.* IEEE Transactions on Image Processing, vol. 16, no. 2, pages 310–316, feb 2007. (Citations pages 43, 45 and 59.)

On-line C-arm Intrinsic Calibration by means of an Accurate Method of Line Detection using the Radon Transform

Résumé

Les “C-arm” sont des systèmes de radiologie interventionnelle fréquemment utilisés en salle d'opération ou au lit du patient. Des images 3D des structures anatomiques internes peuvent être calculées à partir de multiples radiographies acquises sur un “C-arm mobile” et isocentrique décrivant une trajectoire généralement circulaire autour du patient. Pour cela, la géométrie conique d'acquisition de chaque radiographie doit être précisément connue. Malheureusement, les C-arm se déforment en général au cours de la trajectoire. De plus leur motorisation engendre des oscillations non reproductibles. Ils doivent donc être calibrés au cours de l'acquisition. Ma thèse concerne la calibration intrinsèque d'un C-arm à partir de la détection de la projection du collimateur de la source dans les radiographies.

Nous avons développé une méthode de détection de la projection des bords linéaires du collimateur. Elle surpasse les méthodes classiques comme le filtre de Canny sur données simulées ou réelles. La précision que nous obtenons sur l'angle et la position (φ, s) des droites est de l'ordre de $\varphi_{RMS} = \pm 0.0045$ et $s_{RMS} = \pm 1.67$ pixels. Nous avons évalué nos méthodes et les avons comparés à des méthodes classiques de calibration dans le cadre de la reconstruction 3D.

Mots-clefs radiographie interventionnelle, C-arm calibration, géométrie conique et pin-hole, détection de droites, transformée de Radon, filtre de Canny, CB CT.

On-line C-arm Intrinsic Calibration by means of an Accurate Method of Line Detection using the Radon Transform

Abstract

Mobile isocentric x-ray C-arm systems are an imaging tool used during a variety of interventional and image guided procedures. Three-dimensional images can be produced from multiple projection images of a patient or object as the C-arm rotates around the isocenter provided the C-arm geometry is known. Due to gravity affects and mechanical instabilities the C-arm source and detector geometry undergo significant non-ideal and possibly non reproducible deformation which requires a process of geometric calibration. This research investigates the use of the projection of the slightly closed x-ray tube collimator edges in the image field of view to provide the online intrinsic calibration of C-arm systems.

A method of thick straight edge detection has been developed which outperforms the commonly used Canny filter edge detection technique in both simulation and real data investigations. This edge detection technique has exhibited excellent precision in detection of the edge angles and positions, (φ, s), in the presence of simulated C-arm deformation and image noise: $\varphi_{RMS} = \pm 0.0045^o$ and $s_{RMS} = \pm 1.67$ pixels. Following this, the C-arm intrinsic calibration, by means of accurate edge detection, has been evaluated in the framework of 3D image reconstruction.

Keywords Interventional radiology, C-arm on-line calibration, Conical and pin-hole geometry, x-ray edge detection, Radon transform, Canny filter, CB CT